


2019

## High-dynamic-range Foveated Near-eye Display System

Guanjun Tan  
*University of Central Florida*

 Part of the [Electromagnetics and Photonics Commons](#), and the [Optics Commons](#)  
Find similar works at: <https://stars.library.ucf.edu/etd>  
University of Central Florida Libraries <http://library.ucf.edu>

This Doctoral Dissertation (Open Access) is brought to you for free and open access by STARS. It has been accepted for inclusion in Electronic Theses and Dissertations, 2004-2019 by an authorized administrator of STARS. For more information, please contact [STARS@ucf.edu](mailto:STARS@ucf.edu).

---

### STARS Citation

Tan, Guanjin, "High-dynamic-range Foveated Near-eye Display System" (2019). *Electronic Theses and Dissertations, 2004-2019*. 6832.  
<https://stars.library.ucf.edu/etd/6832>

# HIGH-DYNAMIC-RANGE FOVEATED NEAR-EYE DISPLAY SYSTEM

by

GUANJUN TAN

B.S. University of Science and Technology of China, 2014

A dissertation submitted in partial fulfillment of the requirements  
for the degree of Doctor of Philosophy  
in the College of Optics and Photonics  
at the University of Central Florida  
Orlando, Florida

Summer Term

2019

Major Professor: Shin-Tson Wu

© 2019 Guanjun Tan

## ABSTRACT

Wearable near-eye display has found widespread applications in education, gaming, entertainment, engineering, military training, and healthcare, just to name a few. However, the visual experience provided by current near-eye displays still falls short to what we can perceive in the real world. Three major challenges remain to be overcome: 1) limited dynamic range in display brightness and contrast, 2) inadequate angular resolution, and 3) vergence-accommodation conflict (VAC) issue. This dissertation is devoted to addressing these three critical issues from both display panel development and optical system design viewpoints.

A high-dynamic-range (HDR) display requires both high peak brightness and excellent dark state. In the second and third chapters, two mainstream display technologies, namely liquid crystal display (LCD) and organic light emitting diode (OLED), are investigated to extend their dynamic range. On one hand, LCD can easily boost its peak brightness to over 1000 nits, but it is challenging to lower the dark state to  $<0.01$  nits. To achieve HDR, we propose to use a mini-LED local dimming backlight. Based on our simulations and subjective experiments, we establish practical guidelines to correlate the device contrast ratio, viewing distance, and required local dimming zone number. On the other hand, self-emissive OLED display exhibits a true dark state, but boosting its peak brightness would unavoidably cause compromised lifetime. We propose a systematic approach to enhance OLED's optical efficiency while keeping indistinguishable angular color shift. These findings will shed new light to guide future HDR display designs.

In Chapter four, in order to improve angular resolution, we demonstrate a multi-resolution foveated display system with two display panels and an optical combiner. The first display panel



provides wide field of view for peripheral vision, while the second panel offers ultra-high resolution for the central fovea. By an optical minifying system, both  $4\times$  and  $5\times$  enhanced resolutions are demonstrated. In addition, a Pancharatnam-Berry phase deflector is applied to actively shift the high-resolution region, in order to enable eye-tracking function. The proposed design effectively reduces the pixelation and screen-door effect in near-eye displays.

The VAC issue in stereoscopic displays is believed to be the main cause of visual discomfort and fatigue when wearing VR headsets. In Chapter five, we propose a novel polarization-multiplexing approach to achieve multiplane display. A polarization-sensitive Pancharatnam-Berry phase lens and a spatial polarization modulator are employed to simultaneously create two independent focal planes. This method enables generation of two image planes without the need of temporal multiplexing. Therefore, it can effectively reduce the frame rate by one-half.

In Chapter six, we briefly summarize our major accomplishments.

To my beloved family.

## ACKNOWLEDGEMENTS

Five-years-long Ph.D. journey is a truly life-changing experience for me. It would not have been possible without the support and guidance from those around me. I would like to acknowledge those who took their time to help me during past five years.

First and foremost, I would like to render my warmest thanks to my Ph.D. advisor, Dr. Shin-Tson Wu, especially for his insightful teachings, visionary suggestions and continuous encouragement. Prof. Wu is a visionary leading researcher in the display area. He is always encouraging us to explore new research frontiers, so that we can learn both the big picture of new trends and technical details. He is also always willing to help whenever I need guidance, either in research or in career. He will be my life-long friend and the best role model of a scientist and teacher. I would also like to express my special thanks to Dr. Wu's better half Cho-Yan Hiseh for her care and love over the years. I feel so blessed being one of this big family.

I would like to thank my committee members: Prof. M. G. Moharam, Prof. Boris Y. Zeldovich, Prof. C. Kyle Renshaw and Prof. Yajie Dong. They have been always helpful in providing insightful discussions during my Ph.D. pursuit and invaluable advises for my candidacy, proposal and thesis preparation. Besides, they provided strong recommendation and support when I applied for some society awards and scholarships.

I would like to thank my labmates and collaborators, who offered valuable help for my research adventure. I would like to express my appreciation to former and present group members, particularly Dr. Daming Xu, Dr. Zhenyue Luo, Dr. Ruidong Zhu, Dr. Fenglin Peng, Dr. Haiwei Chen, Dr. Yun-han Lee, Dr. Sang-hun Choi, Juan He, Fangwang Gou, Yuge Huang, Ziqian He,

Tao Zhan, Kun Yin, Jianghao Xiong, Md Javed Rouf Talukder, Yannanqi Li, En-lin Hsiang, Junyu Zhou, Hao Chen and Caicai Zhang. In addition, I wish to give my special thanks to my collaborator Prof. Jiun-Haw Lee from National Taiwan University, for his valuable suggestions and fruitful discussions on moth-eye coating and OLED displays. I wish to thank Mr. Yishi Weng from Southeast University of China for valuable discussions on AR and VR displays. Besides, I'd like to thank my friends Mr. Frank Fanjiang, Dr. Zhibing Ge, Dr. Kay Tai, Dr. Yuan Chen and Dr. Xiaokai Li at Apple PPO-Optics Group for their support and inspirations during my internship.

Lastly, I wish to express my deepest gratitude to my parents, my grandparents and my sister for their unconditional support during my Ph.D. years. They always respect and support my choices and without their help life here would be much more challenging.

## TABLE OF CONTENTS

LIST OF FIGURES .....	x
LIST OF TABLES .....	xv
CHAPTER 1: INTRODUCTION .....	1
1.1 Basis of near-eye display .....	2
1.2 Challenges and motivations .....	4
CHAPTER 2: MINI-LED BACKLIT LCD .....	6
2.1 Background .....	6
2.2 System modelling .....	8
2.3 Subjective experiment .....	15
2.4 Experimental results .....	17
2.5 Discussion .....	19
2.6 Summary .....	22
CHAPTER 3: ORGANIC LIGHT-EMITTING DIODE .....	24
3.1 Background .....	24
3.2 Simulation modelling .....	26
3.3 Experimental verification .....	28
3.4 Systematic optimization .....	33
3.5 Optimization results .....	37
3.6 Discussion .....	41

3.7 Summary .....	43
CHAPTER 4: FOVEATED NEAR-EYE DISPLAY .....	44
4.1 Background .....	44
4.2 System configuration .....	47
4.3 Experimental prototyping .....	49
4.4 Image shifter .....	53
4.5 Summary .....	59
CHAPTER 5: MULTIPLANE DISPLAY .....	61
5.1 Background .....	61
5.2 System configuration .....	63
5.3 Experimental prototyping .....	67
5.4 Image rendering .....	70
5.5 Hybrid multiplexed display.....	73
5.6 Discussion .....	76
5.7 Summary .....	77
CHAPTER 6: CONCLUSION .....	79
APPENDIX: STUDENT PUBLICATIONS .....	82
REFERENCES .....	90

## LIST OF FIGURES

Figure 1-1   Representation of virtuality continuum. Adapted from Milgram and Kishino [3]. ....	1
Figure 1-2   Schematic layout of a typical near-eye display system. ....	3
Figure 2-1   Schematic layouts of (a) conventional global-dimming LCD panel and (b) local-dimming LCD panel. ....	7
Figure 2-2   Schematic diagram of a mini-LED backlit LCD. ....	9
Figure 2-3   Simulated test patterns of mini-LED backlight. Mini-LED backlight local dimming modulation with (a) pattern I, (b) pattern II, (c) pattern III, and (d) pattern IV. Simulated displayed images: (e) pattern I, (f) pattern II, (g) pattern III, and (h) pattern IV. ....	10
Figure 2-4   Displayed image simulation. (a) mini-LED backlight modulation; (b) luminance distribution of the light incident on LC layer, and (c) displayed image after LCD modulation. ...	12
Figure 2-5   Color difference $\Delta E$ for different local dimming zone numbers: a) 18; b) 288; c) 1152 and d) 10368. ....	14
Figure 2-6   Color difference $\Delta E$ for LCD contrast ratios: a) 1500:1; b) 2500:1; c) 3500:1 and d) 4500:1. ....	14
Figure 2-7   HDR target pictures used in the subjective experiment: a) Beach, b) City light, c) Christmas, d) Firework, e) Tower, f) Stars, g) Sunset, h) Waffle house, i) Lamp, and j) Candle. ...	16
Figure 2-8   Subjective experiment results of perceived image difference. ....	18
Figure 2-9   Simulated <i>LabPSNR</i> for different mini-LED backlit LCDs. ....	19
Figure 2-10   Conceptual diagram of scaling up display size based on same angular size. ....	20
Figure 3-1   Mechanism of angular color shift of mixed color in an RGB-OLED display. ....	25

Figure 3-2   EL spectra of weak cavity OLEDs at different viewing angles. Measured results: a) device 1; b) device 2 and c) device 3. Simulated results: d) device 1; e) device 2 and f) device 3. ....	30
Figure 3-3   EL spectra of strong cavity OLEDs at different viewing angles. Measured results: a) device 4; b) device 5, and c) device 6. Simulated results: d) device 4; e) device 5 and f) device 6. ....	31
Figure 3-4   OLED EL emission intensity angular distributions: a) device 1; b) device 2; c) device 3; d) device 4; e) device 5; and f) device 6. ....	32
Figure 3-5   Measured and simulated color shifts of OLED devices: a) device 1; b) device 2; c) device 3; d) device 4; e) device 5; and f) device 6. ....	33
Figure 3-6   Layer structures of OLED display with Red, Green and Blue sub-pixels. ....	34
Figure 3-7   10 reference colors in CIE1976 color space. ....	37
Figure 3-8   The <i>Pareto Front</i> of the 3-objective systematic optimization. ....	38
Figure 3-9   Color shift of the 10 reference colors from 0° to 60° for Op1 RGB-OLED. ....	39
Figure 3-10   Color shift of the first 18 colors in Macbeth ColorChecker from 0° to 60° for Op1 RGB-OLED. ....	40
Figure 3-11   The correlations between the OLED optical behaviors and the layers' thickness: (a)(b)(c) HTL layers (red- $d_1$ , green- $d_2$ , blue- $d_3$ ); (d)(e)(f) CPL layers (red- $d_4$ , green- $d_5$ , blue- $d_6$ ); (g)(h)(i) Al <sub>2</sub> O <sub>3</sub> layers in thin film encapsulation (blue- $d_7$ , green- $d_9$ , red- $d_{11}$ ); (j)(k)(l) polymer layers in thin film encapsulation (blue- $d_8$ , red- $d_{10}$ ). ....	42
Figure 4-1   The trade-off between angular resolution and field of view in near-eye displays. ...	45
Figure 4-2   Illustration of human visual acuity and multi-resolution display. ....	46



Figure 4-3   Schematic diagram of the proposed multi-resolution foveated display. ....	47
Figure 4-4   The unfolded layout of the optical paths: a) display panel 1 and b) panel 2.....	49
Figure 4-5   The experimental photographs of the proposed multi-resolution foveated display with 4× resolution enhancement: a) displayed image; b) the magnified green square region in (a); c) the magnified blue rectangle region in (b); d) the magnified red rectangle region in (b). ....	50
Figure 4-6   The experimental photographs of the proposed multi-resolution foveated display with 5× resolution enhancement: a) displayed image; b) the magnified green square region in (a); c) the magnified blue rectangle region in (b); d) the magnified red rectangle region in (b). ....	51
Figure 4-7   The measured on-axis MTF for original and 4× resolution in angular space. Note that the MTF drops to 0.5 at 20 cpd and 72 cpd for the original and 4× resolution, respectively. ....	53
Figure 4-8   Working principle of PBD image shifter. (a) Top view of the LC director distribution in PBD. (b) Phase delay profile of a PBD with 15° deflect angle at $\lambda = 633$ nm for LCP and RCP, respectively. (c) Active driving to result in a switching between deflection and non-deflection states. (d) The polarization state change for the LCP wave deflected by PBD and reflected by mirror. ....	55
Figure 4-9   Optical setup of polarization interference exposure used in PBD fabrication. ....	56
Figure 4-10   Schematic diagram of the multi-resolution display with PBD image shifter.....	57
Figure 4-11   Multi-resolution display (text) with PBD as image shifter: a) high-resolution region in the center; b) magnified blue rectangle region in (a); c) shifted high-resolution region; d) magnified blue rectangle region in (c). ....	58

Figure 4-12   Multi-resolution display (picture) with PBD as image shifter: a) high-resolution region in the center; b) magnified blue rectangle region in (a); c) shifted high-resolution region; d) magnified blue rectangle region in (c). .....	58
Figure 5-1   Conceptual illustration of VAC: a) real object at far distance; b) real object at near distance; c) virtual object at far distance; d) virtual object at near distance. ....	62
Figure 5-2   Working principle of Pancharatnam-Berry phase lens. (a) Top view of the LC director distribution and (b) phase change profile of a PBL with $\pm 0.8D$ optical power for RCP and LCP, respectively .....	64
Figure 5-3   Optical behaviors of PBL. (a) PBL serves as a diverging lens for LCP light and (b) it is a converging lens for RCP light. ....	64
Figure 5-4   Configuration of the proposed polarization-multiplexed multiplane display system. ....	65
Figure 5-5   One example of polarization state change in the proposed polarization-multiplexing design. ....	67
Figure 5-6   Optical setup of polarization interference exposure used in PBL fabrication.....	68
Figure 5-7   Experimental photographs after polarization modulation. Target images: a) without CP, b) with right-handed CP and c) with left-handed CP. Experimental results: d) without CP, e) with right-handed CP, and f) with left-handed CP. ....	70
Figure 5-8   Experimental photographs of two image planes with letters ‘A’ and ‘B’. Camera focusing at a) virtual plane 1 and b) virtual plane 2. ....	70
Figure 5-9   Schematic diagram of the additive light-field rendering method.....	71

Figure 5-10   The rendered 2D images for an additive light field display. (a) image to be displayed virtual plane 1 and (b) virtual plane 2.....	72
Figure 5-11   Experimental photographs of two image planes with two cubes. The photographs captured with camera focusing at: a) front object and b) rear object.....	72
Figure 5-12   Experimental photographs of the multi-plane display at different viewing position: a) upper-left, b) upper, c) upper-right, d) left, e) central, f) right, g) lower-left, h) lower, and i) lower-right. ....	73
Figure 5-13   One example of hybrid space- and polarization-multiplexed four-plane display. ..	74
Figure 5-14   Experimental photographs of four image planes with four digits. The photographs captured with camera focusing at: a) the first focal plane, b) the second focal plane, c) the third focal plane and d) the fourth focal plane. ....	75
Figure 5-15   One example of hybrid time- and polarization-multiplexed three-plane display....	76

## LIST OF TABLES

Table 1: Simulated and measured dynamic contrast ratios of four test patterns. ....	11
Table 2: Required local dimming zone number for larger-size MVA-LCD TVs.....	21
Table 3: Layer structures of the six OLED samples we fabricated .....	29

## CHAPTER 1: INTRODUCTION

With the development of information technology (IT), the consumer electronics play more and more important roles in our daily lives, as we are becoming increasingly dependent on it and less willing to separate ourselves from them. From computer desktop, personal notebook, tablet to smartphone and smartwatch, consumer electronic devices are becoming smaller and smaller but more and more powerful. It has also revealed a clear trend shifting from “portable” to “wearable”. This is the reason of the rise of wearable devices, like fitness trackers, smart watches and head-mounted devices. Within all of these devices, display is always one of the key components, since it can provide abundant visual information, as the most important information output channel. Recently, head-mounted devices (HMD) have attracted a great deal of interest due to its potential applications [1-2] in entertainment, gaming, education, engineering, design, military training and medical surgeries, etc.

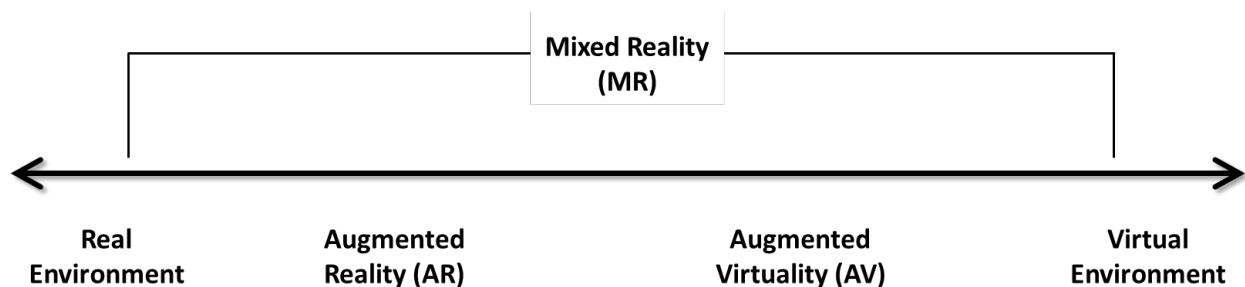


**Figure 1-1 | Representation of virtuality continuum.** Adapted from Milgram and Kishino [3].

Typically, HMDs include virtual reality (VR), augmented reality (AR) and mixed reality (MR). The VR display creates a totally digital world to replace the viewer’s real-world environment, while AR is trying to overlay digitally-created content into the viewer’s real world. In early years, mixed reality was defined as a rather general concept, which may cover both virtual

reality and augmented reality. Especially, Milgram and Kishino [3] defined a “virtuality continuum” in 1994, as presented in Fig. 1-1. In Milgram’s continuum definition, augmented reality and augmented virtuality are just subsets of the general mixed reality. However, currently the MR is more frequently referred to an advanced AR device which can seamlessly blends the real-world environment and digitally-created content with mutual interactions between real and digital worlds. To achieve this, simultaneous localization and mapping (SLAM) and depth tracking technologies needs to be applied to detect the natural environment and map display content with the real world. As for all of these HMDs, near-eye displays play very critical roles for providing immersive viewing experience for users.

### 1.1 Basis of near-eye display

A typical schematic layout of near-eye display system is plotted in Fig. 1-2. It mainly consists of an image source, an eyepiece lens and a viewer [4]. The image source is usually an information display panel. There are basically three different types of display image sources: 1) transmissive type, typically transmissive liquid crystal display (LCD) [5], which currently is also the mainstream technology for flat panel displays; 2) reflective type, including liquid crystal on silicon (LCoS) [6], digital light processing (DLP) [7] and laser beam scanner (LBS) based on micro-electro-mechanical systems (MEMS) [8], which are normally used in projection displays or micro-display systems like AR displays; and 3) emissive type, including organic light-emitting diode (OLED) [9], quantum-dot light-emitting diode (QLED) [10] and emerging micro-LED displays [11]. For virtual reality headsets, the transmissive LCD and self-emissive OLED are the leading technologies. For instance, Oculus Rift S (2019) uses LCD displays while HTC Vive Pro

(2018) and PlayStation VR (2016) are using OLED panels. While for augmented realities, form factor and lightweight are extremely important for commercial products. Therefore, micro-displays, like LCoS, DLP, LBS and micro-OLED, are currently dominating technologies. For example, Google Glass (2013) and Magic Leap one (2018) adopts LCoS as the micro-display, and HoloLens 2 (2019) uses laser beam scanning display system.

As plotted in Fig. 1-2, The eyepiece lens is used to move the virtual image plane to a fixed far distance to the viewer's eye, with magnifying the image from the display panel. Normally, the eyepiece lens directly determines the near-eye display performances, including angular resolution, field of view, depth location, image quality and distortion. Refractive-type lens based on glass or plastic are used in VR headsets. To reduce the weight of whole headset, some VR devices may use Fresnel lens (HTC Vive series) or hybrid Fresnel lens (Oculus Rift series).

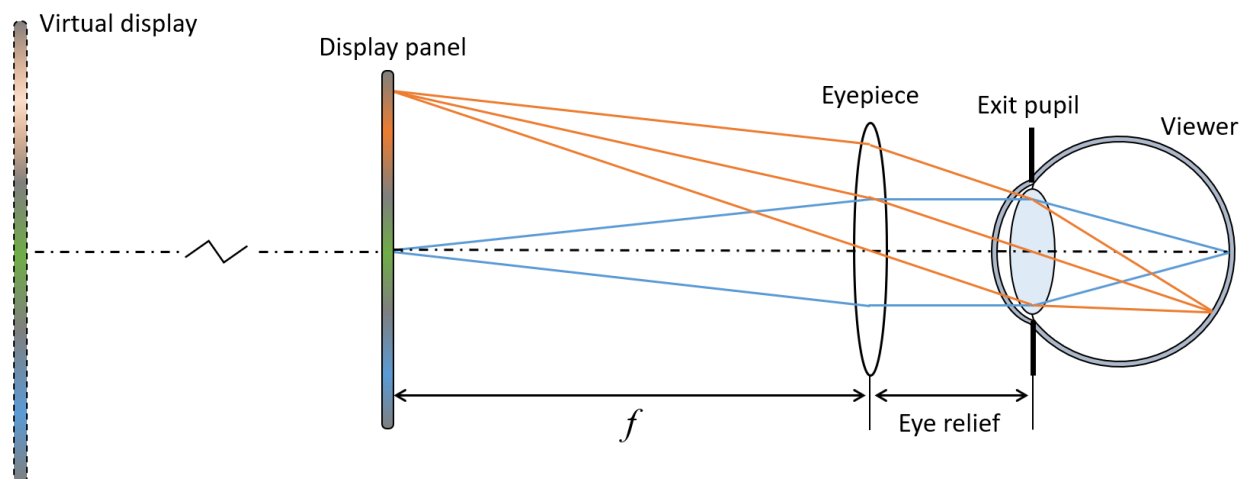


**Figure 1-2 | Schematic layout of a typical near-eye display system.**

A typical HMD device may also include other components. To support audio output, 3D audio is usually included to provide immersive sound effect in most of current VR and AR products. To detect the head location and orientation, a head tracker is integrated into the headsets. A three

degrees of freedom (3 DOF) tracker can only detect the x-y-z translations while six degrees of freedom (6 DOF) can even sense the rotations of head besides translations. As for the input device, usually a controller, or a gesture sensor, is provided for interaction.

## 1.2 Challenges and motivations

Both AR and VR displays have becoming very hot research topics over the past few years, especially after the release of Google Glass in 2013. However, the visual experience offered by current HMD headsets is still far below what we expect. Regarding to display performance of HMDs, we list three major challenges as below:

- 1) Limited dynamic range of display brightness and contrast. Our natural world can provide extremely wide dynamic range, from direct sunlight at daytime to star light at night. The luminance can vary from  $10^9$  to  $10^{-6}$  cd/m<sup>2</sup> with very high dynamic contrast [12-14]. However, no matter for mainstream LCD or OLED displays, it is very challenging to fulfill all the brightness requirements to reproduce the real world. As for VR display to mimic real-world environment, its HDR performance, especially the dark state, is extremely critical. While for AR see-through devices, the requirement of display peak brightness can be extremely strict in order to achieve high ambient contrast ratio [15-16].
- 2) Insufficient angular resolution. Most of current commercial VR displays can offer angular resolution of only 10~15 pixel per degree (ppd) with a field of view (FOV) around 110°. However, the angular resolution is far below human visual acuity: ~1 arcmin for a normal person with 20/20 vision [17]. Thus, users can still observe pixels and severe screen-door effect, which would greatly degrade the immersive experience of virtual contents. To



eliminate screen-door effect, at least  $4\times$  improvement on angular resolution is needed to match human-eye acuity.

- 3) Vergence-accommodation conflict (VAC) issue. Stereoscopic display based on binocular disparity is usually adopted in current VR headsets. Two different images are separately sent to the left and right eyes to generate the illusion of depth. However, stereoscopic 3D perception results in the well-known vergence-accommodation conflict (VAC), which remains one of major challenges for HMDs. Such a mismatch between vergence and accommodation distances is the main cause of visual discomfort and fatigue [18, 19] when wearing such a headset.

This dissertation will be mainly focused on possible solutions to above three challenges. In order to improve HDR performance, mini-LED backlit LCD and OLED displays are investigated, respectively in Chapter two and Chapter three. In Chapter four, a foveated display system is proposed to enhance the angular resolution by up to  $5\times$  while keep wide field of view, which can fulfill the requirements of human visual acuity. To overcome VAC issue, a multiplane display system with novel polarization multiplexing method is demonstrated in Chapter five.

## CHAPTER 2: MINI-LED BACKLIT LCD

### 2.1 Background

An HDR display should be able to exhibit a high contrast ratio (CR)  $>10^5:1$  in order to reveal details in both high and low brightness regions simultaneously. Both high peak brightness and excellent dark state are critical in order to achieve a good HDR display system [20-21]. Specifically, in flat panel displays, the bright state luminance is required to exceed 1000 nits, and the dark state should be below 0.01 nits [22]. However, both OLEDs and LCDs need substantial improvements to realize the HDR features. As to self-emissive OLED display, it exhibits intrinsically excellent dark state. While as a current-driven electroluminescent device, a higher peak brightness would require a higher current, which would inevitably compromise its operation lifetime. Therefore, how to enhance the optical efficiency is a significant topic for OLED development. LCD is a non-emissive display and requires a backlight unit, such as white light emitting diode (LED) or blue LED pumped quantum dots [23]. A major advantage of LCD is that it can achieve high brightness ( $>1000$  nits) by cranking up the LED luminance. However, a pitfall is its limited contrast ratio, which depends on the liquid crystal alignment and de-polarization of color filter array [24]. For example, a commercial multi-domain vertical alignment (MVA) LCD, mainly used in TVs, can provide  $CR \approx 5000:1$ , which is still  $20\times$  lower than the HDR requirement. Therefore, how to achieve good dark state is becoming an urgent task for LCD.

To improve dark state of LCDs, segmented LEDs are adopted in the LCD backlight unit, where the local zones can be independently dimmed to match the displayed image contents [25-26]. This so-called local dimming technique can effectively suppress the dark state light leakage

and greatly enhance the contrast ratio. The schematic layouts of conventional global-dimming and local-dimming LCD panels are plotted in Fig. 2-1.

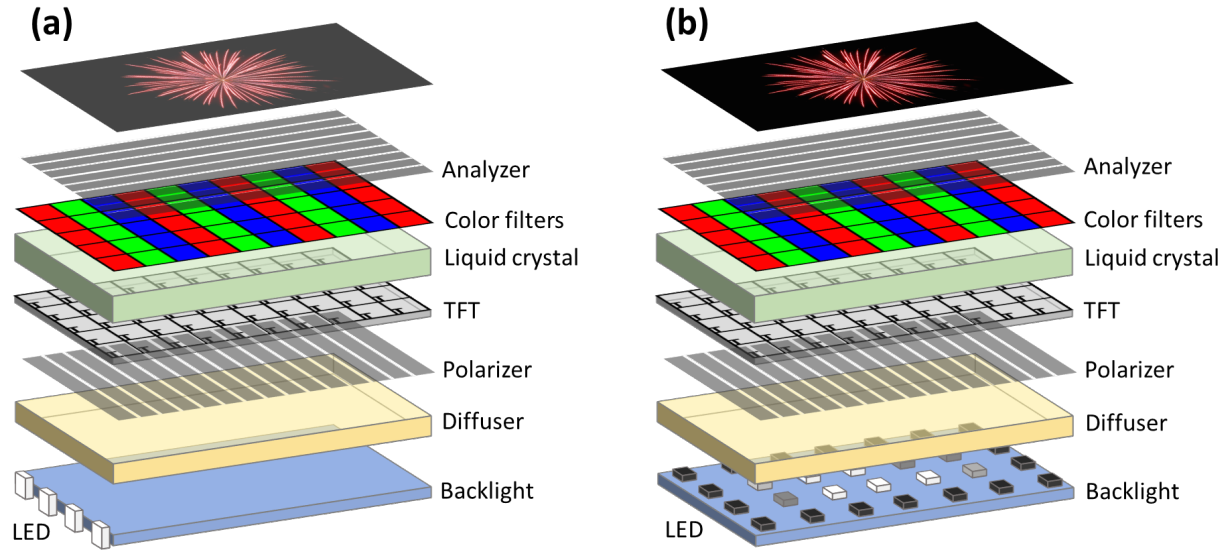


**Figure 2-1 | Schematic layouts of (a) conventional global-dimming LCD panel and (b) local-dimming LCD panel.**

Over the past several years, micro-LED and mini-LED for display applications have attracted much attentions [27-28]. Direct-view micro-LED with a chip size less than 100  $\mu\text{m}$  is considered as a revolutionary technology for future displays [11, 29]. However, the manufacturing yield of micro-LED mass transfer remains a big challenge [30]. On the other hand, mini-LED has a larger chip size (100~500  $\mu\text{m}$ ) than micro-LED and its fabrication is also much easier. Thus, mini-LED is an ideal backlight candidate to enable local dimming for LCDs. Besides the advantage on high brightness (>1000 nits), mini-LED backlight can provide more than 10,000 local dimming zones to achieve excellent HDR performance. In addition, due to the small dimension of mini-LED, it can offer freeform outline and narrow bezel, which is highly desirable for smartphone

applications [31]. However, until now, there is no detailed discussion on system modeling and performance evaluation of LCDs with mini-LED backlight.

## 2.2 System modelling

Figure 2-2 depicts the device structure of the LCD system with a direct-lit mini-LED backlight, which is not drawn to scale. The backlight unit consists of square-shaped mini-LED array with chip size  $s$  and pitch length  $p$ . For simplicity, we assume that all the mini-LEDs having the same angular emission pattern  $I_0(\theta)$ . In practical, different emission patterns can be applied for different application needs. Without losing generality, Lambertian emission is adopted in our simulation. Then a diffuser plate is applied to spread the light to obtain good spatial uniformity. In our simulation, we used the point spread function (PSF) theory [32] to model the light propagation from mini-LED backlight to LCD panel. The diffuser plate is utilized to widen both spatial and angular distributions. The bidirectional scattering distribution function (BSDF) can be used as an accurate description of the optical behaviors of diffuser plate. Here we can make a reasonable simplification. The angular distribution of the light travelling through the diffuser is assumed to be Lambertian distribution, i.e.  $I_d(\theta) \propto \cos(\theta)$ , for a strong diffuser. Moreover, this assumption also applies to some color conversion films, for instance phosphor or quantum-dot layer. The widened spatial distribution can be described by 2-D Gaussian function:

$$I_d(x, y) = \exp \left[ -\frac{(x-x_0)^2 + (y-y_0)^2}{2\rho^2} \right] \quad (1)$$

where  $(x_0, y_0)$  is the location of incident source point and  $\rho$  is the standard deviation of the spatial distribution. The parameter standard deviation  $\rho$  can be tuned to achieve good spatial uniformity.

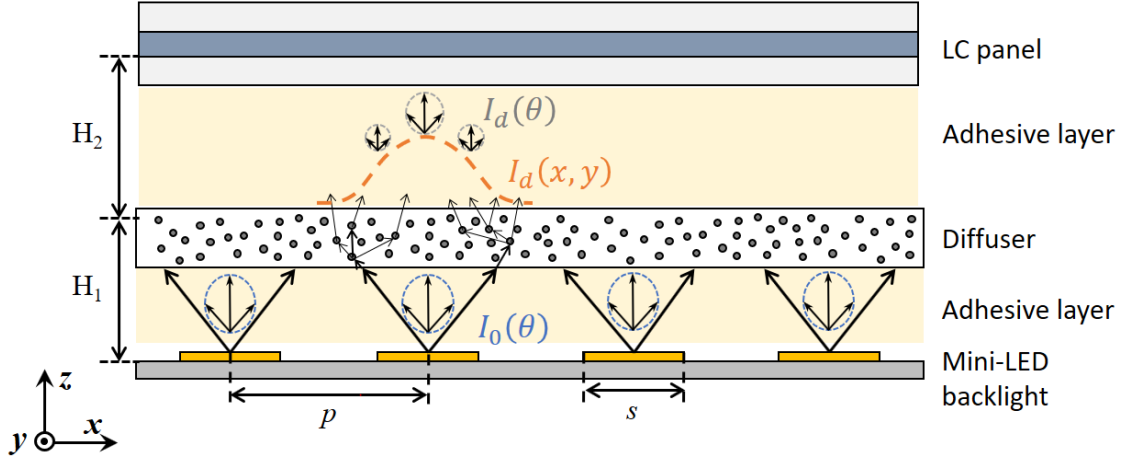


**Figure 2-2 | Schematic diagram of a mini-LED backlit LCD.**

In our simulations, the system settings are based on the device configuration reported in [31]. The dimensions of mini-LED array are set to be  $p = 1$  mm and  $s = 0.5$  mm, according to [31]. The effective light diffusion distances, by considering substrates and adhesive layers between backlight, diffuser plate and LCD panel are reasonably set as  $H_1 = 0.4$  mm and  $H_2 = 0.5$  mm in order to obtain good spatial uniformity. Then we simulate a 6.4-inch 2880×1440 LCD system with mini-LED backlight. The diffusion standard deviation  $\rho$  in Eq. (1) is adjusted to be  $\rho = 0.4$  mm in order to generate uniform luminance over the whole display panel. Typically, the edge of the backlight would be dimmer than the central region. Thus, we also set the backlight area (146 mm × 74 mm) slightly larger than the LCD panel (144 mm × 72 mm) to assure an excellent uniformity, especially for the edges.

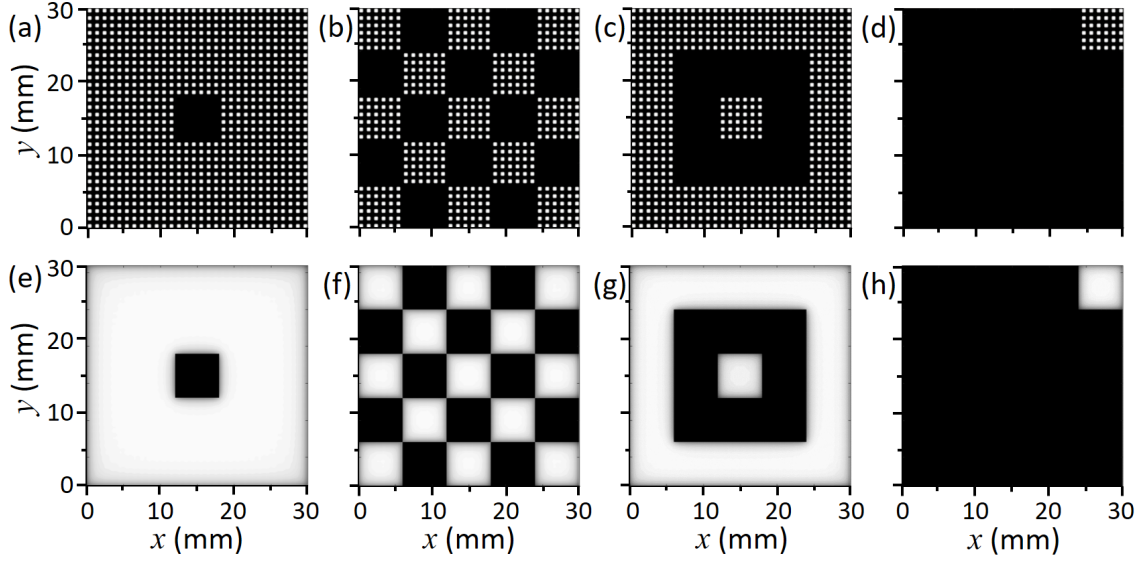


**Figure 2-3 | Simulated test patterns of mini-LED backlight.** Mini-LED backlight local dimming modulation with (a) pattern I, (b) pattern II, (c) pattern III, and (d) pattern IV. Simulated displayed images: (e) pattern I, (f) pattern II, (g) pattern III, and (h) pattern IV.

In order to validate our model, we simulated the abovementioned display system with local dimming technique, and then compared our results with the experimental data reported in [31]. According to the fabrication results from [31], this backlight has  $24 \times 12$  local dimming zones and each zone has  $6 \times 6$  mini-LEDs. Each local dimming zone can be modulated independently. The employed in-plane switching (IPS) LCD panel has a intrinsic  $CR \approx 1500:1$ . We investigated four test patterns, as Figs. 2-2(a)-(d) show. Their corresponding dynamic contrast ratios were calculated as well. Figs. 2-2(e)-(h) presents their corresponding displayed patterns after LC panel modulation. Table 1 summarizes the experimental and calculated dynamic CRs for four test patterns plotted in Fig. 2-3.

As described above, our simulation model can successfully predict the dynamic contrast ratio of a local dimming display system. While a complete simulation model should be able to simulate the displayed images and then to evaluate the HDR performance. Thus, our following

work is to further develop the model to simulate the final displayed images. The target is to make our model capable of relating the device structure to the final HDR display performance, especially the halo effect.

**Table 1: Simulated and measured dynamic contrast ratios of four test patterns.**

Pattern	I	II	III	IV
Simulated CR	15,094	46,547	32,245	31,590,212
Measured CR	~20,000	25,000~40,000	25,000~40,000	>3,000,000

As to the displayed image simulation, first we need to determine how to modulate the mini-LED backlight and LCD panel, respectively. Since our main focus here is on the halo effect, we use the Max-algorithm [12] and LC pixel compensation [33] to minimize the clipping effect. As for a target image to be displayed using our system, we first divide the image into several zones according to the size of local dimming zone. Within each zone, the maximum luminance of the target image is used to determine the luminance of the corresponding mini-LED backlight zone. With the proposed simulation model, the luminance distribution of the light incident on the LC layer can be calculated. Then we can determine the LC panel’s transmittance by the ratio between the luminance on the LC layer and that of the target image. The LED backlight modulation depth is reasonably set to be 10 bits while the LC panel transmittance modulation is 8 bits. Here we give an example of “Candle” image in the dark background, as illustrated in Fig. 2-3. The mini-LED backlight modulation is depicted in Fig. 2-3(a), and the simulated luminance distribution incident on the LC layer is presented in Fig. 2-3(b). By considering the LC panel modulations through

R/G/B channels respectively, we can obtain the final displayed full-color image, as Fig. 2-3(c) shows.

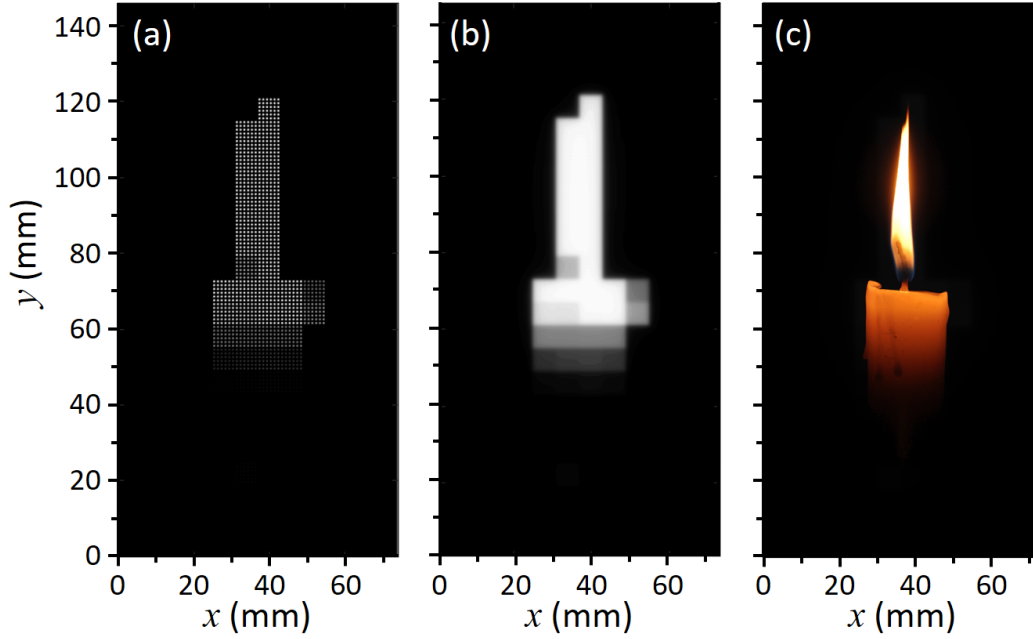


**Figure 2-4 | Displayed image simulation.** (a) mini-LED backlight modulation; (b) luminance distribution of the light incident on LC layer, and (c) displayed image after LCD modulation.

Although it is not easy to observe in the printed Fig. 2-3(c), the halo around the bright candle area still exists, due to the light leakage of LC panel (CR~1500:1). Thus, we may need a quantitative evaluation metric for the halo effect. In our analysis, both brightness and color performance need to be taken into consideration. Therefore, the Peak Signal-to-Noise Ratio (PSNR) in the CIE  $L^*a^*b^*$  color space can be used in our evaluations [34-35]. In the LAB color space,  $L^*$  describes the lightness value,  $a^*$  represents the green-red component, and  $b^*$  represents the blue-yellow component. Based on that, we can define the color difference in  $L^*a^*b^*$  color space, which is the perceived difference between two colors, considering both luminance and chrominance differences:



$$\Delta E = \sqrt{\Delta L^{*2} + \Delta a^{*2} + \Delta b^{*2}} \quad (2)$$

where  $\Delta L^*$ ,  $\Delta a^*$  and  $\Delta b^*$  are the differences between the displayed image and target image. With that, we can define the *LabPSNR* by the following equation [32]:

$$LabPSNR = 10 \times \log_{10} \left[ \frac{(\Delta E_{\max})^2}{\frac{1}{mn} \sum_{i=1}^n \sum_{j=1}^m \Delta E(i, j)^2} \right] \quad (3)$$

where  $m$  and  $n$  are the image resolution (2880×1440 in our example) and  $\Delta E_{\max}$  is the difference between black and white. In our simulations, the normalized  $\Delta E_{\max}$  is set to be 100. Then with *LabPSNR* as the evaluation metric, we are able to quantify the difference between displayed image and target image.

In Fig. 2-4, the backlight has only 288 local dimming zones and the LCD contrast ratio is 1500:1. In the following simulations, we will discuss how the local dimming zone number and LCD contrast ratio influence the final display performance. The  $L^*a^*b^*$  color difference  $\Delta E$  of the displayed images with different local dimming zones are presented in Fig. 2-5. The contrast ratios in Fig. 2-5 are all kept at 1500:1. From Figs. 2-5(a) to 2-5(d), the number of local dimming zones is 18, 288, 1152 and 10368, respectively. The corresponding mini-LED number in each zone is 24×24, 6×6, 3×3 and 1×1. From Figs. 2-5(a)-(d), we can find a clear trend: the displayed image distortion decreases as the local dimming zone number increases. Especially, the halo area around the bright candle dramatically decreases. The calculated *LabPSNR* is improved from 39.9 dB to 48.8 dB as well.

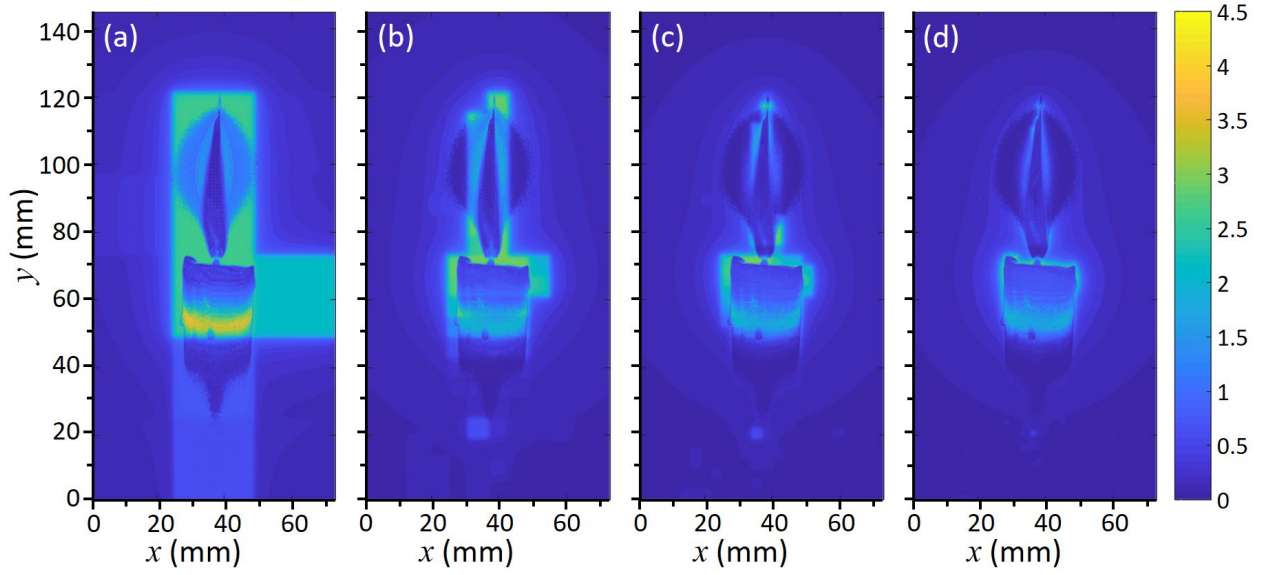


**Figure 2-5 | Color difference  $\Delta E$  for different local dimming zone numbers: a) 18; b) 288; c) 1152 and d) 10368.**

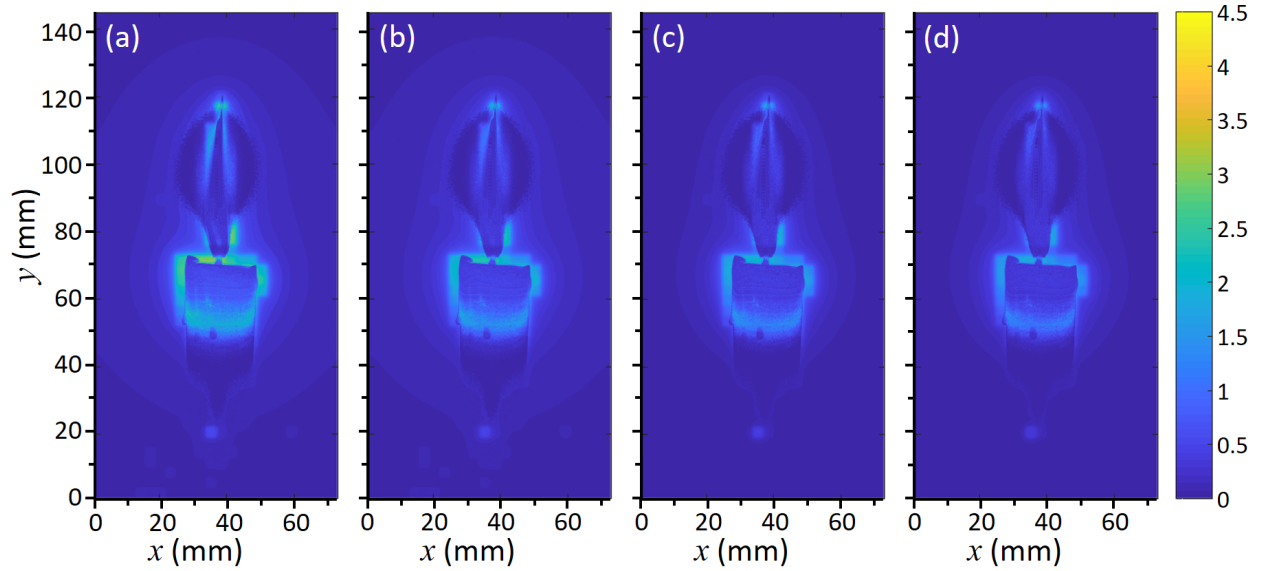


**Figure 2-6 | Color difference  $\Delta E$  for LCD contrast ratios: a) 1500:1; b) 2500:1; c) 3500:1 and d) 4500:1.**

Besides the local dimming zone number, LCD contrast ratio is another important factor affecting the final HDR performance. Therefore, we also analyze the influence of intrinsic LCD

contrast ratio. Figure 2-6 presents the simulated  $\Delta E$  of the displayed images with CR increasing from 1500:1 to 4500:1. Backlight local dimming zone number is set to be 1152 in the simulations illustrated in Fig. 2-6. As depicted in Figs. 2-6(a)-(d), the halo area does not change while the color distortion  $\Delta E$  value decreases as the LC contrast ratio increases. The *LabPSNR* increases from 46.9 dB [Fig. 2-6(a)] to 51.6 dB [Fig. 2-6(d)]. From Fig. 2-5 and Fig. 2-6, the impacts of local dimming zone number and LCD contrast ratio can be clearly distinguished. The dimming zone number mainly affects the halo area, while LCD contrast ratio influences the local image distortion.

### 2.3 Subjective experiment

As discussed in Section 2.2, more local dimming zones and higher LC contrast ratio can reduce the halo effect and improve the display performance. However, the minimum number for dimming zones and LC contrast ratio have not been clearly quantified. To answer this question, subjective experiments were then designed and carried out to measure human visual perception limit of halo effect. With visual perception limit obtained, the required local dimming zone number for an ideal HDR display with indistinguishable halo effect could be estimated.

Ten HDR images were employed in our experiments. As shown in Fig. 2-7, all of the pictures have highlight spots and dark areas qualifying the HDR content requirement. In the meantime, the diversity of the image content was also considered. Some pictures are generally bright [Figs. 2-7(a), (c), and (g)], while some have a large portion of dark areas [Figs. 2-7(d), (f) and (j)]. Moreover, in Figs. 2-7(b), (d) and (f), the high-luminance pixels are finely disseminated in the dark background. While in Figs. 2-7(c) and (h)-(j), there are relatively concentrated bright and dark blocks.



**Figure 2-7 | HDR target pictures used in the subjective experiment:** a) Beach, b) City light, c) Christmas, d) Firework, e) Tower, f) Stars, g) Sunset, h) Waffle house, i) Lamp, and j) Candle.

Based on the model described in Section 2.2, we simulated the displayed images by LCD systems with mini-LED backlight. Ten different local dimming zone numbers (1, 2, 8, 18, 72, 288, 648, 1152, 2592 and 10368) and seven LC contrast ratios (1000:1, 1500:1, 2000:1, 3000:1, 4000:1, 4500:1 and 5000:1) were applied to each picture, generating seventy different rendering conditions in total. In the following experiments, 70 simulated images were selected covering all the rendering conditions. Diverse image contents were evenly distributed in different number of local dimming zones and different LC contrast ratios.

Eleven people with normal or corrected normal vision participated in our subjective contrast experiments. Their ages range from 22 to 28 years old with an average value of 25.5. The experiments were carried out on each observer independently. In a dark room, two OLED panels (Samsung Galaxy S8, panel size 5.8", resolution 2960x1440) were placed at 25 cm (least distance of distinct vision) away from the observer's eyes. One of the OLED panels displays a simulated displayed image by a mini-LED-backlit LCD system while the another one displays the original target image. The observers were asked to select the image they preferred between the two displayed images. In total, seventy sets of image pairs were displayed to each observer. To avoid the influence of prejudgment and viewing angle, the target images were randomly displayed on one of the smartphones between different sets of image pairs, and the location of two smartphones was exchanged for different observers.

## 2.4 Experimental results

Our experimental results are summarized in Fig. 2-8. The perceived difference stands for the ratio of observers, who are able to distinguish the target images from the simulated displayed images by the mini-LED-backlit LCD system. The *LabPSNR* values of the 70 rendered images scatter over a wide range. In Fig. 2-8, the yellow bar denotes the averaged perceived difference ratio in each *LabPSNR* range and the black error bar marks the standard deviation of the experimental data. In our fitting, we assume that probability density follows normal distribution and the cumulative function of normal Gaussian distribution is used as the fitting function. The fitting curve is plotted as the blue solid line in Fig. 2-8. From the fitting result, for a displayed image with *LabPSNR* > 47.4 dB, only less than 5% of people could perceive the difference between

the displayed image and target image. The good match between fitting curve and experimental data implies that *LabPSNR* could be used to predict the human perceptibility of the displayed images.

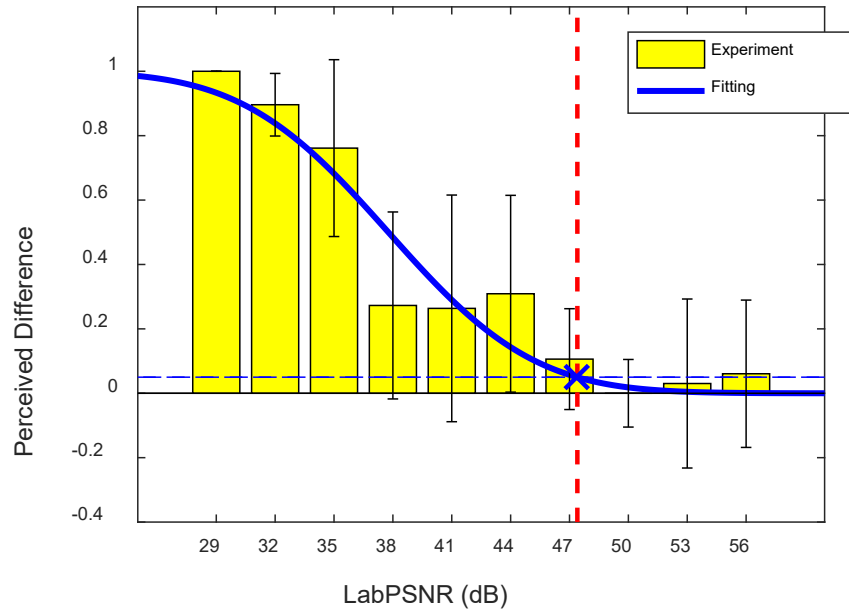


**Figure 2-8 | Subjective experiment results of perceived image difference.**

Having obtained the required *LabPSNR* value, our next step is to estimate the requirements of the display system. It is denoted that the improvement by local dimming technology is dependent on the image content. It is undeniable that as for certain images with a large portion of high spatial frequency component, pixel-level local dimming is necessary for faithful reproduction. However, for most HDR contents, local dimming technology would help greatly. Therefore, in our discussion, we mainly focus on the cases in which local dimming works effectively. Fig. 2-9 plots the average *LabPSNR* values of the pictures with obvious display quality improvement. As expected, *LabPSNR* can be improved by increasing dimming zone number and LCD's contrast ratio. Let's use 47.4 dB as the criterion to estimate the required dimming zone number. As to a

LCD with intrinsic  $CR \approx 1000:1$ , even 10,000 local dimming zones is still inadequate. For a LCD with  $CR \approx 2000:1$ , for instance fringing-field switching (FFS) mode, the required zone number is reduced to 3000. For a LCD with  $CR=5000$  (e.g. MVA), an unnoticeable halo effect can be achieved at only  $\sim 200$  local dimming zones. Our obtained results are consistent with the experimental results reported by Samsung in 2016 [36]. We believe this work shed new light for optimizing the HDR displays with mini-LED backlit LCDs.

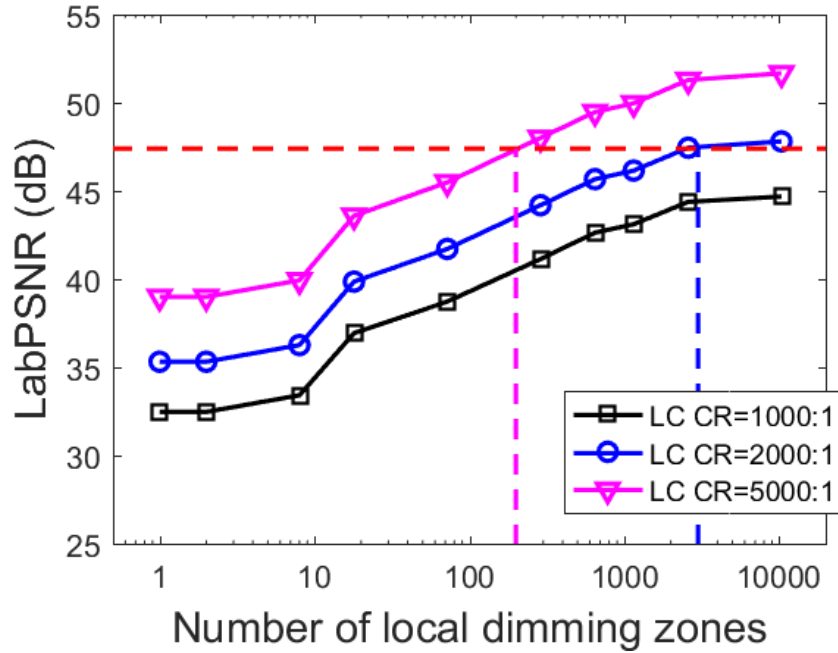


**Figure 2-9 | Simulated *LabPSNR* for different mini-LED backlit LCDs.**

## 2.5 Discussion

In above sections, our simulations and experiments are all based on the small-size smartphone displays with viewing distance at 25 cm. Actually, our analysis and conclusion can also be applied to display devices with different sizes and resolutions. The basic concept is to



convert our results from spatial domain to angular domain. In this discussion section, we give two examples, one for large-size TVs, and another for near-eye displays.

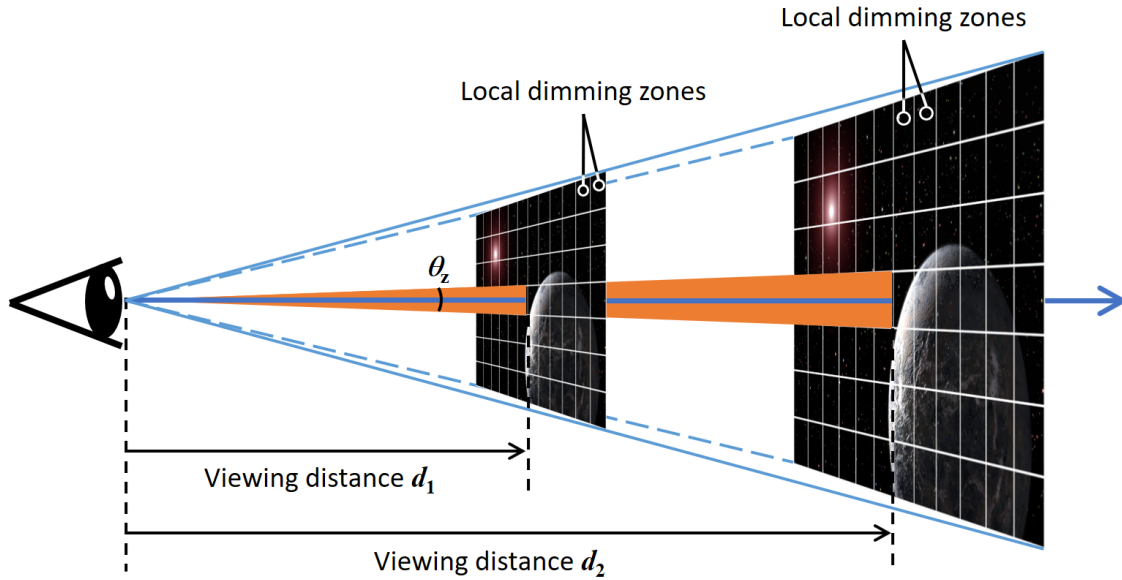


**Figure 2-10 | Conceptual diagram of scaling up display size based on same angular size.**

MVA mode has been widely used for large-size LCD TVs. Based on our settings of a 6.4-inch mobile display at 25-cm viewing distance, ~200 local dimming zones is needed for an MVA LCD with CR= 5000:1. Under such a condition, the angular distance of two adjacent local dimming zones is calculated to be  $\theta_z = 1.65^\circ$ . That is to say, for human eyes, the required angular density of local dimming zones should be over 0.606 zones per degree (zpd). Based on this information, we are able to scale up the display size and resolution, as shown in [Fig. 2-10](#).

Two MVA panels with CR= 5000:1 were considered as examples: 1) 65-inch TV with 4K (3840×2160) resolution and 2) 85-inch TV with 8K (7680×4320) resolution. Because the human-perceived display performance depends on the viewing distance from the panel to the observer, here, we consider two scenarios. The first case is the minimum viewing distance calculated by an



angular pixel density of 60 pixels per degree (ppd), which corresponds to the human visual acuity of 1 arcmin for a normal person with 20/20 vision. As shown in Table 2, the calculated minimum viewing distance is 1.29 m for the 65-inch 4K TV and 0.84 m for the 85-inch 8K TV. We find that the required dimming zone number for the 8K TV (3432 zones) is four times higher than that of the 4K TV (858 zones). The reason is that under the same angular pixel density the pixel number in one dimming zone is fixed as:  $(60 \text{ ppd} / 0.606 \text{ zpd})^2 = 992$  pixels per zone. Therefore, the required zone number is proportional to the panel pixel number. The second distance considered here is the optimum viewing distance, at which the display occupies a  $40^\circ$  field of view (FOV) for the viewer. As demonstrated in Fig. 2-10 and Table 2, regardless of the panel size and resolution, the two panels occupying the same FOV have the same requirement on dimming zone number (364 zones). Another information extracted from Table 2 is that a shorter viewing distance usually requires more local dimming zones due to more distinguishable details.

**Table 2: Required local dimming zone number for larger-size MVA-LCD TVs.**

65" 4K TV (3840×2160)				85" 8K TV (7680×4320)			
Viewing distance	FOV	PPD	Required zones	Viewing distance	FOV	PPD	Required zones
1.29 m	58.4°	60.0	~858	0.84 m	96.3°	60.0	~3432
1.98 m	40.0°	92.1	~364	2.59 m	40.0°	184.1	~364

Normally, FFS mode is adopted in near-eye VR displays, considering its advantages on high resolution applications [37-38]. As discussed in Section 2.4, the FFS mode has intrinsic contrast ratio around 2000:1. Thus, the required angular distance between two adjacent local dimming zones is calculated to be  $\theta_z = 0.4^\circ$ . Then, we can calculate the required local dimming zone number based on the whole field of view and required angular distance  $\theta_z = 0.4^\circ$ . For example,

for a VR with  $120^{\circ}(\text{H}) \times 90^{\circ}(\text{V})$  FOV, the required local dimming zone number would be  $300 \times 225$ . Such a calculation can be applied to different VR designs and also other LC display applications.

## 2.6 Summary

In this chapter, we investigated the one promising approach to high dynamic range display, namely mini-LED backlit LCD with local dimming technique. The LCD technology exhibits good potential to achieve high peak brightness, while its dark state is limited by LC molecule alignment. To enhance the dark state of LCD, we proposed to use mini-LED as the local dimming backlight. Thus, the displayed brightness of each pixel is modulated first by mini-LED backlight and then LC panel carries out the second modulation. So, the whole system's contrast ratio would be greatly enhanced.

To evaluate the display HDR performance, we built a simplified simulation model for LCD system with mini-LED backlight in Section 2.2. We verified our simulation model with the measured results. From our analysis, the halo effect can be reduced and higher image fidelity can be achieved, by increasing LC panel's intrinsic CR or number of local dimming zones. In Section 2.3, we carried out subjective experiments to determine the human visual perception limit of halo effect:  $LabPSNR \sim 47.4$  dB. Then in Section 2.4, based on the visual perception limit, we are able to further estimate the requirements of local dimming zone number: over 200 local dimming zones for high CR  $\approx 5000:1$  (MVA) LCD panels, and more than 3000 dimming zones for CR  $\approx 2000:1$  (FFS) LCDs. These findings can provide valuable guidelines for mini-LED backlit LCD system designs. In Section 2.5, we give two examples to show how to apply our results to different display

systems, including larger-size TVs and near-eye VR displays. We believe that this work paves the way to achieve excellent HDR display with mini-LED backlit LCD panels.

## CHAPTER 3: ORGANIC LIGHT-EMITTING DIODE

### 3.1 Background

Besides excellent dark state, high peak brightness is also another critical requirement for HDR displays, especially for the optical see-through AR displays. For most of current see-through ARs, the basic construction normally consists of an image source, magnifying optics, and an optical combiner [39] to overlay digitally-created content into the viewer's real world. Typical optical combiners may include beam splitter (Google Glass), partial mirror (Meta 2), freeform prism (NED+), partial reflector array (Lumus) and grating-based waveguide (HoloLens 1, 2 and Magic Leap One). As to the AR displays with partial reflector combiner, the optical efficiency may achieve around 50%. While for waveguide-type ARs, optical efficiency is typically lower than 10% [39]. That makes the brightness requirement even more challenging, considering the ambient contrast ratio [26].

OLED display [9] exhibits advantages in true black state, fast response time, color purity and flexibility, in comparison with LCD. OLED now is becoming the mainstream for achieving HDR display with big advantages on dark state. While it is suffering from the limitations from high brightness and operation lifetime. Thus, improving optical efficiency has become a very important task for OLED displays. In order to enhance optical efficiency and color purity, top-emitting OLED with two metallic electrodes utilizing strong microcavity resonance has been widely adopted [40-41], especially in smartphone displays. Although microcavity effect helps improve optical efficiency and narrow the emission spectra, a clear trade-off is the angular color shift at large viewing angle. Due to Fabry-Perot resonance, the trade-offs between optical

efficiency, color purity, and angular color shift inevitably exist. How to optimize the device performance becomes a very important topic. Our target is to get high optical efficient while keeping relatively low angular color shift.

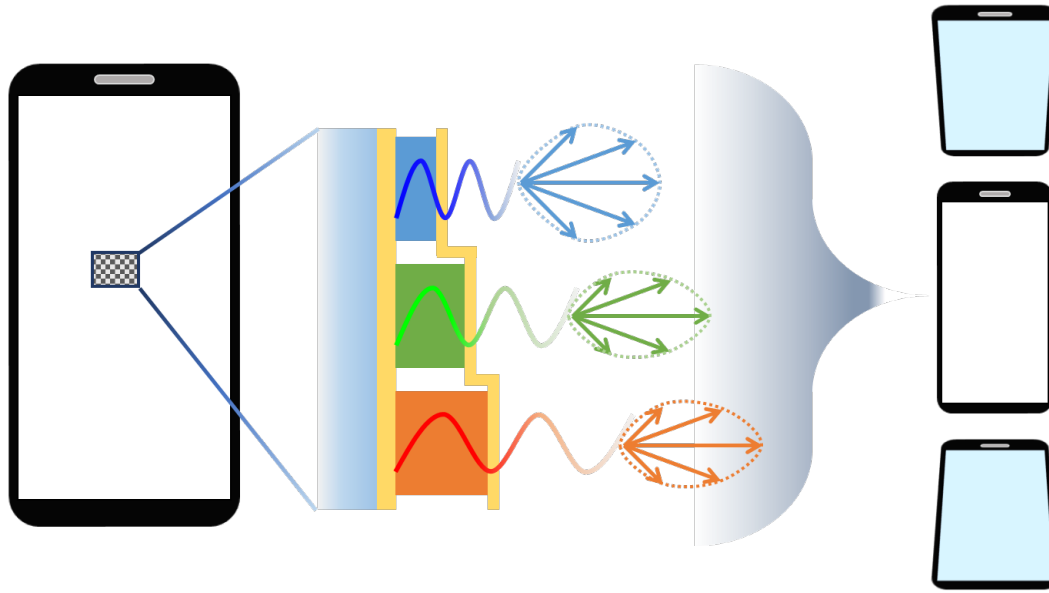


**Figure 3-1 | Mechanism of angular color shift of mixed color in an RGB-OLED display.**

As for the RGB OLED display system, color shifts actually originate from two factors [42]. The first one is directly related to the microcavity resonance. For each individual subpixel, its emission wavelength would shift toward a shorter wavelength as viewing angle increases, which is known as “blue shift” in an optical cavity. The angular color shifts of RGB primary colors can be clearly explained by blue shift. However, the primary colors usually only account for a small portion of the displayed images. The majority are those colors created by mixing RGB colors with different ratios. As to the mixed colors, there arises another non-negligible or even more critical factor. The mismatched angular emission distributions of RGB OLEDs can also result in angular color shift. For instance, if the angular distributions of red and green subpixels decline faster than

that of blue, the white point of the display would look bluish at large viewing angle, as depicted in Fig. 3-1. Therefore, to analyze the color shift of RGB OLED displays, these two factors, namely microcavity resonance effect and angular distribution mismatch, need to be taken into consideration simultaneously. Some prior arts have discussed the angular color shift of monochrome OLEDs [43-45], where only the microcavity effect needs to be considered. Very few system-level investigations on the angular color shift of RGB OLED displays has been reported.

### 3.2 Simulation modelling

In our following analysis, we need to examine not only optical efficiency but also emission spectra at each viewing angles. Thus, we use the rigorous dipole model for planar OLED structure, which describes the emission characterization of isotropic emitter within a multilayer medium. The thin film multilayer can be first simplified to a three-layer structure by the transfer matrix approach [46] or iterative calculation [47]. The emitters in OLED emitting layer are modelled as randomly oriented dipoles. Both transverse magnetic (TM) and transverse electric (TE) waves need to be taken into consideration. The quantitative power dissipation density  $K$  of randomly oriented dipoles can be expressed by [47-48]:

$$K(k_x, \lambda) = \frac{1}{3} K_{TMv} + \frac{2}{3} (K_{TMh} + K_{TEh}), \quad (4)$$

where the subscripts  $v$  and  $h$  stand for the vertical and horizontal dipoles, respectively, and  $k_x$  is the in-plane wave vector. The detailed description of each term in Eq. (4) can be found in [47-48]. The power dissipation density  $K(k_x, \lambda)$  actually describes complete information about OLED emission. We can obtain optical efficiency, spectral and angular distributions from  $K(k_x, \lambda)$ .

Optical outcoupling efficiency of OLEDs can be evaluated by the dipole model [47]. The external quantum efficiency (EQE) is defined as [49]:

$$EQE = \eta \cdot IQE = \eta \cdot \gamma \cdot \eta_{S/T} \cdot q_{eff}, \quad (5)$$

where  $\eta$  is the optical outcoupling efficiency, and  $IQE$  is the internal quantum efficiency, which is the product of effective quantum yield  $q_{eff}$ , charge carrier balance  $\gamma$ , and singlet/triplet capture ratio  $\eta_{S/T}$  [49-50]. In this chapter, our major focus is the optical outcoupling efficiency of OLED. Thus, without losing generality let us assume the  $IQE$  to be 100%. Different optical channels are then extracted from power dissipation  $K$  by the in-plane wave vector  $k_x$  [47-48]. Detailed descriptions of these optical channels are listed as follows:

- 1) Direct emission or air mode with  $0 < k_x < k_0 \cdot n_{air}$  ( $k_0 = 2\pi/\lambda$  is the vacuum wave vector), indicating the light directly emitting into air.
- 2) Substrate mode with  $k_0 \cdot n_{air} < k_x \leq k_0 \cdot n_{sub}$ , depicting the light trapped in glass substrate due to total internal reflection (TIR) in the interface between air and glass substrate.
- 3) Waveguide mode with  $k_0 \cdot n_{sub} < k_x \leq k_0 \cdot n_{eff}$ , describing the light guided inside the OLED active layers, where  $n_{eff}$  is the equivalent refractive index [47-48] of the organic layers and transparent electrode. (Note: the reflective metal electrode and the glass substrate are not included)
- 4) Surface plasmons mode with  $k_0 \cdot n_{eff} < k_x$ , corresponding to the evanescent wave at the organic/metal interface.

Equation (4) only gives the power dissipation at a single wavelength. To further evaluate the spectral and angular distributions, we can take the photoluminescence (PL) spectra  $S(\lambda)$  as the weight ratio [47, 49]. In an OLED device, the substrate thickness is usually in the order of

millimeter. We can reasonably assume that the optical interference effects play no role in the large scale. Therefore, the substrate can be first assumed as a semi-infinite medium in our dipole model simulations. Next, the air-substrate interface can be calculated by Fresnel equations. Once the respective spectral and angular distributions of RGB OLED emissions are obtained, we can calculate the CIE coordinates for the primary and mixed colors. Since the CIE coordinate value is quite sensitive to the spectrum profile, the accuracy of EL simulation becomes critical in our case. Thus, the wavelength dispersion of refractive index of each layer must be considered as well. More detailed theoretical description and simulation process of OLED emission have been exhaustively discussed in previous publications [47-49]. All the simulations carried out in this work are based on our home-made Matlab code. We also compared and verified this simulation model with some commercial software packages RSoft and FDTD solutions.

### 3.3 Experimental verification

Firstly, to validate that our simulation model can precisely calculate the color shift of OLED devices, we carried out some verification experiments. We fabricated two groups of OLED devices with different strength of microcavity effect. The first group includes 3 strong-microcavity OLED samples, with aluminum (Al) as both reflective cathode and semi-transparent anode. While for the weak microcavity group (also 3 samples), indium tin oxide (ITO) was adopted as the transparent anode. In all the six OLED samples, we used *N, N*-Bis (naphthalen-1-yl)-*N, N*-bis (phenyl) benzidine (NPB), 4,7-diphenyl-1,10-phenanthroline (BPhen), and LiF as hole transporting layer (HTL), electron transporting layer (ETL), and electron injection layer (EIL), respectively. Green emitting material tris-(8-hydroxyquinoline) aluminum (Alq<sub>3</sub>) was employed



as the emissive layer (EML). As for the strong microcavity group,  $\text{MoO}_3$  was inserted between semi-transparent electrode and NPB as hole injection layer (HIL). Detailed layer structure of the OLED devices we fabricated are summarized in Table 3. The ETL thickness of both weak microcavity (denoted as devices 1/2/3) and strong microcavity (denoted as devices 4/5/6) OLEDs varies from 40 nm, 60 nm to 80 nm.

**Table 3: Layer structures of the six OLED samples we fabricated**

Sample	Anode		HIL	HTL	EML	ETL	EIL	Cathode
	ITO	Al	$\text{MoO}_3$	NPB	$\text{Alq}_3$	BPhen	LiF	Al
1						40		
2	80	--	--	40	10	60	1	100
3						80		
4						40		
5	80	20	20	40	10	60	1	100
6						80		

Unit: nm.

We measured the EL emission spectra of these six OLED devices at different viewing angles, from  $0^\circ$  (normal direction) to  $80^\circ$ . Measured results are plotted in Figs. 3-2(a-c) (weak cavity) and Figs. 3-3(a-c) (strong cavity), respectively. As depicted in Fig. 3-2, the weak microcavity OLEDs show a relatively broad spectral bandwidth, with less blue shift at large viewing angles. While for the strong microcavity OLEDs shown in Fig. 3-3, their EL spectra are much narrower than those of weak microcavity OLEDs, and a clear blue shift is observed for devices 4, 5 and 6. Accurate simulations were then performed, based on the theoretical model described in Section 3.2. The wavelength-dependent complex refractive indices of the OLED layers were measured by ellipsometry, and then used in our simulations. The simulated results are

presented in Figs. 3-2(d-f) and Figs. 3-3(d-f). Excellent agreements between experiment and simulation have been achieved, no matter for weak microcavity [Fig. 3-2] or strong microcavity OLEDs [Fig. 3-3].

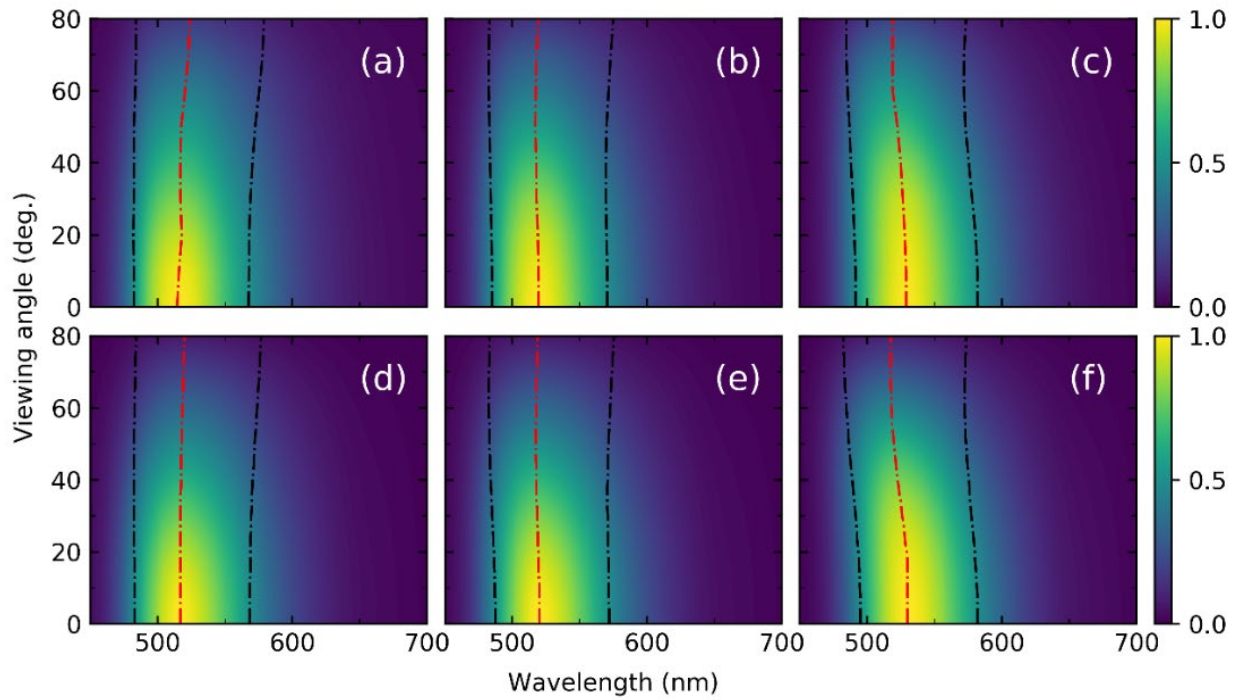


**Figure 3-2 | EL spectra of weak cavity OLEDs at different viewing angles.** Measured results: a) device 1; b) device 2 and c) device 3. Simulated results: d) device 1; e) device 2 and f) device 3.

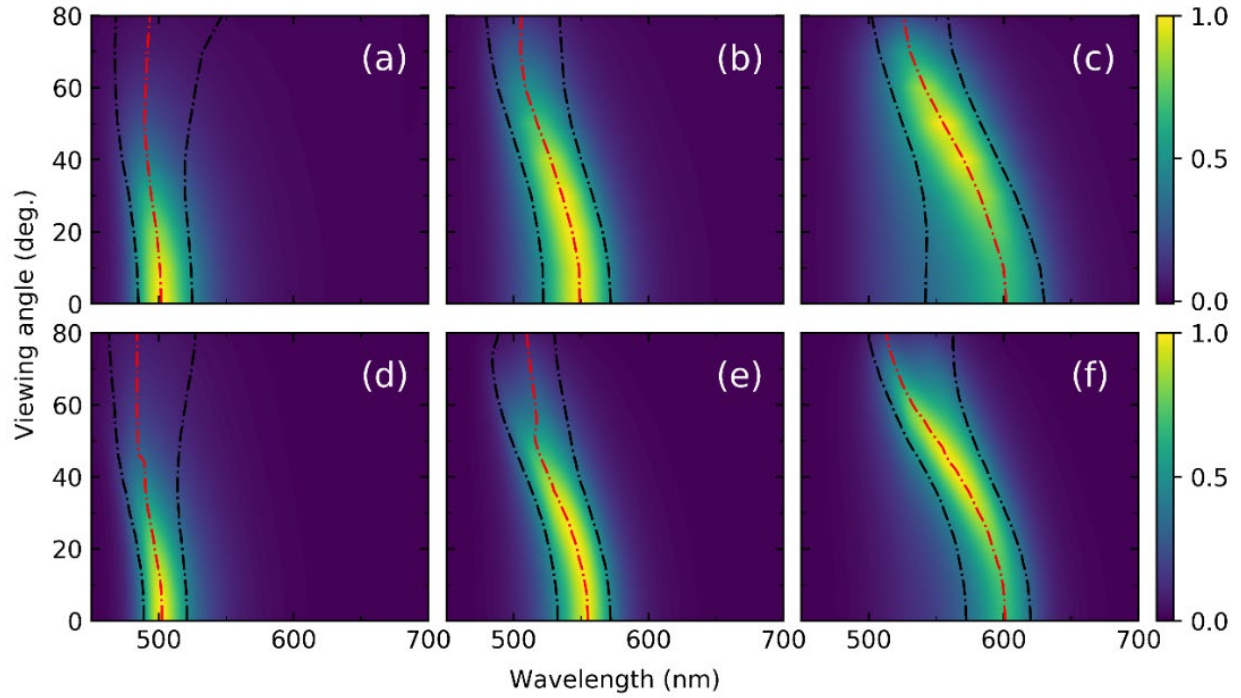


**Figure 3-3 | EL spectra of strong cavity OLEDs at different viewing angles.** Measured results: a) device 4; b) device 5, and c) device 6. Simulated results: d) device 4; e) device 5 and f) device 6.

As discussed above, both angular distribution mismatch and microcavity resonance effect contribute to angular color shift. Fig. 3-4 plots the angular distributions of the emission intensity for six OLED samples. Simulated and measured results are also compared in order to validate our simulation model. Excellent agreements are again obtained as Fig. 3-4 depicts.

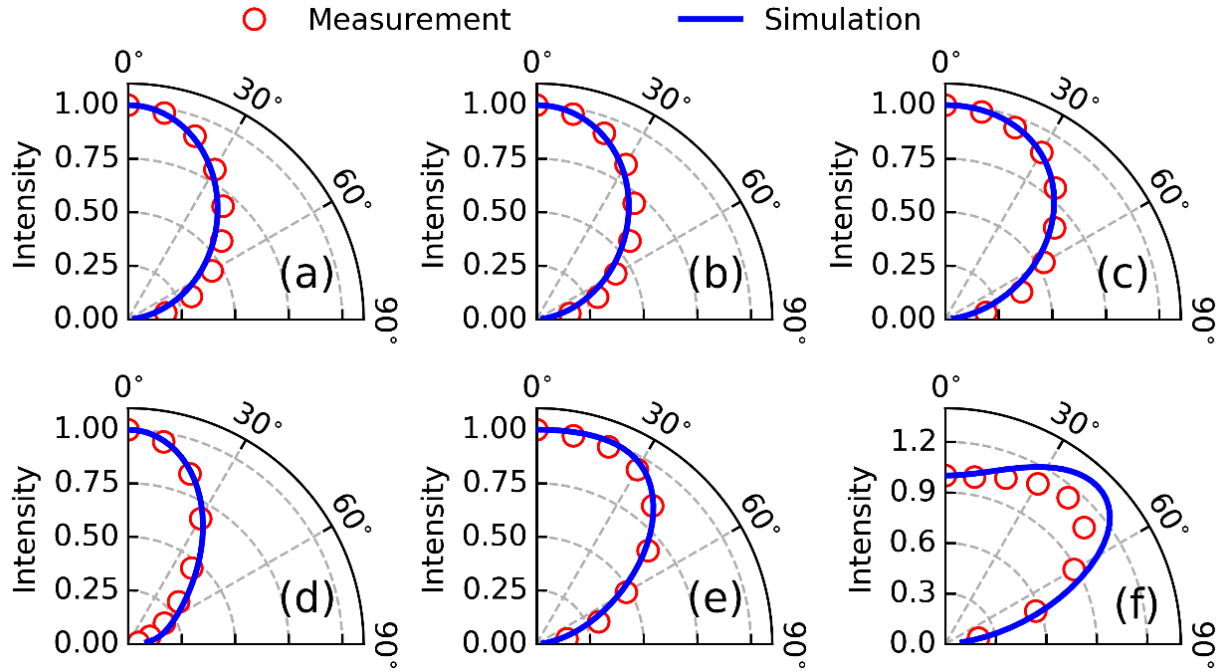


**Figure 3-4 | OLED EL emission intensity angular distributions:** a) device 1; b) device 2; c) device 3; d) device 4; e) device 5; and f) device 6.

To evaluate color shift quantitatively, we calculated the CIE coordinate values as well. In this chapter, all the colors are described in CIE1976 color space instead of CIE1931 color space, because CIE1976 color space is more perceptually uniform and is designed for color difference evaluation [34-35]. The calculated CIE coordinate values of the six OLED samples are shown in Fig. 3-5. The three weak-microcavity OLED samples exhibit a much weaker angular color shift [Figs. 3-5(a-c)] than the strong microcavity ones [Figs. 3-5(d-f)]. These good agreements shown in Fig. 3-5 clearly demonstrate that our simulation model can provide an accurate prediction on the angular color shift, of any OLED device, in spite of its microcavity strengths and resonance lengths.

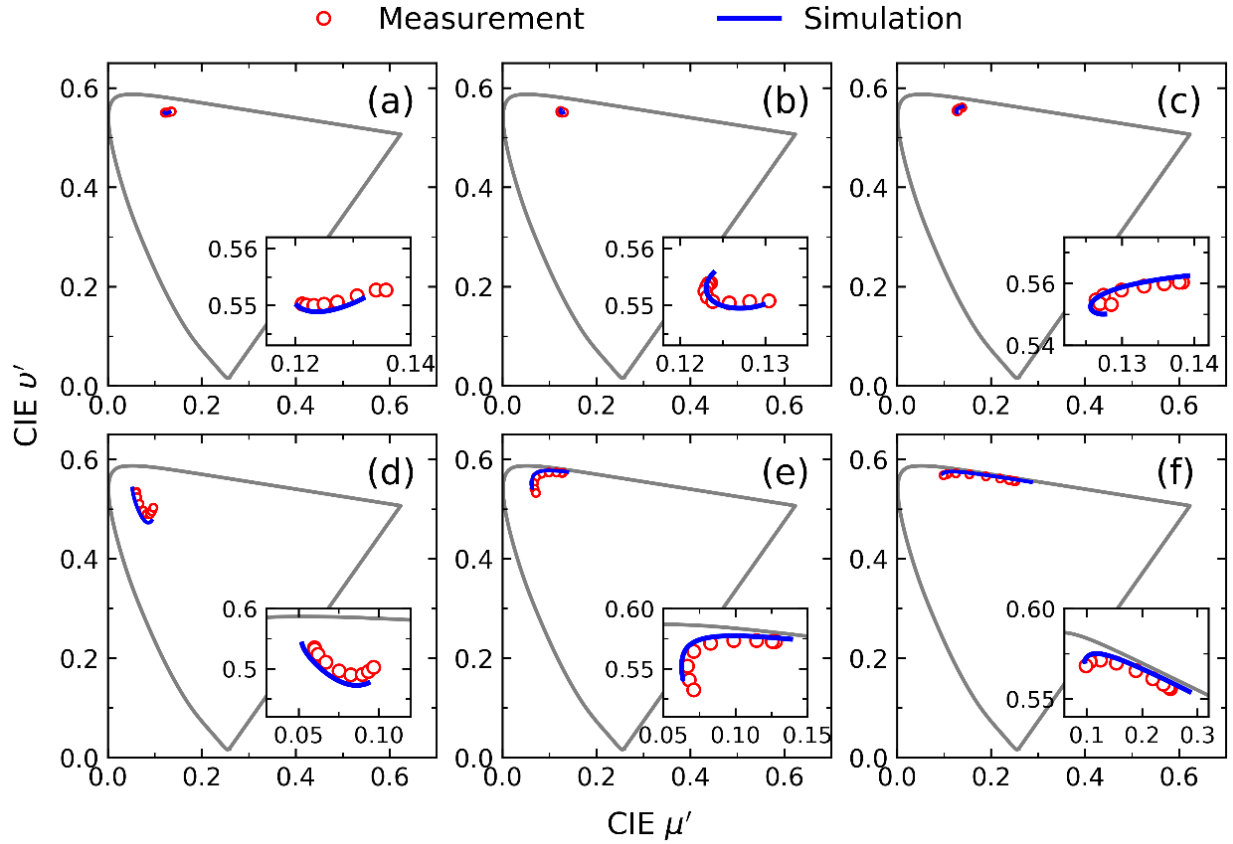


**Figure 3-5 | Measured and simulated color shifts of OLED devices:** a) device 1; b) device 2; c) device 3; d) device 4; e) device 5; and f) device 6.

### 3.4 Systematic optimization

Based on the validated simulation model, we are able to perform systematic optimization for RGB-OLED displays. In the following simulations, the layer structure of the OLED display system is illustrated in Fig. 3-6. It is a typical RGB OLED display system. Each pixel consists of R/G/B three subpixels. The RGB OLED display architecture plotted in Fig. 3-6 has been proven feasible for industrial production [51]. In all three subpixels, we used a bi-layer Ag/ITO as the reflective anode, 4,4',4''-Tris(N-(naphthalen-2-yl)-N-phenyl-amino)triphenylamin (2T-NATA) as the HIL layer [51-52], NPB as the HTL layer, Alq<sub>3</sub> as the ETL layer, and thin Mg:Ag alloy (10:1)

as the semi-transparent cathode [51]. The bis(2-methyl-8-quinolinolato)(para-phenylphenolato) aluminium (III) (BAIq) doped with 10 wt% phosphorescent emitter bis(1-phenylisoquinoline)(acetylanetonate) iridium (III) ( $\text{Ir}(\text{piq})_2(\text{acac})$ ) [51] is adopted as the red emissive layer (Red-EML). The green EML is 8 wt% fac-tris(2-phenylpyridine) iridium ( $\text{Ir}(\text{ppy})_3$ ) doped 4,4'-N,N'-dicarbazole-biphenyl (CBP) [53]. Due to operation lifetime concern, the blue subpixels utilize fluorescent blue emitter 1,4-di-[4-(N, N-diphenyl)amino]styrylbenzene (DSA-Ph), which is doped in host material 2-methyl-9,10-di(2-naphthyl)anthracene (MADN) with 5 wt% concentration [51]. The PL spectra of Red/Green/Blue materials in our simulations are extracted from previous publications [54-56]. The wavelength-dependent refractive indices of the organic layers are either obtained from ellipsometry measurement or extracted from literatures [57-58].

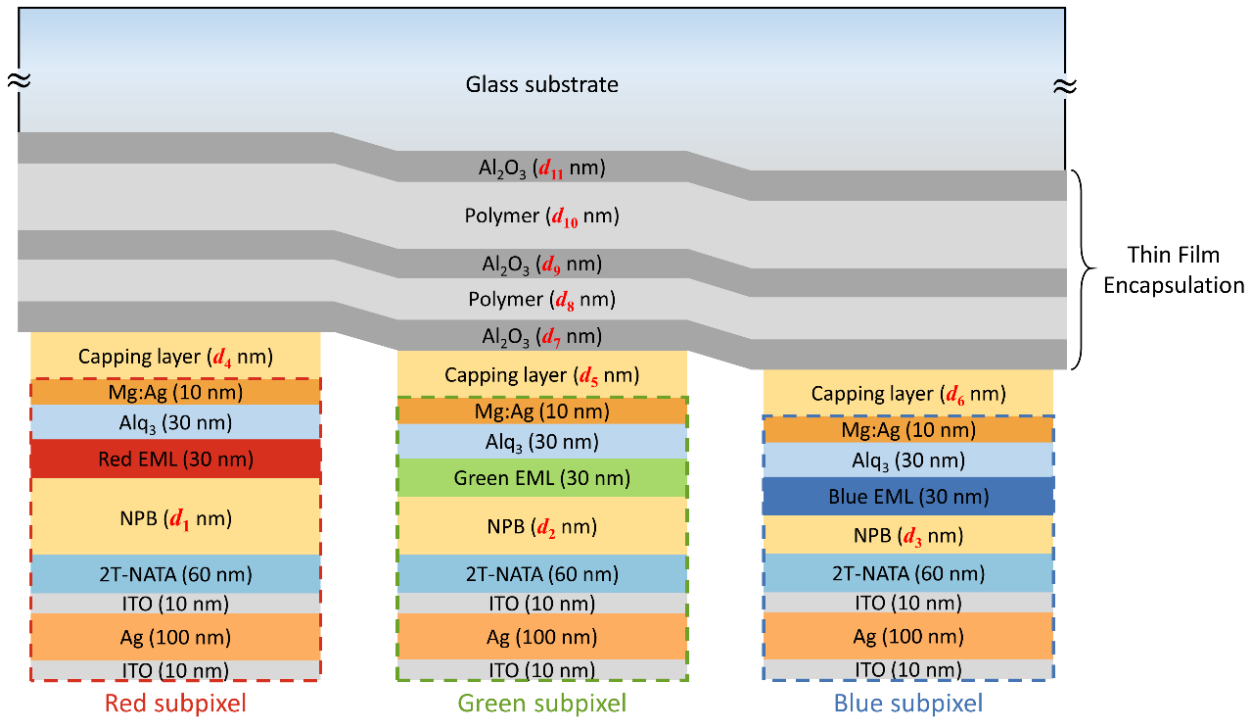


**Figure 3-6 | Layer structures of OLED display with Red, Green and Blue sub-pixels.**

As illustrated in Fig. 3-6, there is a thin dielectric capping layer (CPL) above the semi-transparent cathode. Such a capping layer has been found to significantly enhance the optical efficiency [59-61] of OLED by changing the microcavity effect. Actually, CPL has been widely used in practical OLED display devices. In our simulations, organic material NPB is used as the capping layer. One may also notice that the multilayered thin film encapsulation (TFE) is also included in the system architecture. Since OLED devices are extremely sensitive to moisture and oxygen, reliable encapsulation techniques are essential for commercial applications. The well-known BARIX multilayer technology [62] proposed by Vitex Inc, which involves organic-inorganic alternating stacks, can be very efficient to protect devices from the corrosion of water vapor and oxygen permeation. Recently, the atomic layer deposition (ALD) technique was applied to OLED encapsulation for preparing highly dense and much thinner barrier layer [63-65]. The employment of multilayered TFE would also affect the OLED emission performance [66-67], due to optical interference. Thus, for accurate optical analysis, the TFE multilayer should be taken into consideration as well. As shown in Fig. 3-6, our TFE consists of five  $\text{Al}_2\text{O}_3$ /Polyacrylate alternating layers. The input variable parameters to be optimized are the thicknesses of the HTL, CPL and TFE layers. In total, there are eleven independent variables in our optimization, which can be denoted by  $D = [d_1, d_2, d_3, \dots, d_{11}]$ . The parameter boundary constraints depend on the practical requirements. In particular, the HTL layer thickness is set to be less than 250 nm to avoid electrical property distortion. In order to maintain reliable barrier performance,  $\text{Al}_2\text{O}_3$  layers are kept thicker than 5 nm during optimization.

As mentioned above, three metrics need to be considered to evaluate the RGB OLED display performance. We listed three evaluation metrics as below:

- 1) Optical out-coupling efficiency. As to three subpixels, their optical efficiencies are denoted as  $EQE_R$ ,  $EQE_G$  and  $EQE_B$ , respectively. The first optimization objective can be defined as the arithmetic average, weighted average or minimum value of  $EQE_R$ ,  $EQE_G$  and  $EQE_B$ , according to the specific application needs. In our work, the minimum value  $EQE_{\min} = \min\{EQE_R, EQE_G, EQE_B\}$  is adopted as the first objective, as an example.
- 2) Color gamut coverage (CGC). In the color gamut evaluation, there actually exist several different definitions. We use the color gamut coverage in the normal viewing direction as the second objective, which can be expressed as:

$$CGC = \frac{A_{display} \cap A_{standard}}{A_{standard}}, \quad (6)$$

where  $A_{display}$  stands for RGB triangular area of the display and  $A_{standard}$  is the triangular area of the reference standard. In our simulation, the wide color gamut DCI-P3 with D65 white point is used as the standard, as illustrated in [Fig. 3-7](#).

- 3) Angular color shift. In order to evaluate the color shift throughout the entire color gamut, we have defined 10 reference colors in total. These reference colors include three primary colors, white point D65, and six mixed colors. With DCI-P3 primary colors as an example, 10 reference colors are plotted in CIE1976 color space [[Fig. 3-7](#)]. Since currently most of VR displays can provide FOV around  $100^\circ$  to  $110^\circ$ , we only need to analyze the color shift within  $\pm 60^\circ$  viewing cone. The third optimization objective is defined as the maximum



value of the average color shift  $\Delta\mu'v'_{\max}$  of 10 reference colors from  $0^\circ$  to  $60^\circ$  viewing angle.

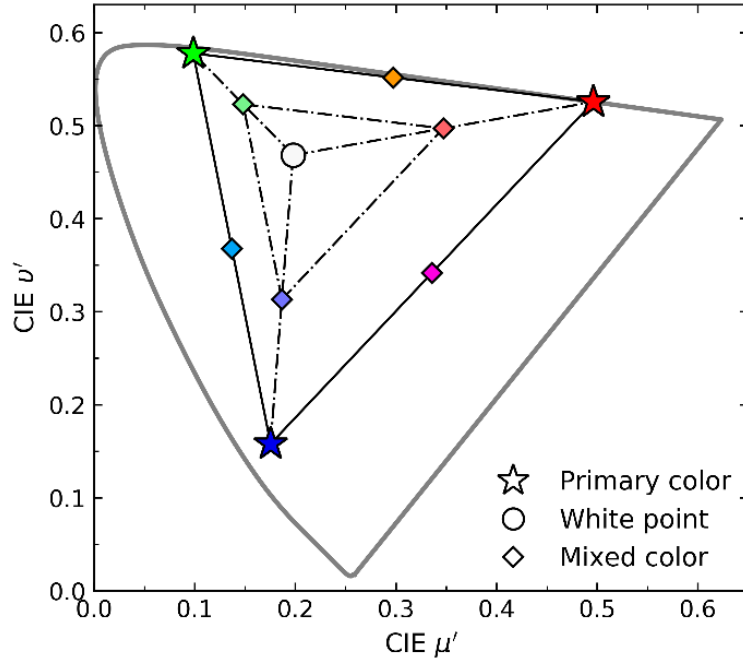


**Figure 3-7 | 10 reference colors in CIE1976 color space.**

### 3.5 Optimization results

The systematic optimization of an RGB OLED display involves 11 input parameters and 3 objectives. Such a multi-parameter and multi-objective optimization would generally consume massive computational resource and long computational time. To speed up the simulation program, multicore parallel computing technique has been adopted. In our workstation with two 14-core Intel Xeon E5-2660 processors, the execution time of one performance evaluation of an RGB OLED display is shorter than 0.25 seconds. Such a fast computation time enables numerous iterations for optimization. To ensure that the global optimal solutions can be determined, four

optimization algorithms, Genetic Algorithm (GA), Adaptive Simulated Annealing (ASA), Particle Swarm Optimization (PSO) and Differential Evolution (DE), have been interchangeably applied during the optimization. As for a multi-objective optimization problem, any further improvement of the solution in terms of one objective is likely to be compromised by the degradation of another objective. Such optimal solutions constitute a *Pareto Front* [68]. In our optimization for the above-mentioned RGB OLED system, more than 1,000,000 iterations have been implemented to give 2,000 optimal solutions. All the optimal solutions visualize the *Pareto Front* of this 3-objective optimization, as illustrated in Fig. 3-8.

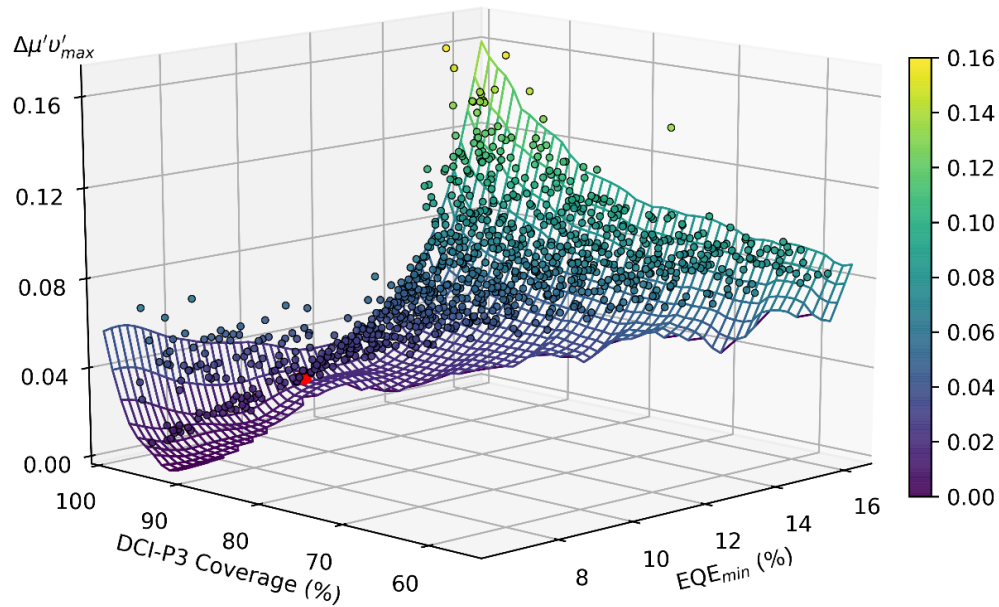


**Figure 3-8 | The *Pareto Front* of the 3-objective systematic optimization.**

Each point on the *Pareto Front* surface in Fig. 3-8 presents an optimal solution. It describes the weakest color shift  $\Delta\mu'v'_{\max}$  we can obtain in theory without sacrificing *EQE* and color gamut. The *Pareto Front* surface geometry reveals the intrinsic trade-offs between optical efficiency, color purity and angular color shift. As the microcavity effect gets stronger, the *EQE* and color

gamut coverage increase, but the angular color shift worsens, as Fig. 3-8 shows. Appropriate optimal solutions can be selected according to different application needs.

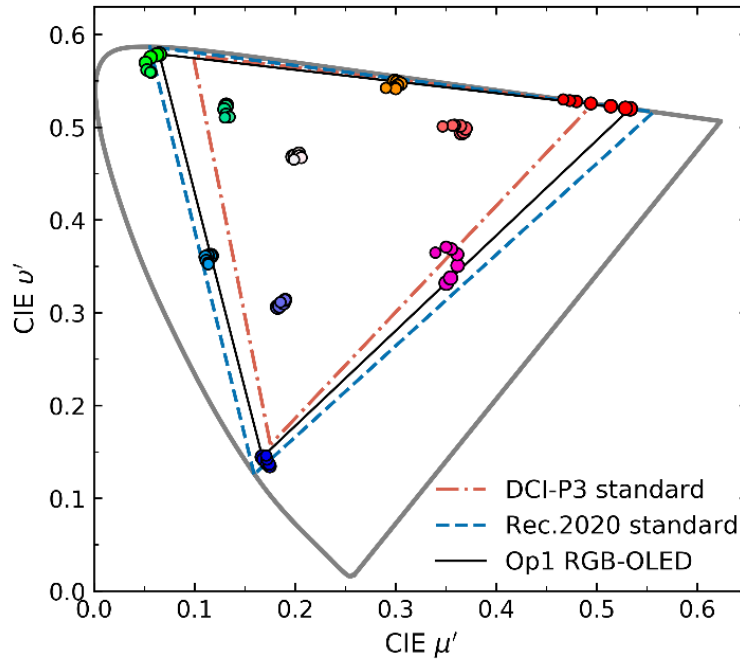


**Figure 3-9 | Color shift of the 10 reference colors from 0° to 60° for Op1 RGB-OLED.**

Here we choose one example: optimal solution 1 (Op1), namely red dot in Fig. 3-8, for detailed analysis. The OLED layer thicknesses for optimal solution 1 are  $D = [184 \text{ nm}, 114 \text{ nm}, 69 \text{ nm}, 39 \text{ nm}, 174 \text{ nm}, 116 \text{ nm}, 56 \text{ nm}, 107 \text{ nm}, 77 \text{ nm}, 126 \text{ nm}, 112 \text{ nm}]$ . As for this system architecture, the optical efficiencies of the RGB OLEDs are  $EQE_R = 11.3\%$ ,  $EQE_G = 17.5\%$ , and  $EQE_B = 13.7\%$ . The average efficiency is  $EQE_{ave} = 14.2\%$ . In comparison with commercialized planar RGB OLED system whose optical efficiency is normally  $\sim 20\%$ , the Op1 system can achieve 71% optical efficiency  $EQE$  of the commercial one. Another significant advantage of top-emitting OLED is its excellent color purity. Thus, we also need to examine the color performance of Op1 OLED display. The color triangle of Op1 is plotted in CIE1976 color space, as shown in Fig. 3-9.

The optimized OLED display Op1 can cover 99.02% of DCI-P3 standard and 88.26% of Rec. 2020 standard. In terms of triangular area ratio, its area can achieve 121.12% of the DCI-P3 triangular area. The optimized OLED device presents an excellent color performance.

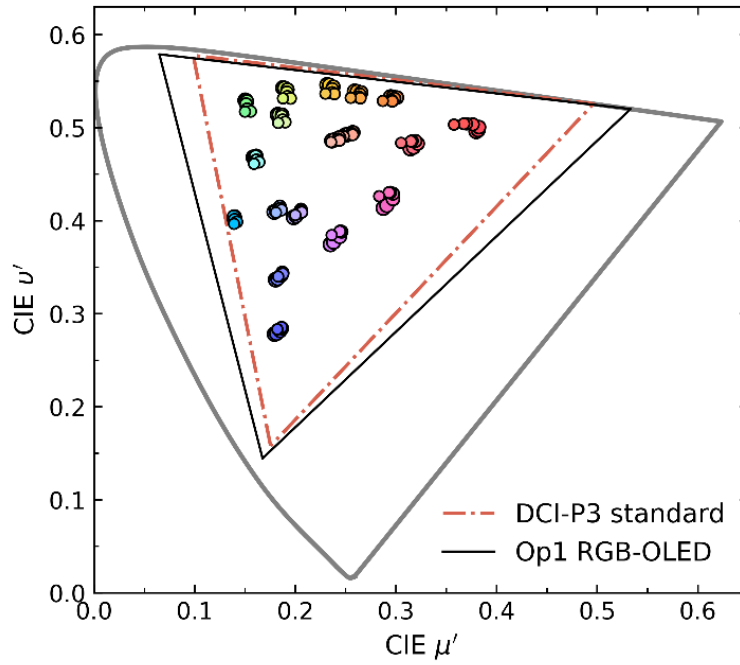


**Figure 3-10 | Color shift of the first 18 colors in Macbeth ColorChecker from 0° to 60° for Op1 RGB-OLED.**

Next, we investigate the angular color shift. Figure 3-9 depicts the CIE coordinates of 10 reference colors at different viewing angles, from 0° to 60° with 10° interval. The average color shift  $\Delta\mu'v'$  at 60° is only 0.019, which is good enough for commercial applications. As Fig. 3-9 indicates, the red channel has the most severe angular color shift. It is harder for red subpixels to get high efficiency, pure colors and weak color shift simultaneously than green and blue subpixels. This is the bottleneck for the RGB OLED display system optimization. One thing noteworthy is that some colors are actually more important than the others in a display system. The Macbeth

ColorChecker [69] is commonly used as the reference in color tests and reproductions. It is designed to mimic the colors of natural objects such as human skin, foliage, and flowers. We also evaluate the color shifts of the first 18 colors from Macbeth ColorChecker based on our Op1 RGB OLED system. The angular color shifts are illustrated in Fig. 3-10. The color shifts of all 18 colors within  $\pm 60^\circ$  viewing cone are kept below 0.02 and the maximum value of average  $\Delta\mu'v'$  from  $0^\circ$  to  $60^\circ$  is only 0.0102, which is visually indistinguishable.

### 3.6 Discussion

In Section 3.5, we have discussed the optimal solutions obtained by multi-objective optimization algorithm. In addition to optimization results, we may still need to examine the relationships between the emission behaviors and the thickness of each layer. In Fig. 3-11, for each of the 2000 optimized configurations, we plot the corresponding thickness of HTL [Figs. 3-11 (a-c)], capping layers [Figs. 3-11(d-f)] and thin film encapsulation layers [Figs. 3-11 (g-l)] with their optical performances. Figure 3-11 clearly illustrates that the HTL layers have higher impact on optical behaviors than other layers. The systematic optimization applies stricter constraint on HTL's thickness. For instance, if a high  $EQE \sim 15\%$  is achieved, the HTL thickness of red OLED needs to be  $200 \pm 5$  nm [Fig. 3-11(a)], while the capping layer can be in the range of  $40 \sim 90$  nm [Fig. 3-11(d)]. Thus, the optical performances are more sensitive to the thickness of HTL layers. Actually, this phenomenon is in accord with our expectation, since the HTL layer is located between two metal electrodes and it can directly affect the cavity length of OLEDs. As for CPL and encapsulation layers, our proposed systematic optimization algorithm has also provided the

optimal thickness ranges for these layers. Within the optimal range, the device performances are not very sensitive to the layer thickness.

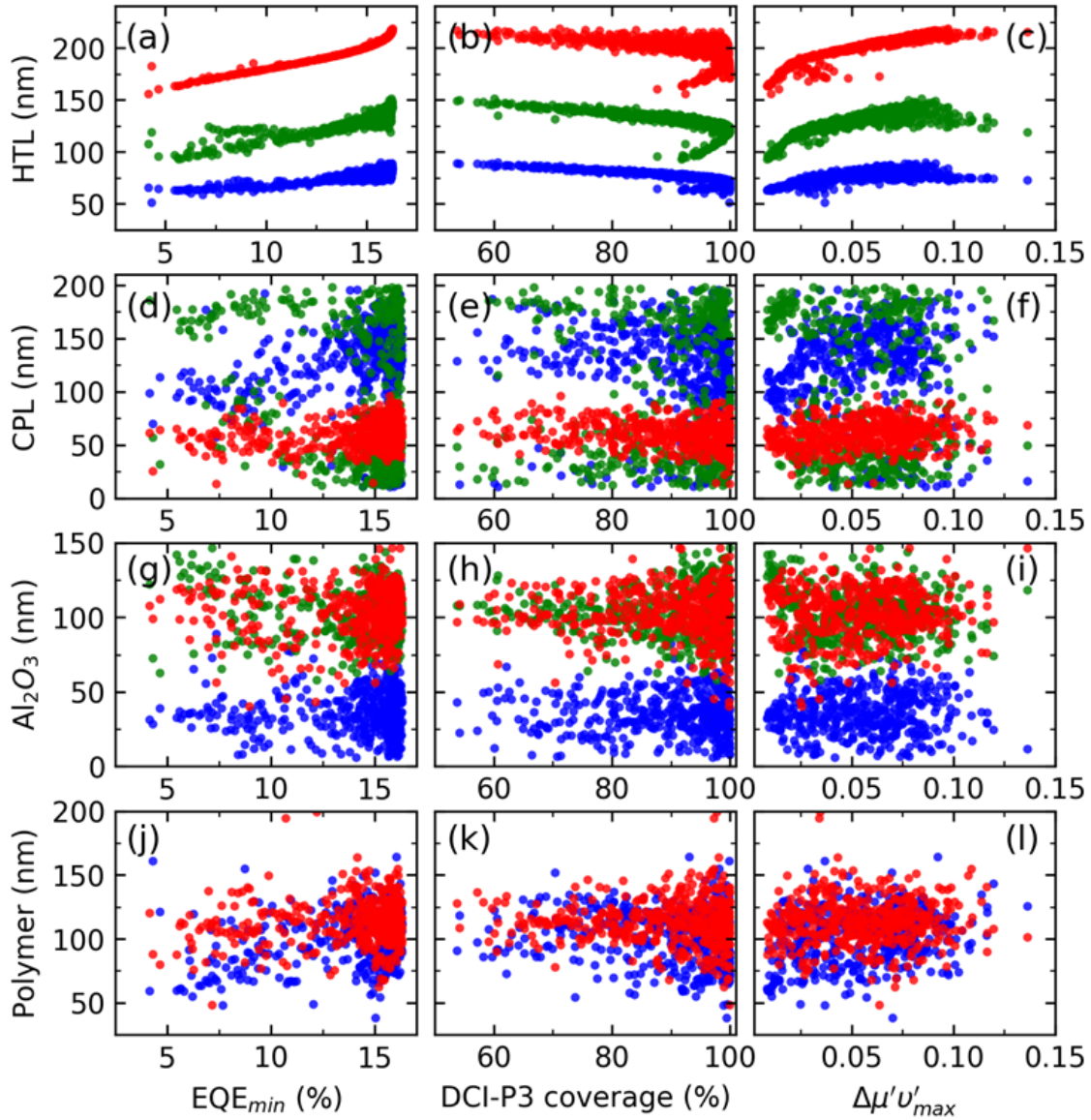


**Figure 3-11 | The correlations between the OLED optical behaviors and the layers' thickness:** (a)(b)(c) HTL layers (red- $d_1$ , green- $d_2$ , blue- $d_3$ ); (d)(e)(f) CPL layers (red- $d_4$ , green- $d_5$ , blue- $d_6$ ); (g)(h)(i)  $\text{Al}_2\text{O}_3$  layers in thin film encapsulation (blue- $d_7$ , green- $d_9$ , red- $d_{11}$ ); (j)(k)(l) polymer layers in thin film encapsulation (blue- $d_8$ , red- $d_{10}$ ).

### 3.7 Summary

In this chapter, we mainly discussed about the system optimization on RGB-OLED display system. OLED is another potential display technology to achieve HDR display. Different from LCD, the limitation of OLED display comes from bright state, specifically inadequate peak brightness. Strong microcavity is one efficient approach to enhance optical efficiency, while its major trade-off is severe angular color shift. How to enhance optical efficiency while keeping low angular color shift remains a challenge to be resolved.

In Sections 3.1 and 3.2, we analyzed the two reasons of angular color shifts of RGB OLED displays: resonance wavelength shift and mismatched subpixel angular distributions. In Section 3.3, we experimentally validate our simulation model for both strong and weak cavity OLEDs. Our simulation model has been proven to be a validate and efficient tool to evaluate angular color shifts. By utilizing four global optimization algorithms, we proposed a systematic method to optimize EQE, color gamut coverage, and angular color shift simultaneously, in Section 3.4. The obtained optimization *Pareto Front* not only reveals the intrinsic trade-offs between efficiency, color gamut, and color shift, but also provides valuable guidelines for improving the RGB OLED display system. Lastly, in Section 3.6, we also carried out detailed analysis on optimization constraints and found that the HTL layers play more important roles than other layers.

## CHAPTER 4: FOVEATED NEAR-EYE DISPLAY

### 4.1 Background

The visual acuity for normal 20/20 vision could achieve  $\sim 1$  arcmin [17], which sets a clear target for display resolution. However, current VR headsets can only deliver angular resolution around 10~15 ppd. It is easy to find that at least  $4\sim 5\times$  improvement on angular resolution is necessary. As Fig. 4-1 illustrates, there exists a trade-off between high angular resolution and wide field of view. In order to achieve angular resolution  $\sim 60$  ppd and  $FOV > 100^\circ$  at the same time, a display panel with over  $6K \times 6K$  of pixels would be needed for each eye. Currently, most of VR headsets are using 1K to 2K resolution panels. Such a huge increase of pixel number would bring several new challenges and difficulties:

- 1) Panel fabrication. No matter for LCD or OLED display, integrating over 36 million ( $6K \times 6K$ ) pixels on a small size panel (usually  $< 5$  inch) is definitely not an easy task. With the tremendous efforts of panel manufactures, the VR display resolution has been pushed to around  $4K \times 4K$  recently [70], although there is still a long way to go for low cost mass production.
- 2) Driving electronics. To drive a high-resolution  $6K \times 6K$  display panel with over 90Hz refresh rate, the addressing time would be much shorter for each scan line [71]. New driving circuitry designs are needed to handle such a high resolution.
- 3) Data transport. Assuming a 90Hz  $6K \times 6K$  display panel, we need to deliver more than 70 Gbit/s to the display panel, not even to mention light field displays with space-, time- or polarization-multiplexing [72].



- 4) Image rendering. It would be extremely challenging to render high-resolution images and videos in real-time, due to the limitation from the computing power. More efficient image rendering pipeline must be developed as well [73].

So far, achieving retina-level resolution near-eye display with wide FOV remains a very challenging task. To overcome these issues, several efforts [74-76] have been devoted to improve the effective resolution by optical methods. For example, using an electrical driven image deflector to increase effective pixel number has been proposed in [75-76]. By doing so, the effective angular resolution can be doubled, while the refresh rate also needs to be doubled.

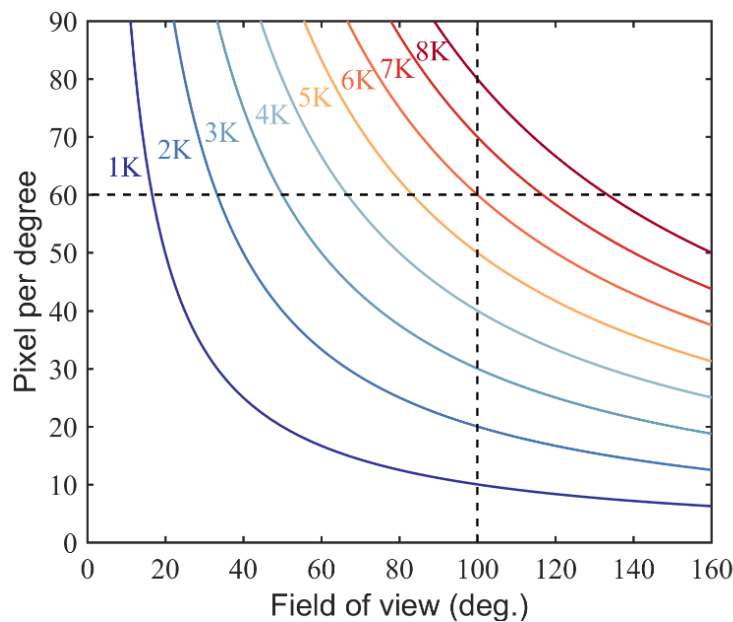


**Figure 4-1 | The trade-off between angular resolution and field of view in near-eye displays.**

As discussed above, simply increasing the pixel number does not seem to be an elegant solution at current stage. Human visual system should be taken into consideration as well. Actually, our visual system has an efficient information processing architecture. In human retina, the image-capture receptors, namely cone cells, are concentrated in a very narrow central region, called fovea

[77]. Therefore, human eye acuity is the highest in the fovea region ( $\sim\pm 5^\circ$ ) and drops rapidly as the eccentricity angle increases, as shown in Fig. 4-2. The image acquired by human eye has much higher information content in the fovea region. Such a foveation concept has already been utilized in the imaging system and video processing [78-79]. As to VR displays, we only need to provide high resolution for the central fovea instead of the whole field of view. Therefore, a multi-resolution display system [Fig. 4-2] seems to be an efficient solution by considering panel fabrication difficulties and data transport issue. Several multi-resolution foveated display designs have been proposed [80-81], but these designs are still relatively bulky and difficult to integrate into a compact wearable device. Moreover, a practical foveated display should be able to displace high resolution region to enable gaze-contingent technique.

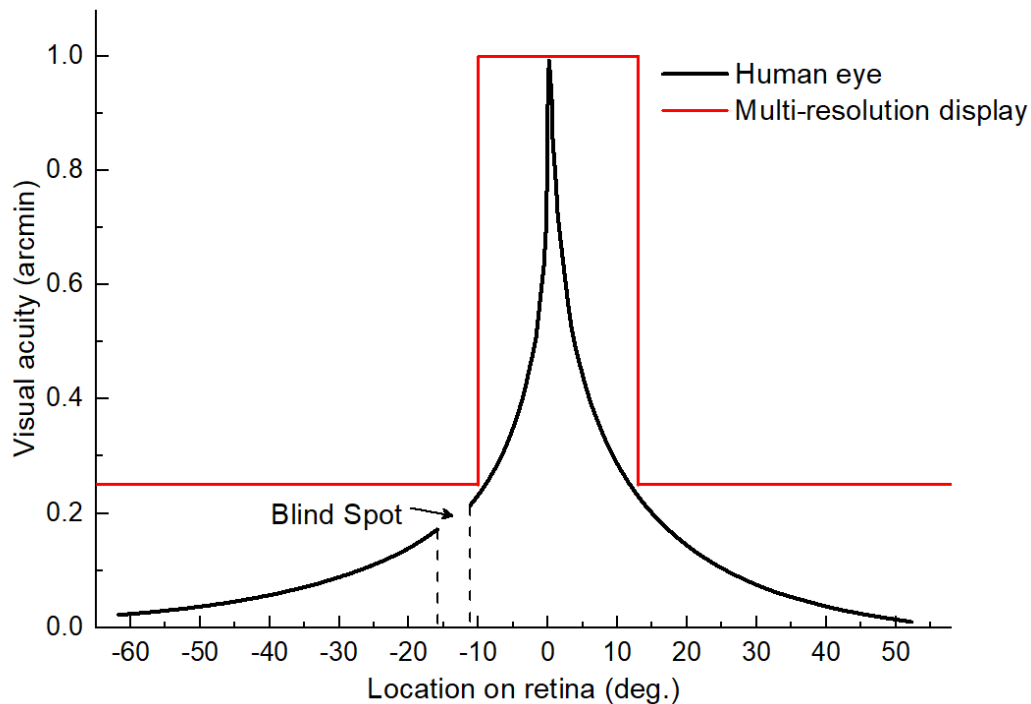


**Figure 4-2 | Illustration of human visual acuity and multi-resolution display.**

## 4.2 System configuration

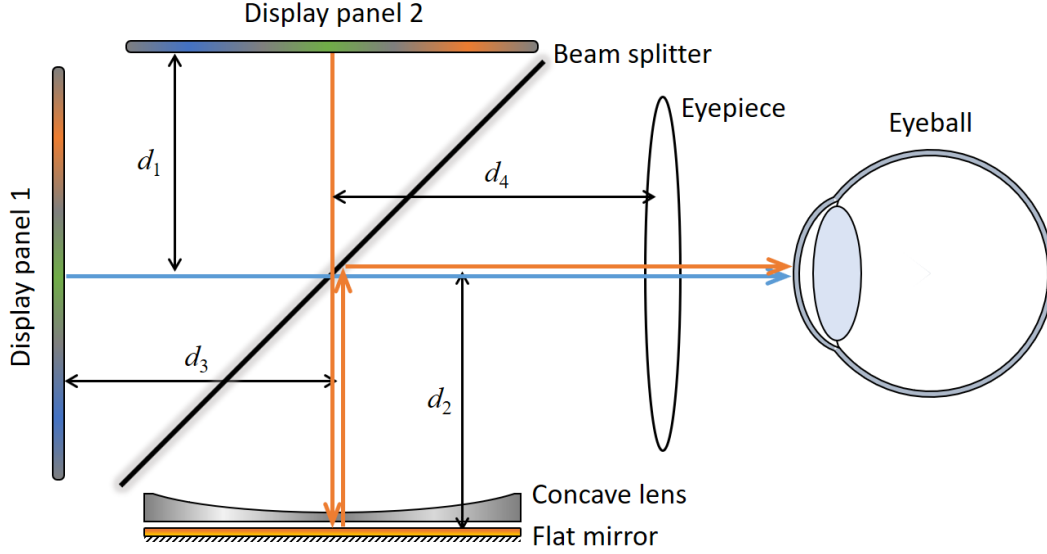


**Figure 4-3 | Schematic diagram of the proposed multi-resolution foveated display.**

Figure 4-3 depicts the system configuration of our proposed multi-resolution display design. Briefly, this design consists of two display panels with a beam splitter (BS) as an optical combiner. The unfolded optics of the proposed design are illustrated in Figs. 4-3(a) and (b). The image displayed by panel 1 will be directly viewed by human eye through beam splitter and eyepiece lens as plotted in Fig. 4-4(a), which is very similar to a conventional VR display. However, in our design this display panel only delivers the image content for peripheral region. The light emitted from the second panel will pass through a folded optical path, which includes a concave lens and a flat mirror, as Fig. 4-4 depicts. Thus, the image displayed by panel 2 will be minified first by the concave lens [Fig. 4-4(b)], before it is perceived by human eye. If the focal length of concave lens is denoted as  $-f_c$  and the optical minification as  $M$ , then the spatial resolution enhancement ratio  $R$  can be expressed by:

$$R = \frac{1}{M} = 1 + \frac{d_1 + d_2}{f_c/2}, \quad (7)$$

where  $d_1+d_2$  stands for the distance from display panel 2 to the flat mirror. According to Eq. (7), the enhancement ratio  $R$  can be enlarged by reducing the focal length of concave lens or increasing the distance  $d_1+d_2$ . Actually, in our following experimental demonstrations, the resolution enhancement can easily reach 4~5 $\times$ . The display 2 can finally generate an ultra-high resolution but small-size image. As mentioned above, two displays provide image contents for fovea and peripheral regions, respectively. A beam splitter is used to combine these two displayed images together, as shown in Fig. 4-3. It is worth mentioning that the perceived image depths from two displays must be matched, as Fig. 4-4(b) plots. Thus, the display panel 2 should be placed at:

$$d_3 = d_2 + \frac{d_1 + d_2}{R}, \quad (8)$$

where  $R$  is the enhancement ratio from Eq. (7). Then display panel 1 and the virtual image of panel 2 can be located at the same depth [Figs. 4-4(a) and (b)].

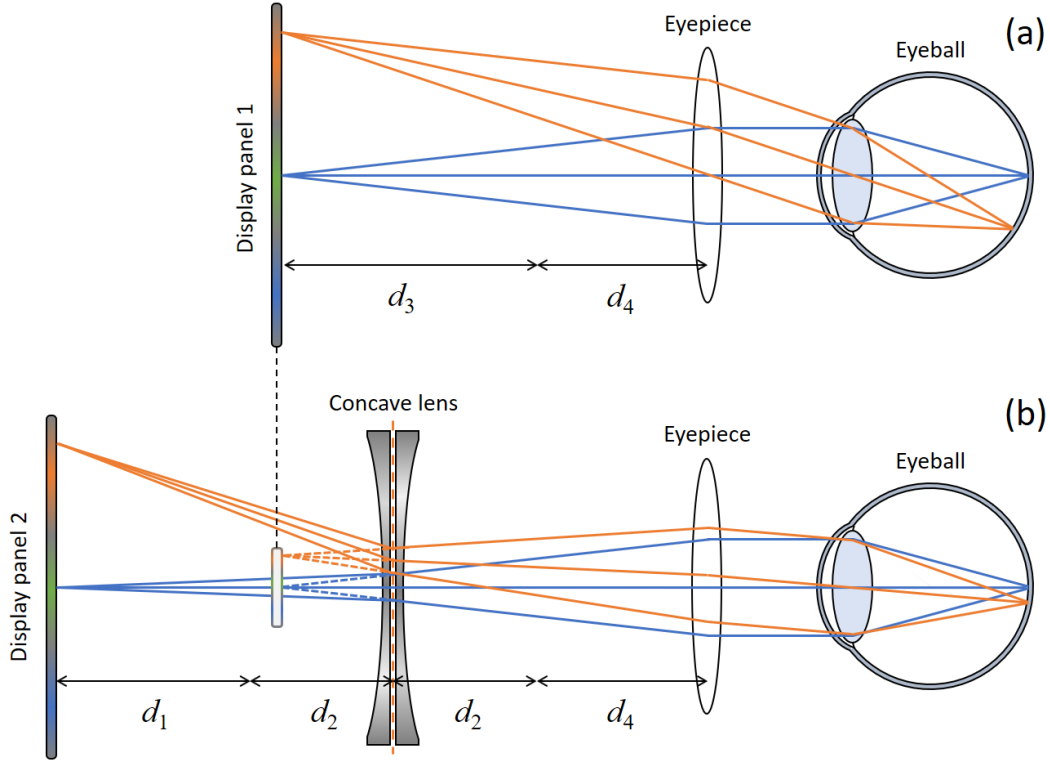


**Figure 4-4 | The unfolded layout of the optical paths: a) display panel 1 and b) panel 2.**

### 4.3 Experimental prototyping

In this section, we carried out experiments to demonstrate our proposed design discussed in Section 4.2. Our optical setup basically followed the layout plotted in Fig. 4-3. In our experiments, two identical 3.7-inch OLED panels with resolution 1200×1080 were employed as the two displays plotted in Fig. 4-3. One plano-concave lens with focus length  $-f_c = -35$  mm was adopted. As for the eyepiece, we used a positive achromatic doublet lens with focal length  $f_e = 10$  cm in our experiments. The main reason why the achromatic lens with  $f_e = 10$  cm is chosen in our experimental setup is to get photography of whole field of view with clear RGB pixels. Actually, the proposed foveated approach can be easily integrated with the current VR design. For instance,

the VR headset eyepieces, like refractive, Fresnel, or hybrid lenses, can also be used in our design. The angular resolution enhancement ratio will keep the same. A camera was placed after the eyepiece lens to capture the displayed images. To eliminate the ghost images generated by panel reflection, we laminated a circular polarizer and an anti-reflection film onto each OLED panel.

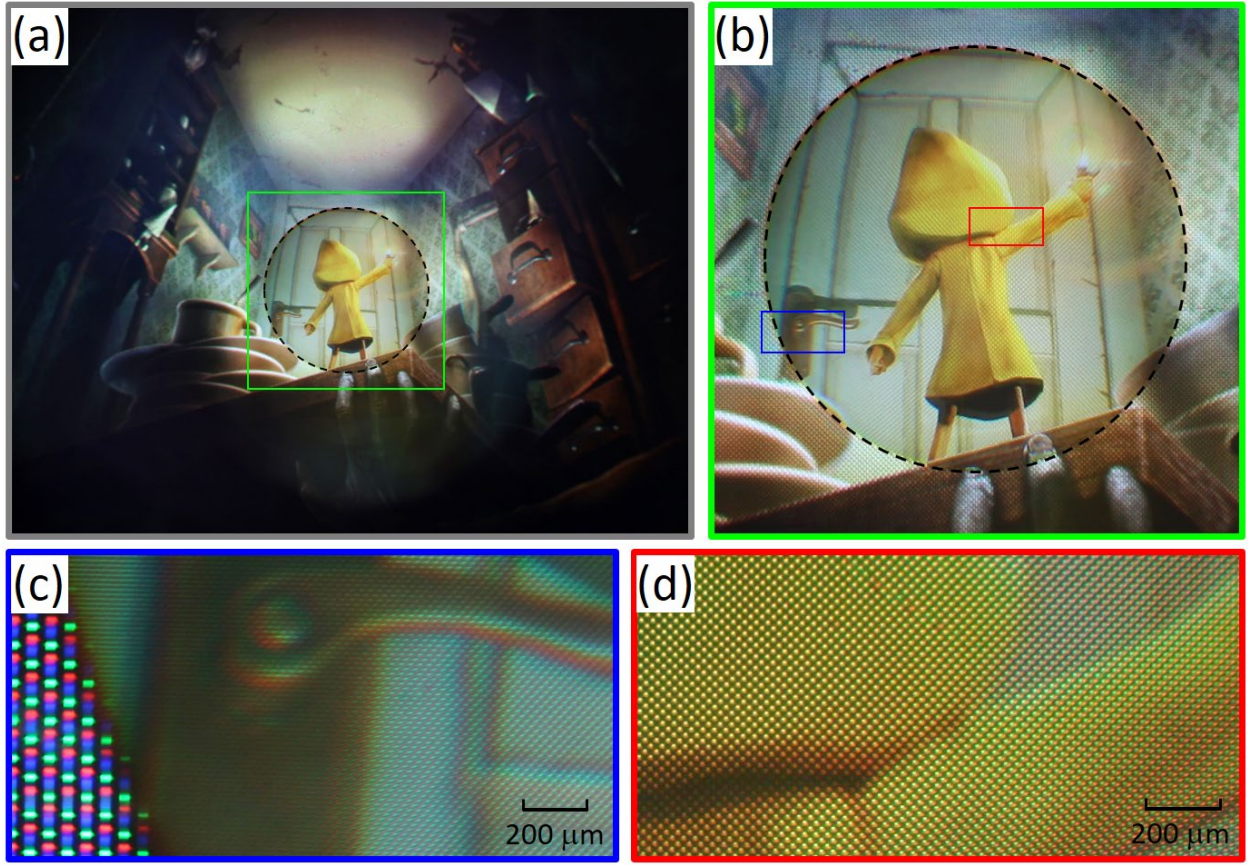


**Figure 4-5 | The experimental photographs of the proposed multi-resolution foveated display with 4× resolution enhancement:** a) displayed image; b) the magnified green square region in (a); c) the magnified blue rectangle region in (b); d) the magnified red rectangle region in (b).

We built up two prototypes with spatial resolution enhancement ratio  $R = 4$  and  $5$ , respectively. According to [Eq. \(7\)](#), we set  $d_1 + d_2 \approx 5.25$  cm to achieve around 4× resolution



enhancement and  $d_1+d_2 \approx 7$  cm for  $5\times$  resolution enhancement. For each case, the distance  $d_3$  was adjusted to match the image depths of two displays, as Eq. (8) suggests.

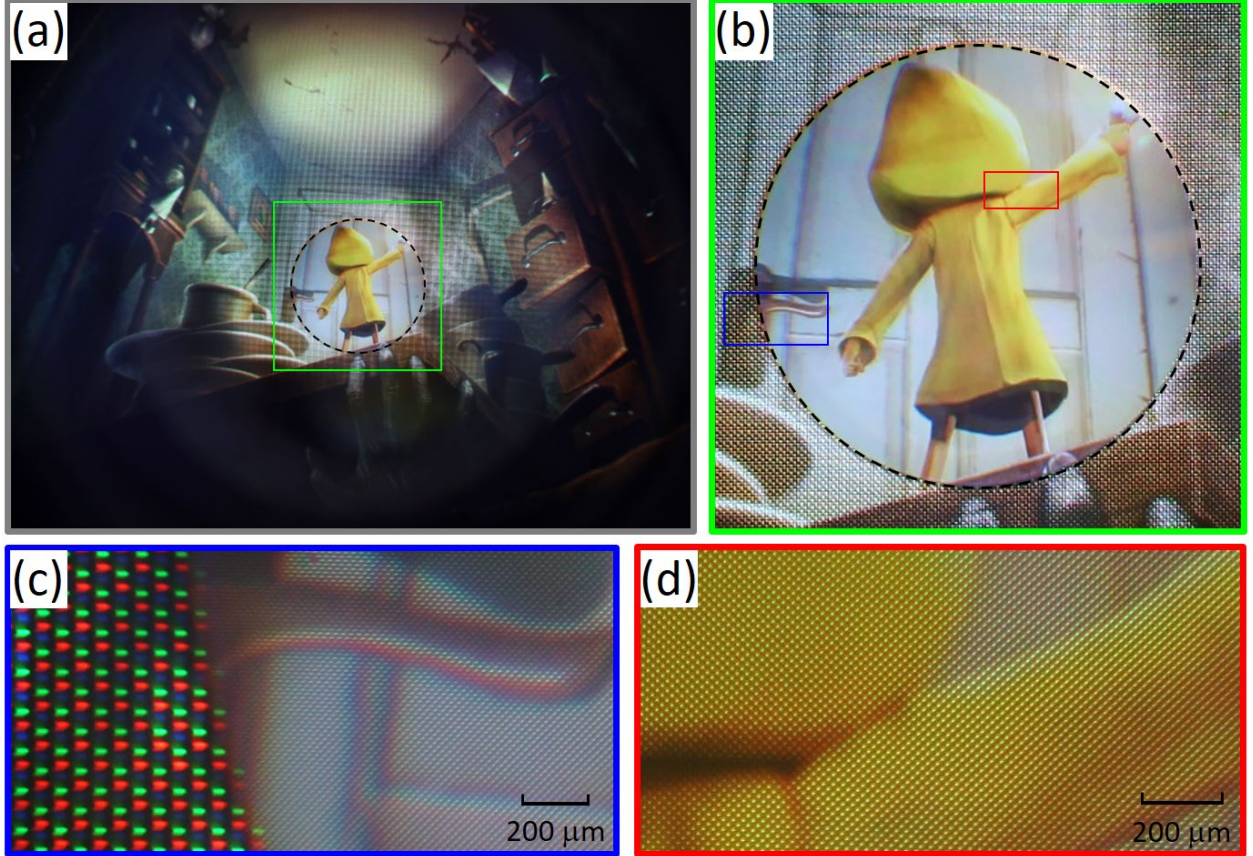


**Figure 4-6 | The experimental photographs of the proposed multi-resolution foveated display with  $5\times$  resolution enhancement:** a) displayed image; b) the magnified green square region in (a); c) the magnified blue rectangle region in (b); d) the magnified red rectangle region in (b).

Figures 4-5 and 4-6 present the experimental photographs taken from our two prototypes. The displayed image quality is very good without obvious image distortions. To further minimize the image distortions in future work, the minifying optical path can be improved with multiple lens or freeform lens. As indicated in Figs. 4-5(a) and 4-6(a), the displayed image regions enclosed by the black circle have much higher spatial resolution than the outside regions. Especially, from the

magnified figures Figs. 4-5(b) and 4-6(b), the clear pixelation or screen-door effect can be observed in the outside low-resolution region. But inside the black circle, images are quite smooth. If we further zoom in the images at the boundary, the pixel size can be compared directly, as depicted in Figs. 4-5(c) and 4-6(c). We also quantitatively evaluated the pixel size through the photographs in our experiments. We first measured the pixel pitch of the OLED panels under an optical microscope, before setting up the foveated display system. Therefore, we are able to measure the pixel pitch in the central and surrounding regions. Then through the photographs, the spatial resolution enhancement ratios can be determined:  $R \approx 4$  for Fig. 4-5 and  $R \approx 5$  for Fig. 4-6. Thus, Fig. 4-5 and Fig. 4-6 indicate that we have successfully demonstrated a multi-resolution foveated display using our proposed optical method.

Figures 4-5 and 4-6 also illustrate that the spatial resolution enhancement of the central region can be easily tuned by changing  $d_1+d_2$ . Higher resolution is achievable, while the trade-off is the shrunk high-resolution region. By comparing Figs. 4-5(a) and 4-6(a), we can clearly see this point. For a commercially available VR display with 1600×1440 resolution and 110° horizontal FOV (HTC Vive pro, 2018), it provides angular resolution of around 14.5 ppd. If we apply our 4× enhancement system, we can obtain ~58 ppd for the central 25° FOV region.

In Fig. 4-7, we further examined the on-axis modulation transfer function (MTF) [82] along two optical paths. The MTF was measured with a Canon EOS T5i camera at F/5.6 with ISO 400 and exposure time 2.5 ms. The MTF of the low-resolution path (Original) drops to 0.5 at 20 cycles per degree (cpd), while the high-resolution path (4×) drops to 0.5 at 72 cpd. The MTF is not exactly 4× as high-resolution path involves an extra fast lens, which introduces additional aberration. As



the system is operating at 14.5 and 58 ppd for low- and high-resolution images, the imaging performance is reasonably sufficient.

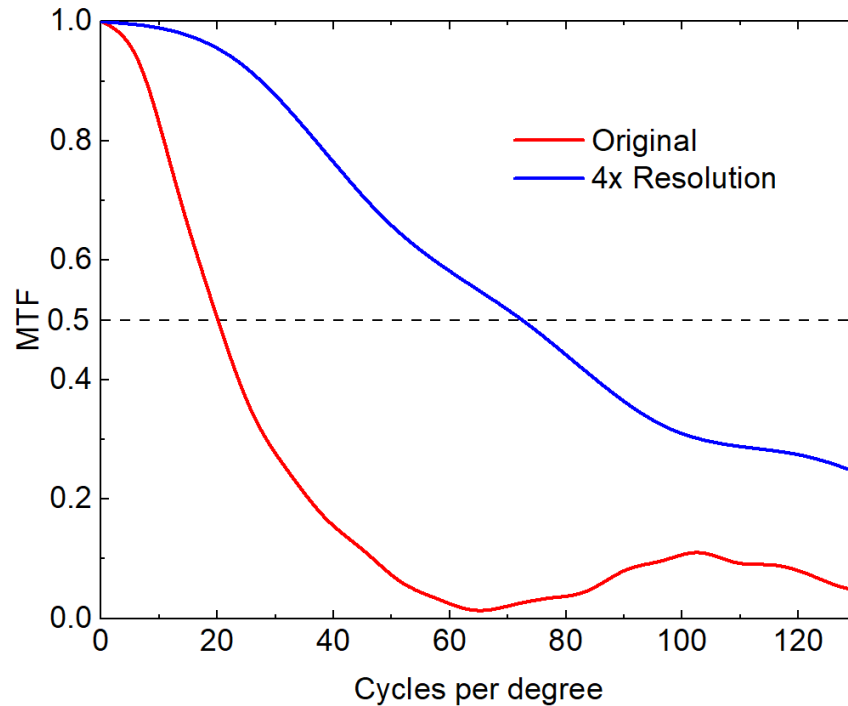


**Figure 4-7 | The measured on-axis MTF for original and 4× resolution in angular space.** Note that the MTF drops to 0.5 at 20 cpd and 72 cpd for the original and 4× resolution, respectively.

#### 4.4 Image shifter

As discussed above, ultra-high angular resolution can be obtained in the narrow central region  $\sim 20^\circ$  FOV. However, this region may still not be large enough, since human eye may look at different positions of the display. Eye-gaze tracking techniques need be integrated to provide better viewing experience. The displayed image content needs to be updated with actively shifting the high-resolution region, by following the eye's viewing direction. To enable eye-tracking function, we propose to use a switchable Pancharatnam-Berry phase deflector (PBD) to shift the high-resolution region and adjust the display contents in real time.

The PBD is a single-order phase grating based on Pancharatnam-Berry phase [83-84]; in theory its diffraction efficiency can achieve up to 100% [75, 85-86]. In a PB phase optical element, the half-wave ( $\lambda/2$ ) plate is spatially patterned with varying in-plane crystal axis direction [85]. Interestingly, its phase modulation is directly determined by the optical axis orientation, namely liquid crystal azimuthal angle  $\varphi(x, y)$ . The detailed working mechanism can be explained by Jones matrices. As for a circularly polarized incident light, the Jones calculus can be written as: [75]

$$J'_{\pm} = R(-\varphi) \cdot W(\pi) \cdot R(\varphi) \cdot \frac{1}{\sqrt{2}} \begin{bmatrix} 1 \\ \pm i \end{bmatrix} = e^{\pm i2\varphi} \frac{1}{\sqrt{2}} \begin{bmatrix} 1 \\ \mp i \end{bmatrix}, \quad (9)$$

where  $J_+$  and  $J_-$  stand for the left- and right-handed circularly polarized light (LCP and RCP), respectively,  $R(\varphi)$  and  $R(-\varphi)$  present the rotation operation matrix and  $W(\pi)$  is the phase retardation matrix. According to Eq. (9), besides flipping the handedness, the  $\lambda/2$  plate also introduces a  $\pm 2\varphi(x, y)$  phase delay. If the LC orientation follows a linear profile [Fig. 4-8(a)] as:

$$\varphi(x, y) = \frac{2\pi}{P} \cdot x, \quad (10)$$

then a linear wavefront delay is constructed, as plotted in Fig. 4-8(b).

Then PBD can work as a high-efficiency single-order phase grating, with deflection angle:

$$\theta = \arcsin\left(\frac{2\lambda}{P}\right). \quad (11)$$

More detailed theoretical explanations can be found in Ref. [75, 85-87]. Both active driving and passive driving schemes can be adopted for driving a PBD [75]. Here we choose the active driving method because PBD will not change the incident light direction at the voltage-on state [Fig. 4-8(c)].

There are three major reasons why we choose a PBD as the image shifter. Firstly, it is a single-order deflector with nearly 100% diffraction efficiency, which helps eliminate ghost images. In experiments, over 95% optical efficiency can be easily achieved [85-87]. Secondly, fast switching between deflection and non-deflection states can greatly reduce the latency for eye-tracking. Both turn-on time and turn-off time of PBD keep shorter than 1 ms [75, 85]. The third reason is low operation voltage, typically 7~8 Volts, which means low power consumption.

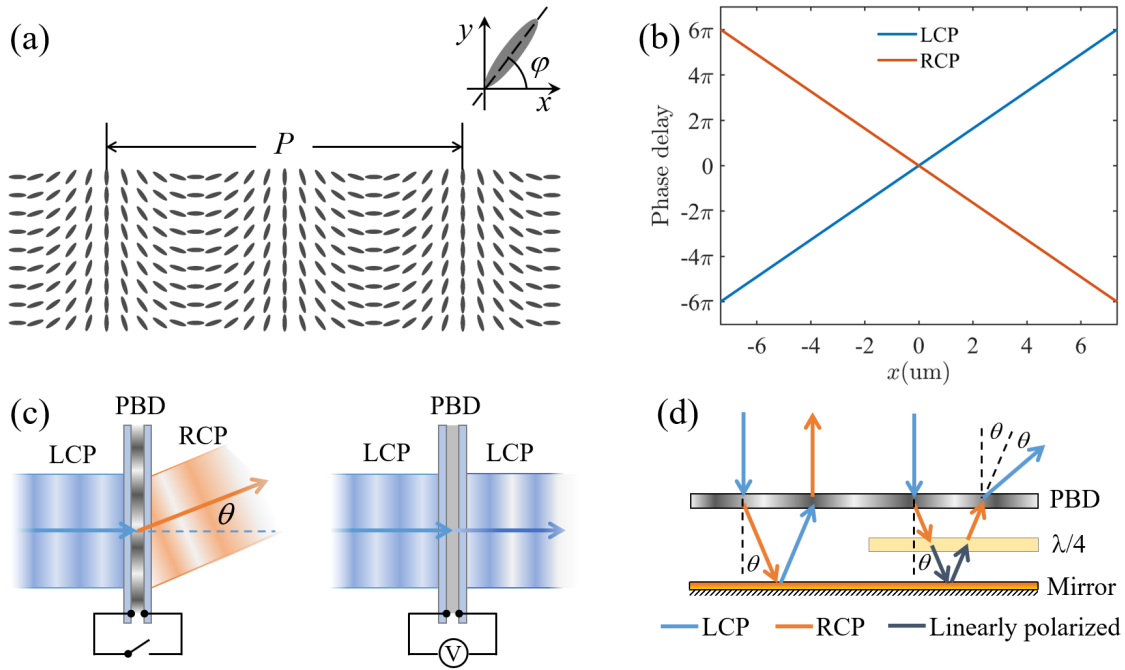


**Figure 4-8 | Working principle of PBD image shifter.** (a) Top view of the LC director distribution in PBD. (b) Phase delay profile of a PBD with  $15^\circ$  deflect angle at  $\lambda = 633$  nm for LCP and RCP, respectively. (c) Active driving to result in a switching between deflection and non-deflection states. (d) The polarization state change for the LCP wave deflected by PBD and reflected by mirror.

It is worth mentioning that polarization management needs to be carefully considered for PB optical elements. As illustrated in Fig. 4-8(d), if a PBD is just simply inserted between the concave lens and the mirror, it works as a simple reflector instead of a deflector because both PBD

and metal reflection will reverse the polarization handedness. Therefore, we need to add another quarter-wave ( $\lambda/4$ ) plate to get the correct polarization state. Finally, the deflection angle of the system combining PBD,  $\lambda/4$  plate, and mirror is  $2\theta$ . Another possible solution is to apply a reflective-type PBD as the image shifter [88].

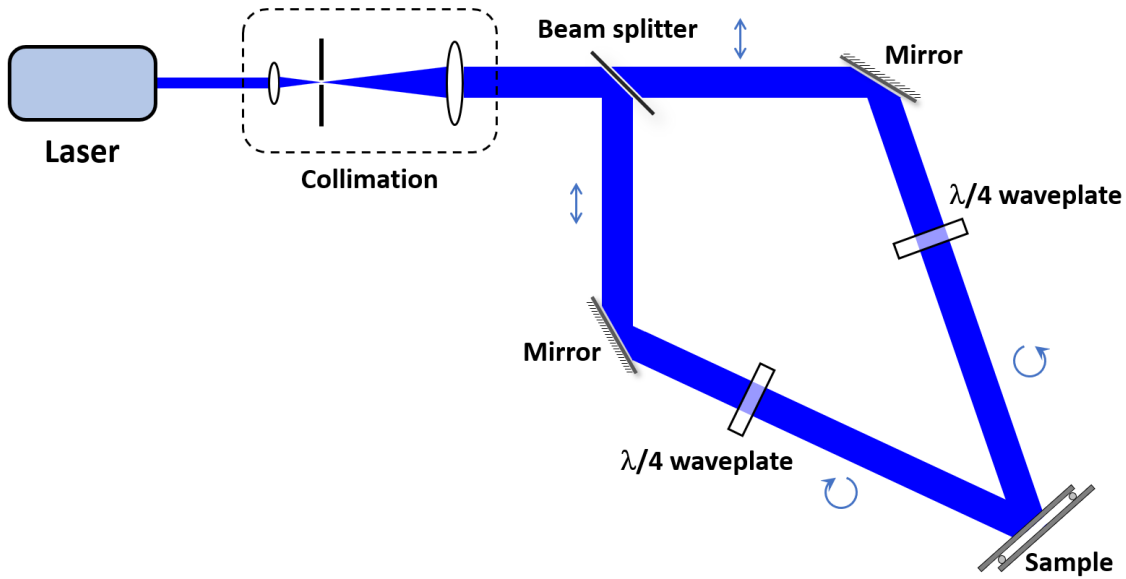


**Figure 4-9 | Optical setup of polarization interference exposure used in PBD fabrication.**

The fabrication process of PB elements normally enrolls polarization interference exposure [89]. Two indium-tin-oxide (ITO) glass substrates were first cleaned and spin-coated with a thin photoalignment layer. Then an empty liquid crystal cell was assembled using two ITO substrates. We set up a Mach-Zehnder interferometer with  $\lambda=442$  nm (He-Cd laser) for interference exposure, whose two arms had opposite circular polarizations, as plotted in Fig. 4-9. After interference exposure, a LC mixture was filling into the above-mentioned empty cell. In our experiment, the spatial period of the fabricated PBD is  $P = 4.88 \mu\text{m}$ , and its deflection angle is  $15^\circ$  for  $\lambda = 633$  nm.

The LC birefringence and thickness were carefully tuned to match the half-wave requirement for  $\lambda=639$  nm. Detailed fabrication procedure of PB elements can be found in [75, 85-89].

To demonstrate this concept by experiments, we inserted the fabricated PBD and a broadband quarter-wave plate between concave lens and flat mirror, as plotted in Fig. 4-10. The above-mentioned OLED panel was still used as display 1. To minimize the possible image blur induced by angular dispersion of diffraction grating, we adopted a 5.5-inch 2560×1440 LCD panel with laser backlight as display panel 2. The three RGB laser wavelengths are  $\lambda_B = 445$  nm,  $\lambda_G = 520$  nm and  $\lambda_R = 639$  nm. A broadband  $\lambda/4$  plate was also laminated to the LCD panel in order to convert its polarization state to circular polarization.

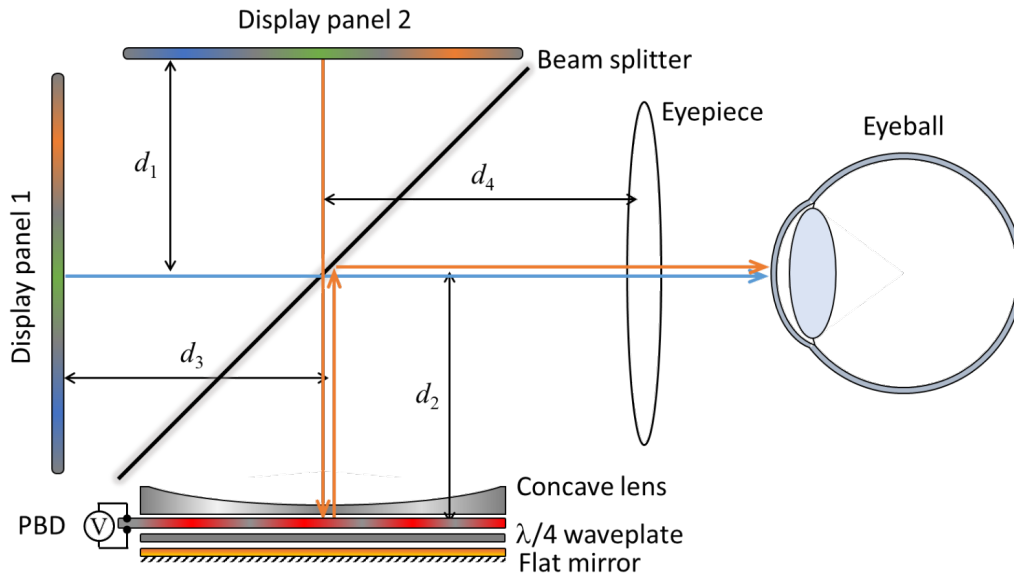


**Figure 4-10 | Schematic diagram of the multi-resolution display with PBD image shifter.**

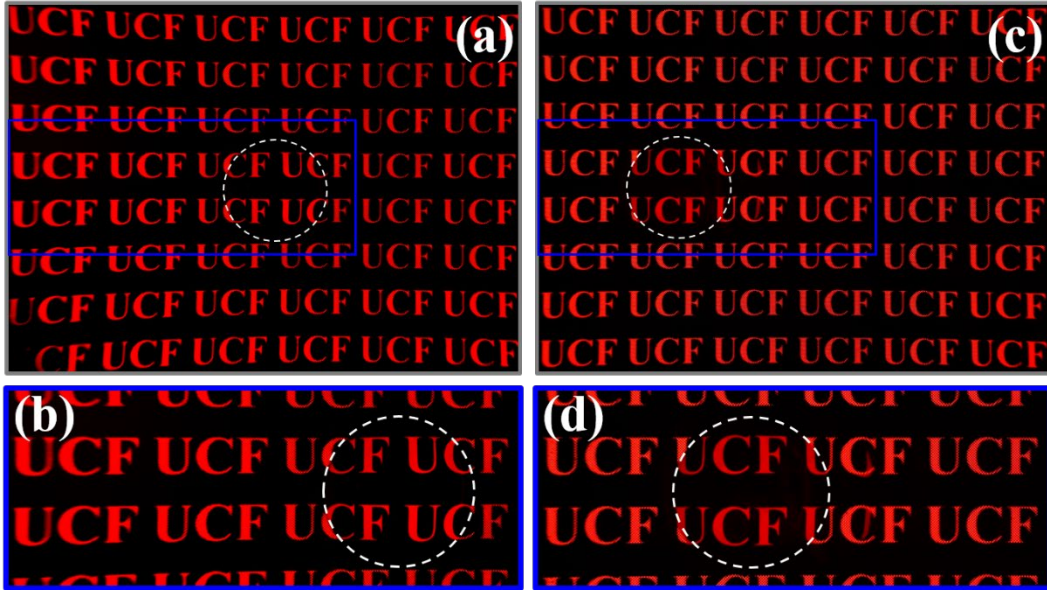


**Figure 4-11 | Multi-resolution display (text) with PBD as image shifter:** a) high-resolution region in the center; b) magnified blue rectangle region in (a); c) shifted high-resolution region; d) magnified blue rectangle region in (c).

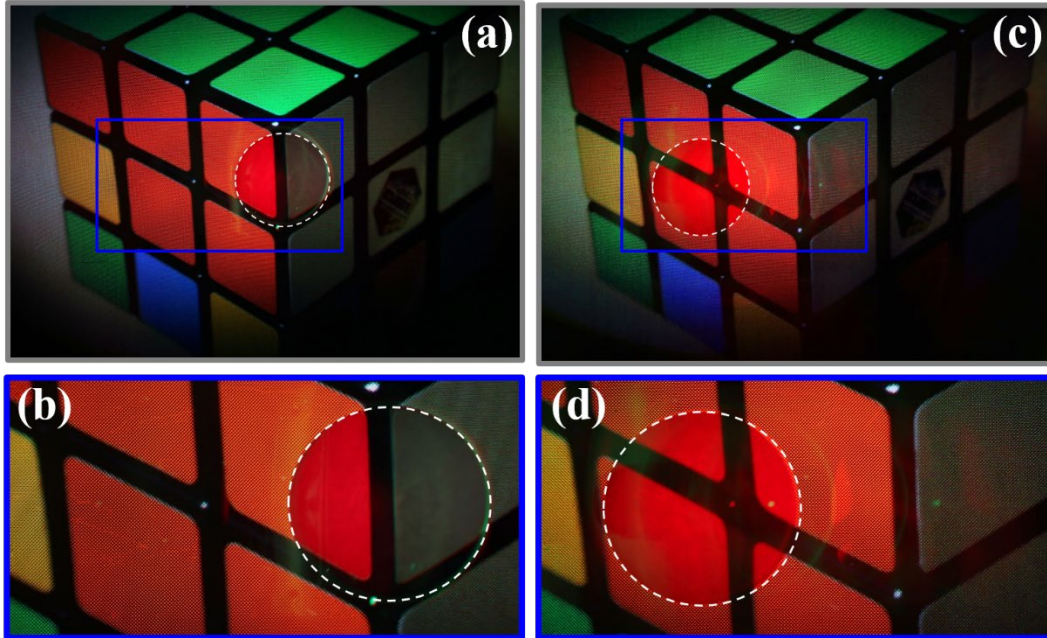


**Figure 4-12 | Multi-resolution display (picture) with PBD as image shifter:** a) high-resolution region in the center; b) magnified blue rectangle region in (a); c) shifted high-resolution region; d) magnified blue rectangle region in (c).

Monochromatic text [Fig. 4-11] and full-color picture [Fig. 4-12] were displayed by using our multi-resolution display with  $5\times$  enhancement. Their high-resolution regions can be successfully displaced with the help of an image shifter PBD. No obvious image blur occurs since laser backlight is adopted to avoid the grating's wavelength dispersion. Also, the high efficiency of PBD shifter, in theory  $\sim 100\%$ , can successfully eliminate the ghost image.

The preliminary results presented in Figs. 4-11 and 4-12 is mainly to demonstrate feasibility of hardware system. Further improvements on display performance can be implemented by image processing. For instance, the boundary transition between low- and high-resolution regions can be made to be smoother and less visible by applying blending image rendering algorithms. The smooth transition may be necessary for better immersive experience for users. Moreover, angular dispersion of diffraction grating may lead to color breakup when shifting high-resolution region to off-axis locations with PBD image shifter. This possible issue can be solved by pre-compensation, when processing display images on panel 2. R/G/B channels of the display content need to be processed separately, because these three wavelengths would have different deflection angles.

#### 4.5 Summary

In this chapter, we demonstrated a multi-resolution near-eye display system, to resolve one of major challenges in VR displays. Currently, the angular resolution of VR display, around  $10\sim 15$  ppd, is far below human visual acuity which requires  $>60$  ppd. Simply increasing pixel number may lead to several difficulties in panel fabrication, driving circuitry, data transfer and real-time

image rendering. From the point of bionics, we proposed a simple but efficient approach to match human visual acuity requirement.

In Section 4.2, we introduced the system configuration and working principle. Basically, we constructed a multi-resolution display system with a low resolution but wide FOV region for periphery and a narrow ultra-high-resolution region for central fovea. The detailed parameters of the optical setup were discussed as well. Then, we built up two prototypes in Section 4.3. The angular resolution has been enhanced by  $4\times$  to  $5\times$ , by an optical minifying system. MTF data was also measured to verify the enhancement ratio in our experiments. In Section 4.4, an image shifter PBD was also employed to relocate the high-resolution region, which can enable the future eye-tracking function. The proposed optical system can effectively reduce the screen-door effect in near-eye displays.



## CHAPTER 5: MULTIPLANE DISPLAY

### 5.1 Background

Most of current near-eye displays only provide one image focal plane, and their 3D perception is created by stereoscopic view based on binocular disparity [90-91]. Two different images are separately sent to the left and right eyes to generate the illusion of depth. After viewing stereoscopic 3D contents, many users reported adverse effects including headache and dizziness. The vergence-accommodation conflict issue is believed to be the main cause of visual discomfort and fatigue for near-eye displays [18-19]. As depicted in Fig. 5-1, when viewing real objects in natural world, the accommodation distance and vergence distance are always matched. However, in head-mounted displays, the accommodation cue keeps fixed on the display image plane, while the vergence distance varies with the display contents [72]. That would result in conflict between vergence and accommodation cues, as illustrated in Fig. 5-1(c) and (d). Recently, VAC issue is getting more and more attention from both academia and industry. In August 2018, Magic Leap released their first product, Magic Leap One, which creates two image depth by two sets of micro-display system. Actually, Magic Leap one is the first commercial product providing more than one image depth.

To resolve VAC issue, many approaches have been proposed [72, 85, 92-106]. Generally, these solutions can be divided into two categories [72]: static (space-multiplexed) and dynamic (time-multiplexed) approaches. Static category typically includes stacked panels [92-95], integral displays [96-97], and scanned fiber array [98]. Major challenges of static approaches are the

difficulties to stack multiple focal planes in a compact way, and the loss of display resolution and contrast [72].

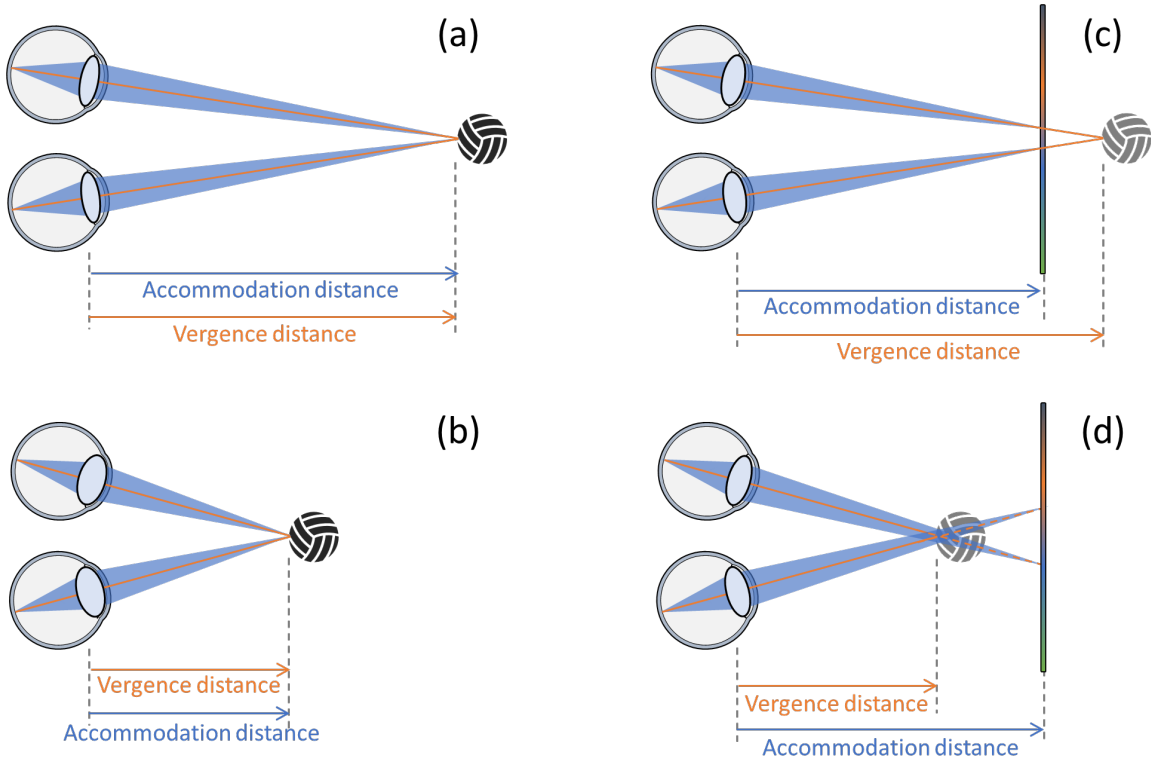


**Figure 5-1 | Conceptual illustration of VAC:** a) real object at far distance; b) real object at near distance; c) virtual object at far distance; d) virtual object at near distance.

Time-multiplexed methods do not necessarily involve multiple display screens, which enables more compact designs. Dynamic approaches change the image depths time-sequentially to provide the correct focus cues [72]. However, some tunable optical elements, such as deformable mirror [99], tunable lens [85, 100-103], switchable shutter [104] or diffuser [105-106], are needed in a dynamic design. While the main challenge of time-multiplexing is to provide sufficiently high frame rate of display panel and fast response time of tunable optics, in order to avoid image flickering. Actually, the refresh rate requirement is proportional to the number of

focal surfaces. Especially for current commercial VR headsets, over 90 Hz display refresh rate is commonly used to reduce motion picture response time [107]. Thus, as to time-multiplexed approaches, 180 Hz refresh rate is required for two focal depths and 270 Hz for three focal depths. Such a high frame rate would lead to higher power consumption and complicated driving circuitry.

In this chapter, we proposed a novel polarization multiplexing approach, which is different from convention space- or time-multiplexing methods. Our key optical element is a polarization-selective bi-focal Pancharatnam-Berry phase lens (PBL). In our system design, a PBL is employed to generate two focal planes and a liquid crystal spatial polarization modulator (SPM) is then applied to send correct images to these two images planes simultaneously. The proposed method can generate two independent image planes without sacrificing temporal or spatial complexities.

## 5.2 System configuration

One of the key components in our system is a Pancharatnam-Berry phase lens. As discussed in Section 4.4, the PB elements exhibit excellent optical behaviors with very high efficiency. Another unique feature of PB optical element is the high selectivity on incident polarization state. As illustrated in Eq. (9), the introduced PB phase delays are opposite for LCP and RCP, respectively. In a PB lens, the spatial distribution of LC director azimuthal angle  $\phi(x, y)$  follows paraboloid function, as Fig. 5-2(a) illustrates. Thus, for a circularly polarized light, a paraboloid phase distribution can be constructed. Please note that the phase profiles of LCP and RCP lights have opposite signs [Fig. 5-2(b)]. Therefore, if the PBL is designed to work as a diverging lens for LCP, then it is a converging lens for RCP, as Fig. 5-3 depicts. Basically, PBL is a polarization-sensitive bifocal lens with very high polarization selectivity.

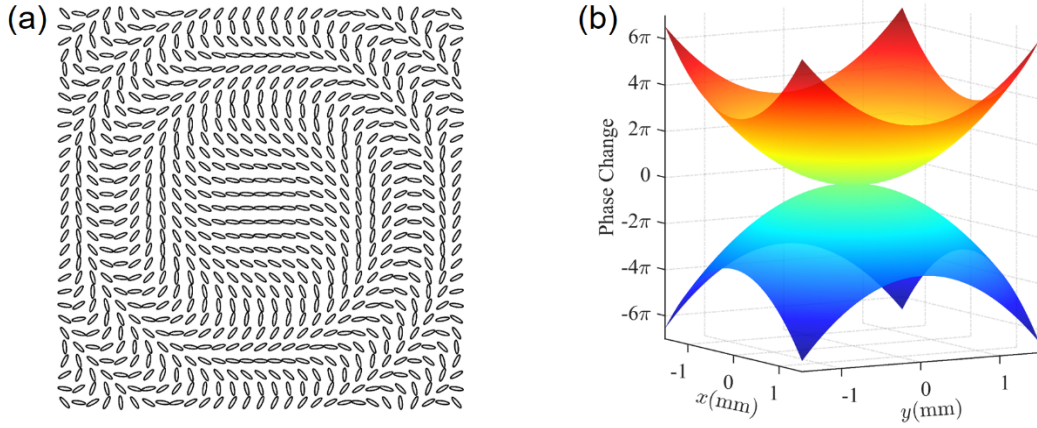


**Figure 5-2 | Working principle of Pancharatnam-Berry phase lens.** (a) Top view of the LC director distribution and (b) phase change profile of a PBL with  $\pm 0.8D$  optical power for RCP and LCP, respectively

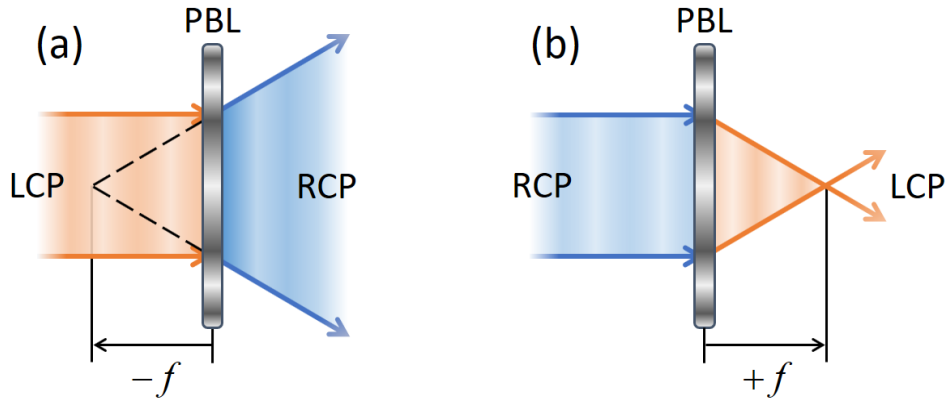


**Figure 5-3 | Optical behaviors of PBL.** (a) PBL serves as a diverging lens for LCP light and (b) it is a converging lens for RCP light.

From Fig. 5-3, a PBL can offer two focal planes, depending on the incident light polarization state. Therefore, time-multiplexing operation is not necessary to generate multiple image planes. However, achieving multiple image planes is just the first step to realize multi-plane or light field display. Next, we need to assign correct and independent images to these focal planes. Based on PBL's excellent polarization selectivity, we can adopt the polarization-multiplexing operation to send independent images to the focal planes. The LCP and RCP are a set of basis for

optical polarization state space. For a polarized light, it can be represented as a superposition of LCP and RCP waves, and its LCP and RCP components can be independently sent to PBL's two focal planes, respectively. Thus, by modulating the incident light polarization, we can easily control the ratios of LCP and RCP, and generate independent images for two focal planes.

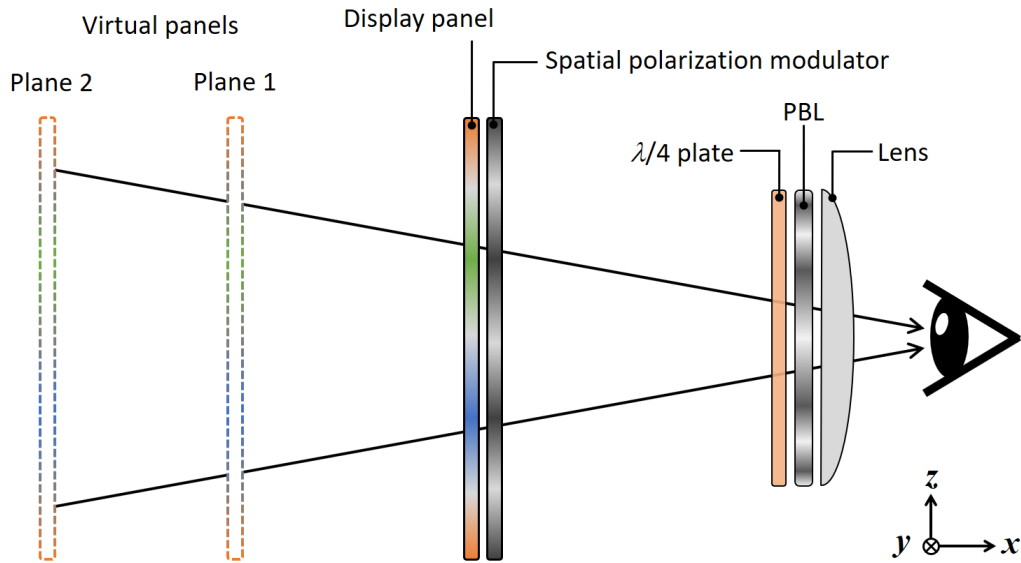


**Figure 5-4 | Configuration of the proposed polarization-multiplexed multiplane display system.**

Figure 5-4 presents the system configuration of the proposed polarization-multiplexed multiplane display. The display panel shown in Fig. 5-4 can be a liquid crystal display (LCD) or an organic light emitting diode (OLED) display panel with a circular polarizer. Without losing generality, we can assume the display panel emits a linearly polarized light along z-axis ( $0^\circ$ ). Then a spatial polarization modulator (SPM) is closely integrated and aligned to the display panel. The SPM in Fig. 5-4 is designed to achieve full modulation between two orthogonal polarization states, namely from  $0^\circ$  to  $90^\circ$  in our system. With a broadband quarter-wave plate oriented at  $45^\circ$ , these two orthogonal linear polarizations would be converted to RCP and LCP waves, respectively. In

addition, SPM can continuously control the polarization state, so that the relative ratio of RCP and LCP components can be continuously tuned. With the help of polarization-sensitive PBL, RCP and LCP components will be sent to two virtual planes simultaneously, as Fig. 5-4 shows. In brief, the PBL simultaneously provides two focal image planes and SPM directs the images to these two focal planes.

In Fig. 5-4, the display panel and polarization modulator jointly determine the displayed images of two virtual planes. How to input correct information data also needs to be carefully considered. The target light intensity distributions in plane 1 and plane 2 are denoted as  $I_1$  and  $I_2$ , respectively. The display panel in Fig. 5-4 should provide total light intensity  $I_{DP}$  as:

$$I_{DP} = I_1 + I_2. \quad (12)$$

Then SPM is used to separate the two focal plane images. After polarization modulation, the proportion of  $0^\circ$  and  $90^\circ$  polarization components to the total intensity should be:

$$\begin{aligned} t_{0^\circ} &= I_1 / (I_1 + I_2), \\ t_{90^\circ} &= I_2 / (I_1 + I_2). \end{aligned} \quad (13)$$

From Eq. (13),  $t_{0^\circ}$  and  $t_{90^\circ}$  can vary from 0 to 1. That requires a full-range polarization modulation. Then, after quarter-wave plate and PBL,  $I_1$  and  $I_2$  can be successively assigned to virtual planes 1 and 2.

Fig. 5-5 gives one simple example to understand the polarization state change in the proposed display system. The display panel, no matter LCD or OLED, can emit linearly polarized light, with polarization direction  $0^\circ$ . A pixelated SPM is used to modulate polarization state between two orthogonal polarizations. The polarization state of each pixel can be independently modulated to  $0^\circ$ ,  $45^\circ$ ,  $90^\circ$  or any intermediate polarization states. Each pixel may have different

polarizations after SPM. After passing through a  $\lambda/4$  waveplate (optical axis  $45^\circ$ ), the  $0^\circ$  polarization would be converted to LCP, and  $90^\circ$  polarization is converted to RCP. These intermediate polarization states will also be converted to elliptical polarizations. PB lens is highly sensitive to hardness of circular polarization state. With the help of PBL, for each pixel, its LCP component will be sent to virtual plane 1, and RCP component will be assigned to plane 2. Then, the gray level can be generated. Finally, we can get two focal image planes, and are able to send independent images to virtual plane 1 and 2 simultaneously.

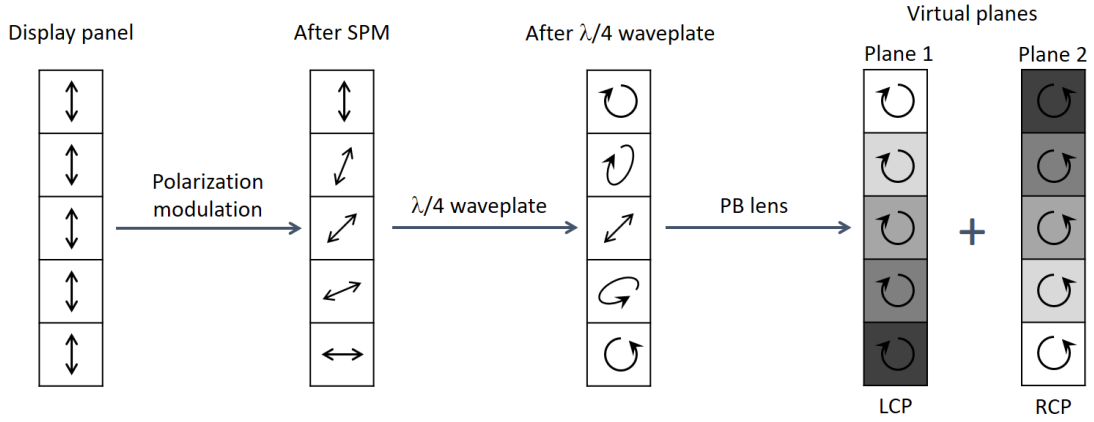


**Figure 5-5 | One example of polarization state change in the proposed polarization-multiplexing design.**

### 5.3 Experimental prototyping

In experiments, we used a 4.7-inch 60-Hz LCD panel with resolution  $1334 \times 750$  as the display panel. In order to prepare a SPM, we removed the polarizers of a commercial twisted-nematic (TN) LCD (5.0-inch, 60-Hz,  $800 \times 480$ ) and successfully made it into a spatial polarization modulator. The reasons why we chose TN LCD are twofold: 1) it can easily offer a full-range modulation, and 2) it is a broadband device [108].

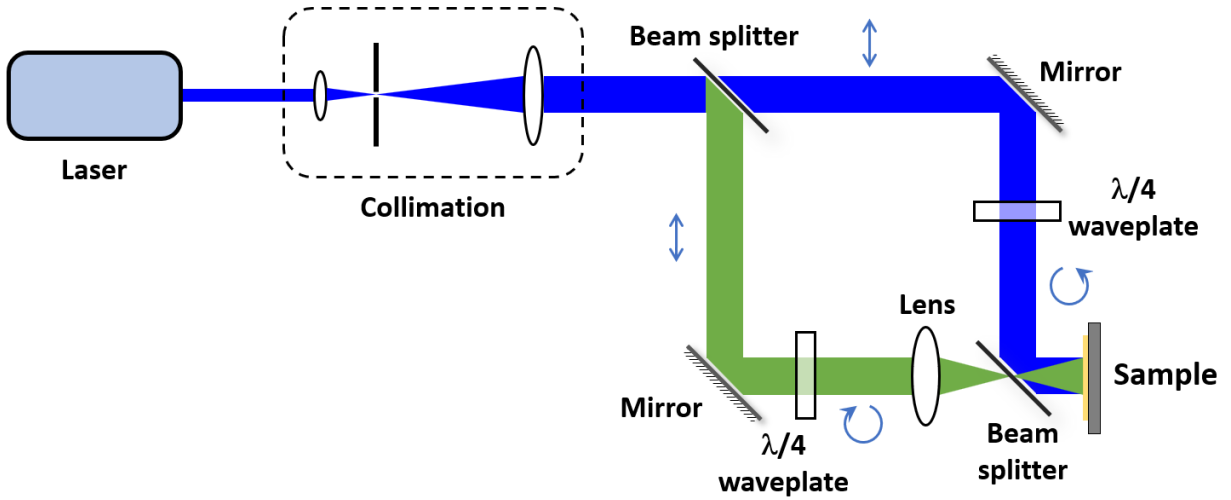


**Figure 5-6 | Optical setup of polarization interference exposure used in PBL fabrication**

We fabricated a 2.5-inch PBL with optical power  $\pm 0.8\text{D}$  by interference exposure [85-87]. The fabrication process of PBL is actually quite similar to that of PB deflector in Section 4.4. While a different polarization interferometry was used to record the lens phase profile on the photoalignment layer. The optical setup is plotted in Fig. 5-6. A convex lens was positioned in one arm to obtain the desired interference pattern. After interference exposure, a UV-curable diluted LC monomer (RM257) was coated on the exposed substrate surface. Then the coated substrate was cured by a UV light, forming a thin cross-linked LC polymer layer. The PB lens was designed to match the half-wave requirement for  $\lambda=550\text{ nm}$ . Please note that the depth difference can be easily tuned by changing the optical setup of interference exposure. Moreover, in our system [Fig. 5-4], a positive lens with optical power 10D was applied to provide a biased focusing power and to place two virtual planes at the suitable depths. Thus, the accommodation depths of two focal images are 0.1 D and 1.7 D, respectively. The horizontal field of view is close to  $\pm 35^\circ$  in our proof-of-concept experimental demonstrations.



Before constructing a multiplane display, we need to examine the display reproduction capability for these two focal planes. Based on Eq. (12) and Eq. (13), we calculated  $I_{DP}$ ,  $t_{0^\circ}$  and  $t_{90^\circ}$  for two target images with letter “A” and “B”. RGB channels in the full-color images were separately processed. Moreover, the gamma 2.2 correction in practical display panel was taken into consideration as well. Then we loaded the intensity information  $I_{DP}$  to display panel and polarization modulation  $t_{0^\circ}$  and  $t_{90^\circ}$  to SPM. To examine the crosstalk between two focal plane images, we inserted right-handed and left-handed circular polarizers successively just after the quarter-wave plate. The experimental photographs are shown in Fig. 5-7. Our system can successfully reproduce two images with correct polarizations: letter “A” in RCP [Fig. 5-7(e)] and “B” in LCP [Fig. 5-7(f)]. While one may notice that there still exists very little crosstalk in Figs. 5-7(e) and (f). Detailed measurements indicate that the crosstalk between these two orthogonal polarizations is: 0.27%, 0.42% and 4.83% for  $\lambda = 457$  nm, 514 nm and 633 nm, respectively. Actually, this crosstalk comes from the commercial TN panel, since it is optimized for display at  $\lambda \approx 550$  nm, instead of polarization modulation.

With the help of PBL, these two images with orthogonal polarizations should be sent to different focal depths. Letters “A” and “B” exist simultaneously while they are located at different depths [Fig. 5-8]. With the camera focusing at front virtual plane 1 [Fig. 5-8(a)], letter “A” was on focus with clear and sharp edges, while letter “B” was blurred. When focusing at rear plane, “A” became blurry.

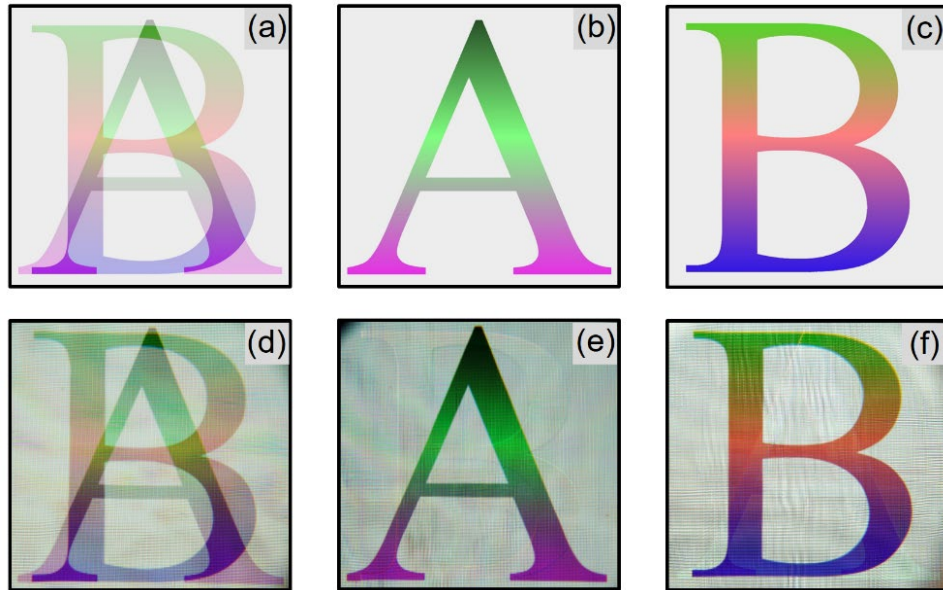


**Figure 5-7 | Experimental photographs after polarization modulation.** Target images: a) without CP, b) with right-handed CP and c) with left-handed CP. Experimental results: d) without CP, e) with right-handed CP, and f) with left-handed CP.

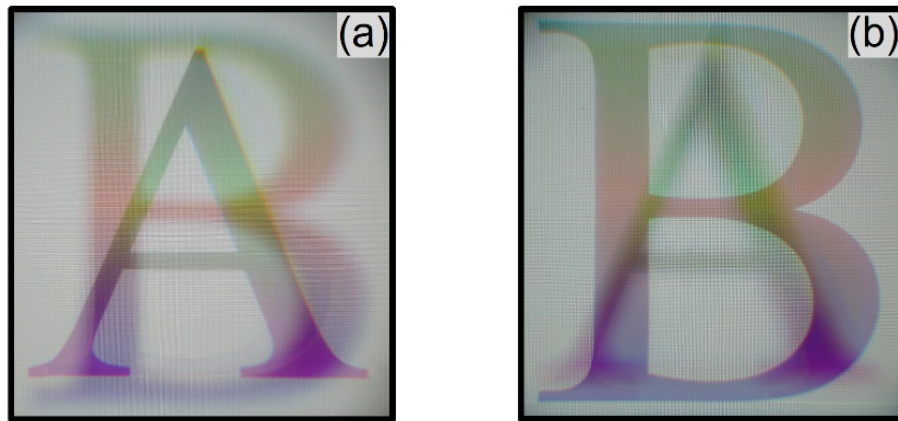


**Figure 5-8 | Experimental photographs of two image planes with letters 'A' and 'B'.** Camera focusing at a) virtual plane 1 and b) virtual plane 2.

#### 5.4 Image rendering

To create correct 3D perception, the display images on two focal planes should be designed and optimized. Several different image rendering methods can be applied on our system to generate

3D perception [85, 95, 103, 109-110]. Here we adopted an additive factorization method to generate all the 2D images for corresponding image depths [95, 103]. Since virtual planes 1 and 2 exist simultaneously as Fig. 5-9 depicts, total light intensity  $I_{total}$  along a specific direction can be directly calculated by:

$$I_{total} = I_{1i} + I_{2j}, \quad (14)$$

where  $I_{1i}$  and  $I_{2j}$  represent the intensity of specific pixels along specific direction from first and second virtual planes. After optimization, these two images can be generated. In our system with two virtual planes, we rendered two images for the 16×16 mm eye-box size with 5×5 viewing points. The rendered images are shown in Fig. 5-10.

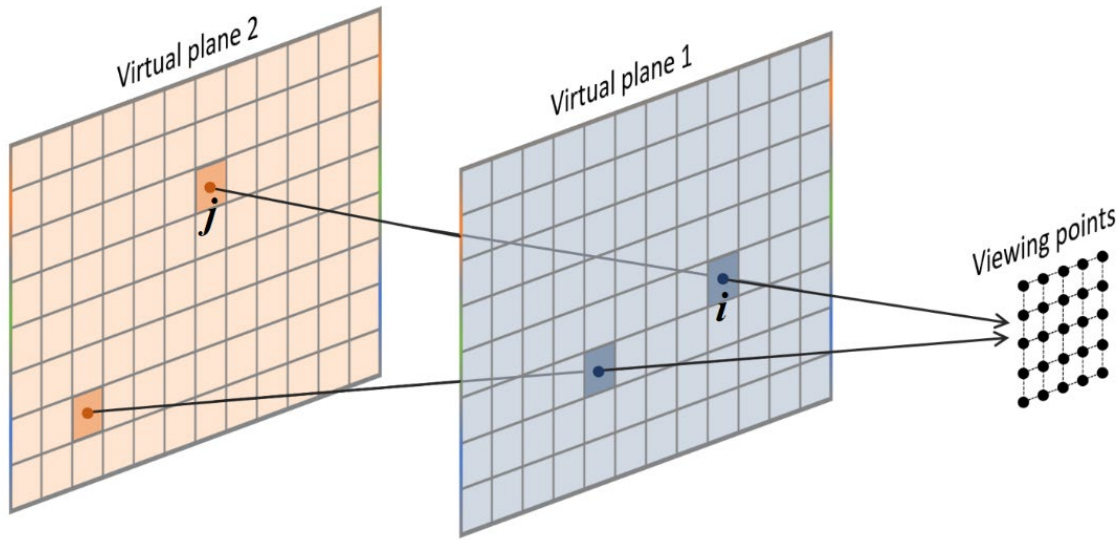


**Figure 5-9 | Schematic diagram of the additive light-field rendering method.**

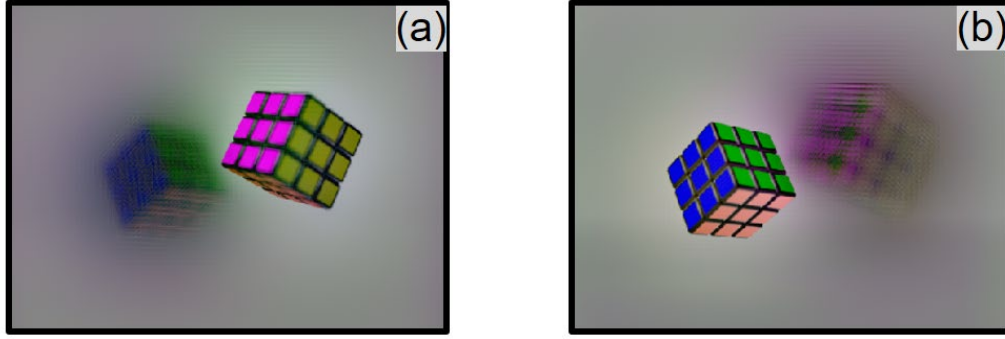


**Figure 5-10 | The rendered 2D images for an additive light field display.** (a) image to be displayed virtual plane 1 and (b) virtual plane 2.

With the rendered images obtained [Fig. 5-10], we calculated the intensity information  $I_{DP}$  and polarization modulation  $t_{0^\circ}$  and  $t_{90^\circ}$  by Eq. (12) and Eq. (13). With the images correctly displayed at virtual planes, an additive light field display system was constructed. The experimental results are presented in Fig. 5-11 and Fig. 5-12. Two cubes located at two different depths: the red-yellow cube at near distance and the blue-green one at far distance. The blue-green cube was blurry when focusing at front plane [Fig. 5-11(a)], while the red-yellow cube became blurry when focusing at rear plane [Fig. 5-12(b)].

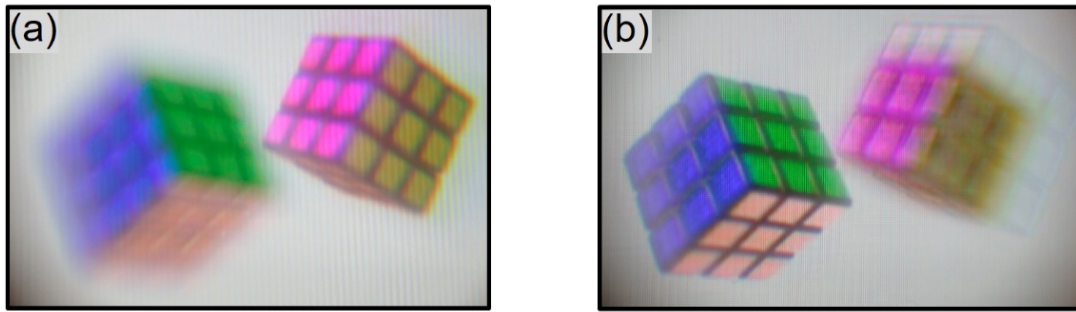


**Figure 5-11 | Experimental photographs of two image planes with two cubes.** The photographs captured with camera focusing at: a) front object and b) rear object.

Figure 5-12 shows the photographs at different viewing positions. Obvious 3D parallax effect is clearly illustrated in Fig. 5-12. From different viewing points, we can see slightly different

images. For instance, from left [Figs. 5-12(d)] to right [Figs. 5-12(f)], two cubes get closer and closer. Especially, at right viewing points [Figs. 5-12(c), (f) and (i)], the front pink-yellow cube blocks a portion of the rear blue-green cube. Figures 5-11 and 5-12 demonstrate that our proposed system can successfully realize a multiplane display with correct 3D reproduction capability. Since there are only two image planes in this proof-of-concept experiment, the occlusion issue is not well addressed [Figs. 5-12(c) and (f)], in which more image planes are eventually needed.

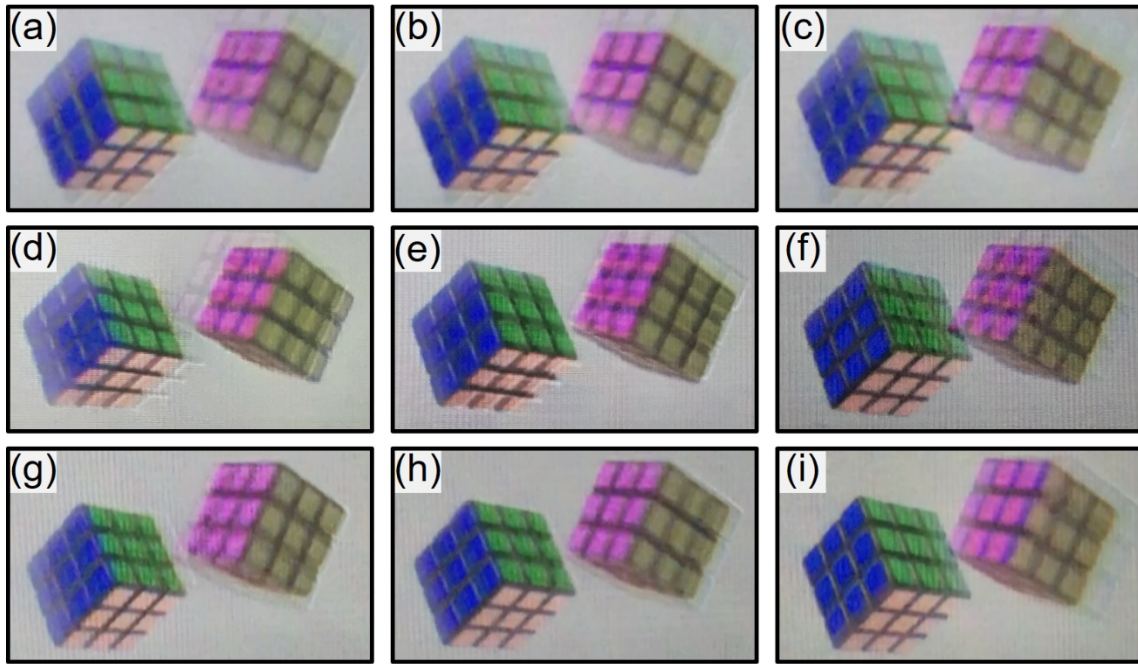


**Figure 5-12 | Experimental photographs of the multi-plane display at different viewing position:** a) upper-left, b) upper, c) upper-right, d) left, e) central, f) right, g) lower-left, h) lower, and i) lower-right.

### 5.5 Hybrid multiplexed display

In our experiments, we use one PBL to achieve two focal planes for proof-of-concept demonstration. To further improve the quality and functionality, the number of image planes, spacing between adjacent planes and image rendering algorithm all need to be taken into

consideration. The spacing between two adjacent planes should be  $\sim 0.6D$  and 5~6 image planes are eventually needed [111]. Polarization multiplexing is not actually competing with other multiplexing operations. Instead, it can help to provide more degrees of freedom. The proposed polarization-multiplexed approach can also be easily integrated with the conventional space- or time-multiplexed configurations to provide more focal planes.

We built up a four-plane hybrid space-/polarization-multiplexing display system. Fig. 5-13 presents the schematic illustration of combining polarization multiplexing with space multiplexing to provide more focal planes. Some preliminary results are shown in Fig. 5-14. We rendered for images to locate four digits, “1”, “2”, “3”, “4”, at different depths, respectively. When camera focusing on one focal plane, the corresponding digit is clear while other digits are blurry.

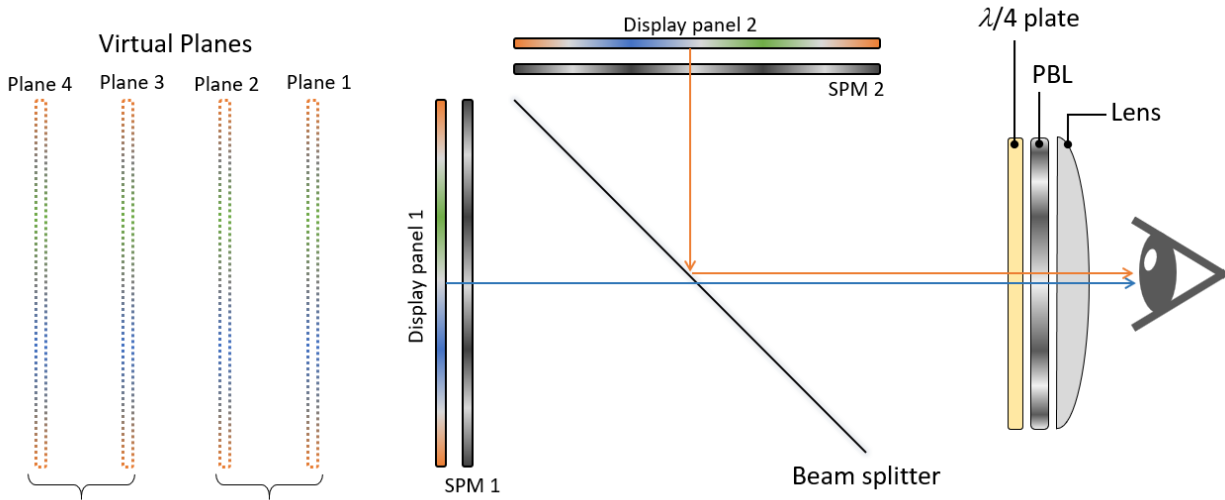


**Figure 5-13 | One example of hybrid space- and polarization-multiplexed four-plane display.**



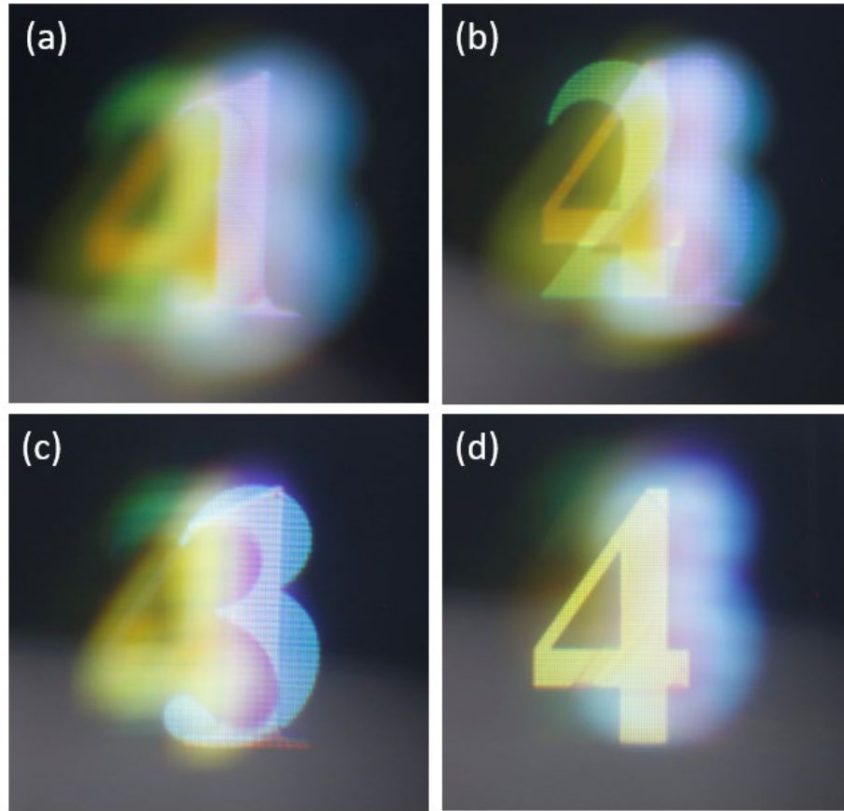


**Figure 5-14 | Experimental photographs of four image planes with four digits.** The photographs captured with camera focusing at: a) the first focal plane, b) the second focal plane, c) the third focal plane and d) the fourth focal plane.

It is also achievable to integrate polarization multiplexing with time multiplexing operation. An easiest way is to make the PB lens used in our experiments to be a switchable device [103], as presented in Fig. 5-15. Then, one PB lens can provide three states: focusing, defocusing and transmission without lensing effect. At least three focal planes can be achieved by only one switchable PBL. Stacking more PBL can further increase the number of focal planes, while the trade-off is the higher refresh rate of display panel and SPM.

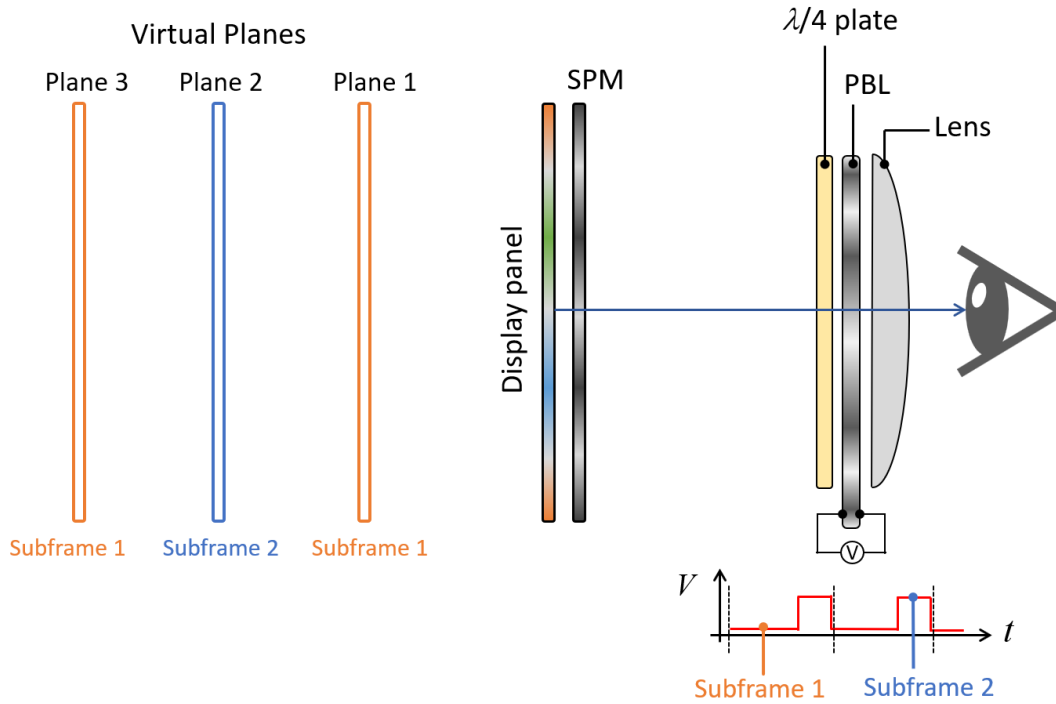


**Figure 5-15 | One example of hybrid time- and polarization-multiplexed three-plane display.**

## 5.6 Discussion

From Fig. 5-11, Fig. 5-12 and Fig. 5-14, there remains noticeable ghost image, which could originate from the TN panel's polarization crosstalk [Fig. 5-7] and the wavelength-dependent efficiency of PBL. Normally, such a commercial TN panel is optimized for display applications at  $\lambda \approx 550$  nm. Thus, for the blue and red wavelengths, such a TN LCD deviates slightly from an ideal polarization rotator, which leads to the observed crosstalk between two focal image planes. One way to mitigate this issue is to slightly increase the  $d\Delta n$  value of the TN LCD and to apply different optimal operation voltages when driving R/G/B pixels, respectively. The second reason of the ghost image may come from the efficiency drop of the PBL. It is easy to understand that the PBL



used in our prototype is optimized for green light. Only for  $\lambda \approx 550$  nm, the half-wave requirement is satisfied. The optical efficiency would drop when the wavelength deviates from the optimal wavelength. To address this issue, a dual-twist structure [112-115] can be adopted to effectively improve the efficiency to >95% within the whole visible range.

As for virtual reality displays, a  $6K \times 6K$  resolution is desirable to eliminate the screen-door effect, as discussed in Section 4.1. Our proposed multiplane display should also be able to support high resolution applications. In our design, we employed two pixelated panels, which may cause several issues, including reduced brightness and Moiré pattern. Especially, as the resolution increases, these issues may become even more severe. Actually, the second panel, namely SPM, is utilized mainly to provide depth information. Thus, it is not required for SPM to match the resolution of display panel. A relatively lower resolution of SPM helps to reduce possible Moiré effect when two panels are aligned together, and to improve the optical efficiency.

## 5.7 Summary

In this chapter, we mainly focused on the third challenges, namely VAC issue, in current near-eye displays. Stereoscopic 3D display is commonly adopted in most of current VR headsets. While stereoscopic display with one image plane usually causes the conflict between vergence cue and accommodation cue. VAC is believed to be the main reason for dizziness and visual discomfort when wearing VR headsets. VAC issue has become one of the biggest challenge in VR headsets and needs to be overcome in order to provide better user experience.

In Section 5.1, we reviewed several previous approaches to solve the VAC issue. They are all based on space multiplexing and time multiplexing. We proposed a novel polarization-

multiplexed multiplane display design to overcome the VAC issue in Section 5.2. The depth information is coded by the polarization states of each pixel by a SPM, and then is reproduced by the polarization-sensitive bi-focal PB lens. In Section 5.4, we applied additive light field rendering to successfully reproduce correct 3D contents. Our proposed polarization-multiplexing method can be easily incorporated with conventional space- or time-multiplexing. We gave two examples and presented some preliminary results in Section 5.5. Some potential issues and drawbacks were discussed, and several possible solutions were also proposed in Section 5.6. We believe that the polarization multiplexing is a novel approach to offers more degrees of freedom, and to alleviate the trade-off between frame rate and the focal plane number.

## CHAPTER 6: CONCLUSION

In this dissertation, we mainly focused on three major challenges of current near-eye VR display systems: 1) limited dynamic range of display brightness and contrast, 2) insufficient angular resolution and 3) vergence-accommodation conflict issue.

To improve the HDR performance, we investigated the possible solutions for both LCDs and OLEDs. In Chapter two, we proposed a mini-LED local dimming backlight for LCD. We developed a validate simulation model to analyze the performance of HDR LCD using a two-dimensional local dimming mini-LED backlight. The halo effect of the proposed HDR display system was investigated by both numerical simulation and human visual perception experiment. We found that halo effect is mainly governed by two factors: intrinsic LCD contrast ratio and dimming zone number. Based on our results, to suppress halo effect to indistinguishable level, a LCD with  $CR \approx 5000:1$  requires  $\sim 200$  local dimming zones, while for a LCD with  $CR \approx 2000:1$  the required number of dimming zones is over 3000. Our model provides useful guidelines to optimize the mini-LED backlit LCDs for achieving dynamic contrast ratio comparable to organic LED displays.

While for OLED display with prefect dark state, its limitation of dynamic range is not from dark state. Instead, the dynamic range is actually limited by peak brightness. Microcavity effect is a commonly-used method to enhance optical efficiency and peak brightness. However, a major tradeoff of the strong cavity effect is its apparent angular color shift, especially for RGB-based OLED displays, due to their mismatched angular intensity distributions. To mitigate the color shift, we first analyzed the emission spectrum shifts and angular distributions for the OLEDs with strong

and weak cavities, both theoretically and experimentally. Excellent agreement between simulation and measurement has been obtained. Next, we proposed a systematic approach for RGB-OLED displays based on multi-objective optimization algorithms. Three objectives, namely external quantum efficiency (EQE), color gamut coverage, and angular color shift of primary and mixed colors, can be optimized simultaneously. Our optimization algorithm has been proven to be an efficient approach for optimizing the microcavity effect of RGB-OLED display system.

Insufficient angular resolution can greatly degrade immersive experience of current VR headsets, which is becoming an urgent challenge needs to be solved. In Chapter four, we proposed a multi-resolution foveated display for near-eye displays. Two display panels were adopted in our system: the first one provides a wide FOV, while the second one offers an ultra-high resolution at the central fovea region. Especially, by an optical minifying system, resolution of the second panel can be enhanced by up to  $5\times$ , which is approaching the human-eye acuity. Moreover, a Pancharatnam-Berry phase deflector was applied to actively shift the high-resolution region, in order to integrate with gaze-contingent functions. Our proposed design only requires two relatively low-resolution panels, which can avoid the fabrication and driving difficulties for high-resolution display panel. In addition, the proposed foveated display design can be easily integrated into varifocal or light field display systems. The foveated display system is an efficient way to deliver both high angular resolution and wide field of view to VR users.

Resolving VAC issue has become a very hot topic for near-eye displays. In Chapter five, a multiplane display system was proposed to address the VAC issue, which is the major cause of visual discomfort and fatigue when wearing VR headsets. The conventional space-multiplexing solutions usually lose compactness and display resolution and contrast. While the time-

multiplexing methods require higher display frame rate and fast response time of tunable optics. We proposed a multiplane display using polarization-multiplexing operation, instead of space- or time-multiplexing. A bi-focal PB lens with high polarization selectivity was implemented to generate two focal depths simultaneously. A spatial polarization modulator was then utilized to direct the two images to designated focal planes. Based on this design, a dual-focal-plane display system was constructed in our prototype. This method enables the generation of two image planes without the need for temporal multiplexing or switchable lenses. Thus, the proposed design can effectively reduce the frame rate by one half. The proposed polarization-multiplexing operation is a novel method to realize multi-plane display system, without increasing spatial or temporal complexities. It can help to release the burdens of space- and time-multiplexing.

## **APPENDIX: STUDENT PUBLICATIONS**

### Journal publications

- [1] T. Zhan, J. Xiong, G. Tan, Y. H. Lee, J. Yang, S. Liu, and S. T. Wu, “Enhancing near-eye display resolution by polarization multiplexing,” Opt. Express 27, (2019). (In press)
- [2] F. Gou, E-L. Xiang, G. Tan, P-T. Chou, Y-L. Li, Y-F. Lan, and S-T. Wu, “Angular color shift of micro-LED displays,” Opt. Express 27, (2019). (In press)
- [3] Y. Huang, G. Tan, F. Gou, M. C. Li, S. L. Lee, and S. T. Wu, “Prospects and challenges of mini-LED and micro-LED displays,” J. SID, 27, (2019). DOI: 10.1002/jsid.760
- [4] C. Zhang, Z. He, H. Chen, L. Zhou, G. Tan, S. T. Wu, and Y. Dong, “Light diffusing, down-converting perovskite-on-polymer microspheres,” J. Mater. Chem. C (2019). DOI: 10.1039/C9TC01130G
- [5] Z. He, G. Tan, D. Chanda, and S. T. Wu, “Novel liquid crystal photonic devices enabled by two-photon polymerization,” Opt. Express 27(8), 11472-11491 (2019).
- [6] F. Gou, E. L. Hsiang, G. Tan, Y. F. Lan, C. Y. Tsai, and S. T. Wu, “High performance color-converted micro-LED displays,” J. SID 27(4), 199-206 (2019).
- [7] T. Zhan, Y. H. Lee, J. Xiong, G. Tan, K. Yin, J. Yang, S. Liu, and S. T. Wu, “High-efficiency switchable optical elements for advanced head-up displays,” J. SID 27(4), 223-231 (2019).
- [8] T. Zhan, Y. H. Lee, G. Tan, J. Xiong, K. Yin, F. Gou, J. Zou, N. Zhang, D. Zhao, J. Yang, S. Liu, and S. T. Wu, “Pancharatnam-Berry optical elements for head-up and near-eye displays,” J. Opt. Soc. Am. B 36(5), (2019).

- [9] F. Gou, E. L. Hsiang, G. Tan, Y.-F. Lan, C.-Y. Tsai, and S. T. Wu, "Tripling the optical efficiency of color-converted micro-LED displays with funnel-tube array," *Crystals* 9(1), 39 (2019).
- [10] G. Tan, T. Zhan, Y. H. Lee, J. Xiong, and S. T. Wu, "Polarization-multiplexed multiplane display," *Opt. Lett.* 43(22), 5651-5654 (2018).
- [11] G. Tan, Y. H. Lee, T. Zhan, J. Yang, S. Liu, D. F. Zhao, and S. T. Wu, "Foveated imaging for near-eye displays," *Opt. Express* 26(19), 25076-25085 (2018).
- [12] G. Tan, Y. Huang, M. C. Li, S. L. Lee, and S. T. Wu, "High dynamic range liquid crystal displays with a mini-LED backlight," *Opt. Express* 26(13), 16572-16584 (2018).
- [13] Y. H. Lee, G. Tan, K. Yin, T. Zhan, and S. T. Wu, "Compact see-through near-eye display with depth adaption," *J. SID* 26(2), 64-70 (2018).
- [14] H. Chen, G. Tan, and S. T. Wu, "Ambient contrast ratio of LCDs and OLED displays," *Opt. Express* 25(26), 33643-33656 (2017).
- [15] G. Tan, J. H. Lee, S. C. Lin, R. Zhu, S. H. Choi, and S. T. Wu, "Analysis and optimization on the angular color shift of RGB OLED displays," *Opt. Express* 25(26), 33629-33642 (2017).
- [16] G. Liu, Y. H. Lee, Y. Huang, Z. Zhu, G. Tan, M. Q. Cai, P.-P. Li, D. Wang, Y. Li, S. Pang, C. Tu, S.T. Wu, and H.-T. Wang, "Dielectric broadband meta-vector-polarizers based on nematic liquid crystal," *APL Photonics* 2(12), (2017).
- [17] G. Tan, Y. H. Lee, F. Gou, H. Chen, Y. Huang, Y.F. Lan, C.Y. Tsai, and S. T. Wu, "Review on polymer-stabilized short-pitch cholesteric liquid crystal displays," *J. Phys. D: Appl. Phys.* 50, 493001 (2017).



- [18] Y. H. Lee, G. Tan, T. Zhan, Y. Weng, G. Liu, F. Gou, F. Peng, N.V. Tabiryan, S. Gauza, and S. T. Wu, "Recent progress in Pancharatnam-Berry phase optical elements and the applications for virtual/augmented realities," *Optical Data Processing and Storage* 3, 79-88 (2017).
- [19] G. Tan, J. H. Lee, Y.-H. Lan, M.-K. Wei, L. H. Peng, I C. Cheng, and S. T. Wu, "Broadband antireflection film with Moth-eye-like structure for flexible display application," *Optica* 4(7), 678-683 (2017).
- [20] H. Chen, G. Tan, M. C. Li, S. L. Lee, and S. T. Wu, "Depolarization effect in liquid crystal displays," *Opt. Express* 25(10), 11315-11328 (2017).
- [21] G. Tan, Y. H. Lee, F. Gou, M. Hu, Y. F. Lan, C. Y. Tsai, and S. T. Wu, "Macroscopic model for analyzing the electro-optics of uniform lying helix cholesteric liquid crystals," *J. Appl. Phys.* 121, 173102 (2017).
- [22] Y. Huang, H. Chen, G. Tan, H. Tobata, S-I Yamamoto, E. Okabe, Y. F. Lan, C. Y. Tsai, and S. T. Wu, "Optimized blue-phase liquid crystal for field-sequential-color displays," *Opt. Mater. Express* 7(2), 641-650 (2017).
- [23] H. Chen, R. Zhu, G. Tan, M.C. Li, S. L. Lee, and S. T. Wu, "Enlarging the color gamut of liquid crystal displays with a functional reflective polarizer," *Opt. Express* 25(1), 102-111 (2017).
- [24] H. Chen, G. Tan, Y. Huang, Y. Weng, T. H. Choi, T. H. Yoon and S. T. Wu, "A low voltage liquid crystal phase grating with switchable diffraction angles," *Sci. Rept.* 7, 39923 (2017).

- [25] G. Tan, R. Zhu, Y. S. Tsai, K. C. Lee, Z. Luo, Y. Z. Lee, and S. T. Wu, "High ambient contrast ratio OLED and QLED without a circular polarizer," J. Phys. D: Appl. Phys. 49, 315101 (2016).
- [26] R. Zhu, H. Chen, T. Kosa, P. Coutino, G. Tan, and S. T. Wu, "High-ambient-contrast augmented reality with a tunable transmittance liquid crystal film and a functional reflective polarizer," J. SID 24(4), 229-233 (2016).
- [27] R. Zhu, G. Tan, J. Yuan, and S. T. Wu, "Functional reflective polarizer for augmented reality and color vision deficiency," Opt. Express 24(5), 5431-5441 (2016).
- [28] D. Xu, F. Peng, G. Tan, J. He and S. T. Wu, "A semi-empirical equation for the response time of in-plane switching liquid crystal display and measurement of twist elastic constant," J. Appl. Phys. 117, 203103 (2015).
- [29] J. Yuan, G. Tan, D. Xu, F. Peng, A. Lorenz and S. T. Wu, "Low-voltage and fast-response polymer-stabilized hyper-twisted nematic liquid crystal," Opt. Mater. Express 5, 1339-1347 (2015).
- [30] D. Xu, G. Tan and S. T. Wu, "Large-angle and high-efficiency tunable phase grating using fringe field switching liquid crystal," Opt. Express 23, 12274-12285 (2015).

#### Conference proceedings

- [1] G. Tan, T. Zhan, Y. H. Lee, J. Xiong, S. T. Wu, "Near-eye light field display with polarization multiplexing," Optical Design Challenge 2019, 110400E (February 2019).

- [2] Y. Huang, G. Tan, M. C. Li, S. L. Lee, S.T. Wu, “Emerging High-Dynamic-Range Mini-LED Displays,” Proc. SPIE, Advances in Display Technologies IX, 1094205 (February 2019).
- [3] G. Tan, H. Chen, Y.F. Lan, C.Y. Tsai, and S.T. Wu, “Wide-view and Fast-response Uniform Standing Helix Cholesteric LCD,” SID Symp. Digest 49(1), 1769-1772 (May 2018, Los Angeles, California).
- [4] H. Chen, G. Tan, M. C. Li, S. L. Lee, and S. T. Wu, “High Contrast Ratio LCD with an In-cell Polarizer,” SID Symp. Digest 49(1), 1734-1737 (May 2018, Los Angeles, California).
- [5] Y. H. Lee, G. Tan, K. Yin, T. Zhan, and S. T. Wu, “Compact See-through Near-eye Display with Depth Adaption,” SID Symp. Digest 49(1), 1060-1063 (May 2018, Los Angeles, California).
- [6] H. Chen, G. Tan, and S. T. Wu, “Can LCDs Outperform OLED Displays in Ambient Contrast Ratio?” SID Symp. Digest 49(1), 981-984 (May 2018, Los Angeles, California).
- [7] G. Tan, J. H. Lee, S. C. Lin, R. Zhu, S. H. Choi, and S. T. Wu, “Systematic Optimization for Achieving Indistinguishable Color Shift of RGB OLED Displays,” SID Symp. Digest 49(1), 418-421 (May 2018, Los Angeles, California).
- [8] C. Zhang, J. He, H. Chen, G. Tan, L. Zhou, S. T. Wu, Y. Sohn, and Y. Dong, “Converting Light Diffusing Polymer Powders into Stable Perovskite-Based Tunable Downconverters,” SID Symp. Digest 49(1), 222-224 (May 2018, Los Angeles, California).
- [9] G. Tan, Y. H. Lan, M. K. Wei, L. H. Peng, I.C. Cheng, S. T. Wu, and J. H. Lee. “Antireflection and self-cleaning film with moth-eye-like structure for mobile flexible

- displays,” Proc. SPIE 10556, Advances in Display Technologies VIII, 1055608 (March 2018).
- [10] F. Gou, Y.-H. Lee, G. Tan, M. Hu, Y.-F. Lan, C.-Y. Tsai, and S. T. Wu, "Submillisecond Grayscale Response Time of a Uniform Lying Helix Liquid Crystal," SID Symp. Digest 48(1), 1822-1825 (2017, Los Angeles, California).
  - [11] G. Tan, Y. H. Lee, F. Gou, M. Hu, Y. F. Lan, C. Y. Tsai, and S. T. Wu, "Figure of Merit for Optimizing the Performance of Uniform Lying Helix Cholesteric Liquid Crystals," SID Symp. Digest 48(1), 490-493 (2017, Los Angeles, California).
  - [12] Y. Huang, H. Chen, G. Tan, H. Tobata, S. Yamamoto, E. Okabe, Y. F. Lan, C. Y. Tsai, and S. T. Wu, "New Blue-Phase Liquid Crystal Optimized for Color-Sequential Displays," SID Symp. Digest 48(1), 486-489 (2017, Los Angeles, California).
  - [13] G. Tan, J. H. Lee, Y. H. Lan, M. K. Wei, L. H. Peng, I Cheng, and S. T. Wu, "Moth-eye Anti-reflection Surface for Sunlight Readable Flexible Displays," SID Symp. Digest 48(1), 574-577 (2017, Los Angeles, California).
  - [14] H. Chen, R. Zhu, G. Tan, M. C. Li, S. L. Lee, and S. T. Wu, "Wide-Color-Gamut LCD with a Functional Reflective Polarizer," SID Symp. Digest 48(1), 1659-1662 (2017, Los Angeles, California).
  - [15] Y. H. Lee, G. Tan, Y. Weng, and S. T. Wu, "Switchable Lens based on Cycloidal Diffractive Waveplate for AR and VR Applications," SID Symp. Digest 48(1), 1061-1064 (2017, Los Angeles, California).
  - [16] R. Zhu, H. Chen, G. Tan, T. Kosa, P. Coutino and S. T. Wu, "A High-Ambient-Contrast Augmented Reality System," SID Symp. Digest 47, 1025–1028 (2016, San Francisco)

- [17] G. Tan, R. Zhu, Y. S. Tsai, K. C. Lee, Z. Luo, Y. Z. Lee and S. T. Wu, “High Ambient Contrast Ratio OLED and Quantum-dot LED without a Circular Polarizer,” SID Symp. Digest 47, 1509–1512 (2016, San Francisco)
- [18] D. Xu, G. Tan and S. T. Wu, “Multi-angle Beam Steering for Head-Mounted Displays,” SID Symp. Digest 47, 1826–1829 (2016, San Francisco).

#### Patents

- [1] Y. H. Lee, T. Zhan, G. Tan, F. Gou, F. Peng, S. T. Wu, “Optical Display System with Enhanced Resolution, Methods, and Applications,” US Patent 10,115,327 B1 (Oct. 30, 2018).
- [2] Y. S. Tsai, K. C. Lee, S. T. Wu, G. Tan, R. Zhu, "Display device and optical film," US Patent 9,680,132 B1 (June. 13, 2017).

## REFERENCES

- [1] R. Azuma, Y. Baillet, R. Behringer, S. Feiner, S. Julier, and B. MacIntyre, "Recent advances in augmented reality," *IEEE Comput. Graph. Appl.* 21(6), 34-47 (2001).
- [2] S. K. Feiner, "Augmented reality: A new way of seeing," *Sci. Amer.* 54, 48-55 (2002).
- [3] P. Milgram and F. Kishino, "A taxonomy of mixed reality visual displays," *IEICE Trans. Information Systems* E77-D (12), 1321-1329 (1994).
- [4] H. Hua, "Enabling focus cues in head-mounted displays," *Proc. IEEE* 105(5), 805-824 (2017).
- [5] M. Schadt, "Milestone in the history of field-effect liquid crystal displays and materials," *Japan. J. Appl. Phys* 48(3S2), 03B001 (2009).
- [6] S. T. Wu and C. S. Wu, "Mixed-mode twisted nematic liquid crystal cells for reflective display," *Appl. Phys. Lett.* 68, 1455-1457 (1996).
- [7] P. F. Van Kessel, L. J. Hornbeck, R. E. Meier and M. R. Douglass, "A MEMS-based projection display," *Proc. IEEE* 86(8), 1687-1704 (1998).
- [8] W. O. Davis, R. Sprague, and J. Miller, "MEMS-based pico projector display," *Optical MEMs and Nanophotonics, 2008 IEEE/LEOS International Conference*, 31-32 (2008).
- [9] C. W. Tang and S. A. VanSlyke, "Organic electroluminescent diodes," *Appl. Phys. Lett.* 51(12), 913-915 (1987).
- [10] Y. Shirasaki, G. J. Supran, M. G. Bawendi and V. Bulović, "Emergence of colloidal quantum-dot light-emitting technologies," *Nat. photonics* 7(1), 13-23 (2013).

- [11] H. X. Jiang and J. Y. Lin, “Nitride micro-LEDs and beyond—A decade progress review,” *Opt. Express* 21, A475-A484 (2013).
- [12] H. Seetzen, W. Heidrich, W. Stuerzlinger, G. Ward, L. Whitehead, M. Trentacoste, A. Ghosh, and A. Vorozcovs, “High dynamic range display systems,” *ACM Trans. Graph.* 23(3), 760-768 (2004).
- [13] M. D. Fairchild, “The HDR photographic survey,” in *IS&T/SID 15th Color Imaging Conference*, (2007), 233-238.
- [14] M. D. Fairchild, “Seeing, adapting to, and reproducing the appearance of nature,” *Appl. Opt.* 54(4), B107-B116 (2015).
- [15] H. Chen, G. Tan, and S. T. Wu, “Ambient contrast ratio of LCDs and OLED displays,” *Opt. Express* 25(26), 33643-33656 (2017).
- [16] Y. H. Lee, T. Zhan, and S. T. Wu, “Prospects and challenges in augmented reality displays,” *Virtual Reality & Intelligence Hardware* 1(1), 10-20 (2019).
- [17] B. A. Wandell, *Foundations of Vision* (Sinauer Associates, 1995).
- [18] D. M. Hoffman, A. R. Girshick, K. Akeley, and M. S. Banks, “Vergence-accommodation conflicts hinder visual performance and cause visual fatigue,” *J. Vis.* 8(3), 33 (2008).
- [19] M. Lambooi, M. Fortuin, I. Heynderickx, and W. IJsselstein, “Visual discomfort and visual fatigue of stereoscopic displays: A review,” *J. Imaging Sci. Technol.* 53, 030201 (2009).
- [20] S. Daly, T. Kunkel, X. Sun, S. Farrell, and P. Crum, “Viewer preferences for shadow, diffuse, specular, and emissive luminance limits of high dynamic range displays,” *SID Symp. Dig. Tech. Papers* 44(1), 563-566 (2013).

- [21] R. Zhu, A. Sarkar, N. Emerton, and T. Large, “Reproducing high dynamic range contents adaptively based on display specifications,” *SID Symp. Dig. Tech. Papers* 48(1), 1188-1191 (2017).
- [22] H. Chen, R. Zhu, M. C. Li, S. L. Lee, and S. T. Wu, “Pixel-by-pixel local dimming for high-dynamic-range liquid crystal displays,” *Opt. Express* 25(3), 1973-1984 (2017).
- [23] H. Chen, J. He, and S. T. Wu, “Recent advances in quantum-dot-enhanced liquid crystal displays,” *IEEE. J. Selected Topics in Quantum Electronics*, 23(5), 1900611 (2017).
- [24] H. Chen, G. Tan, M. C. Li, S. L. Lee, and S. T. Wu, “Depolarization effect in liquid crystal displays,” *Opt. Express* 25(10), 11315-11328 (2017).
- [25] P. de Greef and H. G. Hulze, “Adaptive dimming and boosting backlight for LCD-TV Systems,” *SID Symp. Dig. Tech. Papers* 38(1), 1332-1335 (2007).
- [26] S. Cha, T. Choi, H. Lee, and S. Sull, “An optimized backlight local dimming algorithm for edge-lit LED backlight LCDs,” *J. Disp. Technol.* 11(4), 378-385 (2015).
- [27] T. Wu, C. W. Sher, Y. Lin, C. F. Lee, S. Liang, Y. Lu, S. W. Huang Chen, W. Guo, H. C. Kuo and Z. Chen, “Mini-LED and micro-LED: Promising candidates for the next generation display technology,” *Appl. Sci.* 8(9),1557 (2018).
- [28] Y. Huang, G. Tan, F. Gou, M. C. Li, S. L. Lee, and S. T. Wu, “Prospects and challenges of mini-LED and micro-LED displays,” *J. Soc. Inf. Display* 27, (2019). DOI: 10.1002/jsid.760
- [29] Z. Liu, W. C. Chong, K. M. Wong, and K. M. Lau, “GaN-based LED micro-displays for wearable applications,” *Microelectron. Eng.* 148, 98-103 (2015).



- [30] A. Paranjpe, J. Montgomery, S. M. Lee and C. Morath, "Micro-LED displays: key manufacturing challenges and solutions," *SID Symp. Dig. Tech. Papers* 49(1), 597-600 (2018).
- [31] Z. Deng, B. Zheng, J. Zheng, L. Wu, W. Yang, Z. Lin, P. Shen, and J. Li, "High dynamic range incell LCD with excellent performance," *SID Symp. Dig. Tech. Papers* 49(1), 996-998 (2018).
- [32] N. Burini, E. Nadernejad, J. Korhonen, S. Forchhammer, and X. Wu, "Modeling power-constrained optimal backlight dimming for color displays," *J. Disp. Technol.* 9(8), 656-665 (2013).
- [33] J. Korhonen, N. Burini, S. Forchhammer, J. M. Pedersen, "Modeling LCD displays with local backlight dimming for image quality assessment," *Proc. SPIE* 7866, 843607 (2011).
- [34] R. Hunt and M. R. Pointer, *Measuring Colour*, IVth edition (Wiley, 2011).
- [35] M. D. Fairchild, *Color Appearance Models*, IIIrd edition (Wiley, 2013).
- [36] D. M. Hoffman, N. N. Stepien, and W. Xiong, "The importance of native panel contrast and local dimming density on perceived image quality of high dynamic range displays," *J. Soc. Inf. Display* 24(4), 216-228 (2016).
- [37] F. Gou, H. Chen, M. C. Li, S. L. Lee, and S. T. Wu, "Submillisecond-response liquid crystal for high-resolution virtual reality displays," *Opt. Express* 25(7), 7984-7997 (2017).
- [38] J. H. Yoon, S. J. Lee, Y. J. Lim, E. J. Seo, H. S. Shin, J. M. Myoung and S. H. Lee, "Fast switching, high contrast and high resolution liquid crystal device for virtual reality display," *Opt. Express* 26(26), 34142-34149 (2018).

- [39] Y. H. Lee, T. Zhan, and S. T. Wu, "Prospects and challenges in augmented reality displays," *Virtual Reality & Intelligence Hardware* 1(1), 10-20 (2019).
- [40] M. H. Lu, M. S. Weaver, T. X. Zhou, M. Rothman, R. C. Kwong, M. Hack, and J. J. Brown, "High-efficiency top-emitting organic light-emitting devices," *Appl. Phys. Lett.* 81(21), 3921-3923 (2002).
- [41] L. H. Smith, J. A. E. Wasey, and W. L. Barnes, "The light out-coupling efficiency of top emitting organic light-emitting diodes," *Appl. Phys. Lett.* 84(16), 2986-2988 (2004).
- [42] E. Kim, J. Chung, J. Lee, H. Cho, N. S. Cho, and S. Yoo, "A systematic approach to reducing angular color shift in cavity-based organic light-emitting diodes," *Org. Electron.* 48, 348-356 (2017).
- [43] Q. Wang, Z. Deng, and D. Ma, "Realization of high efficiency microcavity top-emitting organic light-emitting diodes with highly saturated colors and negligible angular dependence," *Appl. Phys. Lett.* 94(23), 233306 (2009).
- [44] M.-K. Wei, J.-H. Lee, H.-Y. Lin, Y.-H. Ho, K.-Y. Chen, C.-C. Lin, C.-F. Wu, H.-Y. Lin, J.-H. Tsai, and T.-C. Wu, "Efficiency improvement and spectral shift of an organic light-emitting device by attaching a hexagon-based microlens array," *J. Opt. A: Pure Appl. Opt.* 10(5), 055302 (2008).
- [45] M. Thomschke, R. Nitsche, M. Furno, and K. Leo, "Optimized efficiency and angular emission characteristics of white top-emitting organic electroluminescent diodes," *Appl. Phys. Lett.* 94(8), 083303 (2009).
- [46] P. Yeh, *Optical Waves in Layered Media* (John Wiley & Sons, 1988).

- [47] K. A. Neyts, "Simulation of light emission from thin-film microcavities," *J. Opt. Soc. Am. A* 15(4), 962-971 (1998).
- [48] R. Zhu, Z. Luo, and S.-T. Wu, "Light extraction analysis and enhancement in a quantum dot light emitting diode," *Opt. Express* 22(S7 Suppl 7), A1783-A1798 (2014).
- [49] W. Brütting, J. Frischeisen, T. D. Schmidt, B. J. Scholz, and C. Mayr, "Device efficiency of organic light-emitting diodes: progress by improved light outcoupling," *Phys. Status Solidi* 210(1), 44-65 (2013).
- [50] S. Hofmann, M. Thomschke, B. Lüssem, and K. Leo, "Top-emitting organic light-emitting diodes," *Opt. Express* 19(106), A1250-A1264 (2011).
- [51] S. Kim, H.-J. Kwon, S. Lee, H. Shim, Y. Chun, W. Choi, J. Kwack, D. Han, M. Song, S. Kim, S. Mohammadi, I. Kee, and S. Y. Lee, "Low-power flexible organic light-emitting diode display device," *Adv. Mater.* 23(31), 3511-3516 (2011).
- [52] S.-F. Chen and C.-W. Wang, "Influence of the hole injection layer on the luminescent performance of organic light emitting diodes," *Appl. Phys. Lett.* 85(5), 765-767 (2004).
- [53] J.-B. Kim, J.-H. Lee, C. K. Moon, S.-Y. Kim, and J.-J. Kim, "Highly enhanced light extraction from surface plasmonic loss minimized organic light-emitting diodes," *Adv. Mater.* 25(26), 3571-3577 (2013).
- [54] D. Zhao, H. Liu, Y. Miao, H. Wang, B. Zhao, Y. Hao, F. Zhu, and B. Xu, "A red tandem organic light-emitting diode based on organic photovoltaic-type charge generation layer," *Org. Electron.* 32, 1-6 (2016).

- [55] Z. Gao, F. Wang, K. Guo, H. Wang, B. Wei, and B. Xu, "Carrier transfer and luminescence characteristics of concentration-dependent phosphorescent Ir (ppy) <sub>3</sub> doped CBP film," *Opt. Laser Technol.* 56, 20-24 (2014).
- [56] M. T. Lee, C. H. Liao, C. H. Tsai, and C. H. Chen, "Highly efficient, deep-blue doped organic light-emitting devices," *Adv. Mater.* 17(20), 2493-2497 (2005).
- [57] B. W. D'Andrade and J. J. Brown, "Organic light-emitting device luminaire for illumination applications," *Appl. Phys. Lett.* 88(19), 192908 (2006).
- [58] Y. Sakai, M. Shibata, and D. Yokoyama, "Simple model-free estimation of orientation order parameters of vacuum-deposited and spin-coated amorphous films used in organic light-emitting diodes," *Appl. Phys. Express* 8(9), 096601 (2015).
- [59] H. Riel, S. Karg, T. Beirlein, W. Rieß, and K. Neyts, "Tuning the emission characteristics of top-emitting organic light-emitting devices by means of a dielectric capping layer: An experimental and theoretical study," *J. Appl. Phys.* 94(8), 5290-5296 (2003).
- [60] L. S. Hung, C. W. Tang, M. G. Mason, P. Raychaudhuri, and J. Madathil, "Application of an ultrathin LiF/Al bilayer in organic surface-emitting diodes," *Appl. Phys. Lett.* 78(4), 544-546 (2001).
- [61] H. Riel, S. Karg, T. Beierlein, B. Ruhstaller, and W. Rieß, "Phosphorescent top-emitting organic light-emitting devices with improved light outcoupling," *Appl. Phys. Lett.* 82(3), 466-468 (2003).
- [62] A. B. Chwang, M. A. Rothman, S. Y. Mao, R. H. Hewitt, M. S. Weaver, J. A. Silvernail, K. Rajan, M. Hack, J. J. Brown, X. Chu, L. Moro, T. Krajewski, and N. Rutherford, "Thin

- film encapsulated flexible organic electroluminescent displays,” *Appl. Phys. Lett.* 83(3), 413-415 (2003).
- [63] A. P. Ghosh, L. J. Gerenser, C. M. Jarman, and J. E. Fornalik, “Thin-film encapsulation of organic light-emitting devices,” *Appl. Phys. Lett.* 86(22), 223503 (2005).
  - [64] J.-S. Park, H. Chae, H. K. Chung, and S. I. Lee, “Thin film encapsulation for flexible AM-OLED: a review,” *Semicond. Sci. Technol.* 26(3), 034001 (2011).
  - [65] H. Jung, H. Jeon, H. Choi, G. Ham, S. Shin, and H. Jeon, “Al<sub>2</sub>O<sub>3</sub> multi-density layer structure as a moisture permeation barrier deposited by radio frequency remote plasma atomic layer deposition,” *J. Appl. Phys.* 115(7), 073502 (2014).
  - [66] F. B. Sun, Y. Duan, Y. Q. Yang, P. Chen, Y. H. Duan, X. Wang, D. Yang, and K. W. Xue, “Fabrication of tunable [Al<sub>2</sub>O<sub>3</sub>: Alucone] thin-film encapsulations for top-emitting organic light-emitting diodes with high performance optical and barrier properties,” *Org. Electron.* 15(10), 2546-2552 (2014).
  - [67] C. H. Yang, P. Yin, J. H. Tao, J. C. Hsiao, M. T. Lee, H. H. Lu, and Y. H. Lin, “Novel thin film encapsulation structure for wearable plastic AMOLED display,” *SID Symp. Dig. Tech. Papers* 47, 841-843 (2016).
  - [68] C. A. C. Coello and G. B. Lamont, *Applications of Multi-Objective Evolutionary Algorithms* (World Scientific, 2004).
  - [69] C. S. McCamy, H. Marcus, and J. G. Davidson, “A color-rendition chart,” *J. Appl. Photogr. Eng.* 2(3), 95-99 (1976).

- [70] C. Vieri, G. Lee, N. Balram, S. H. Jung, J. Y. Yang, S. Y. Yoon, and I. B. Kang, "An 18 megapixel 4.3" 1443 ppi 120 Hz OLED display for wide field of view high acuity head mounted displays," *J. Soc. Inf. Display* 26(5), 314-324 (2018).
- [71] Y. Iwase, A. Tagawa, Y. Takeuchi, T. Watanabe, S. Horiuchi, Y. Asai, K. Yamamoto, T. Daitoh, and T. Matsuo, "A novel low-power gate driver architecture for large 8K 120 Hz liquid crystal display employing IGZO technology," *J. Soc. Inf. Display* 26(5), 304-313 (2018).
- [72] G. Kramida, "Resolving the vergence-accommodation conflict in head-mounted displays," *IEEE Trans. Vis. Comput. Graph.* 22(7), 1912-1931 (2016).
- [73] B. Bastani, E. Turner, C. Vieri, H. Jiang, B. Funt, and N. Balram, "Foveated pipeline for AR/VR head-mounted displays," *Inf. Disp.* 33(6), 14-19 (2017).
- [74] F. Heide, D. Lanman, D. Reddy, J. Kautz, K. Pulli, and D. Luebke, "Cascaded displays: spatiotemporal superresolution using offset pixel layers," *ACM Trans. Graph.* 33(4), 60 (2014).
- [75] Y. H. Lee, T. Zhan, and S. T. Wu, "Enhancing the resolution of a near-eye display with Pancharatnam-Berry phase deflector," *Opt. Lett.* 42(22), 4732-4735 (2017).
- [76] J. Y. Wu, P. Y. Chou, K. E. Peng, Y. P. Huang, H. H. Lo, C. C. Chang, and F. M. Chuang, "Resolution enhanced light field near eye display using e-shifting method with birefringent plate," *J. Soc. Inf. Display* 26(5), 269-279 (2018).
- [77] G. Osterberg, "Topography of the layer of rods and cones in the human retina," *Acta Ophthal. Suppl.* 6, 1-103 (1935).

- [78] H. Hua and S. Liu, "A dual-sensor foveated imaging system," *Appl. Opt.* 47(3) 317-327 (2008).
- [79] Y. Qin and H. Hua, "Continuously zoom imaging probe for the multi-resolution foveated laparoscope," *Biomed. Opt. Express* 7, 1175-1182 (2016).
- [80] J. P. Rolland, A. Yoshida, L. D. Davis, and J. H. Reif, "High-resolution inset head-mounted display," *Appl. Opt.* 37(19), 4183-4193 (1998).
- [81] M. Shenker, "Optical design criteria for binocular helmet-mounted displays," in *Display System Optics*, A. Cox, R. Hartmann, eds., *Proc. SPIE* 778, 70-78 (1987).
- [82] P. D. Burns, "Slanted-edge MTF for digital camera and scanner analysis," *Proc. IS&T 2000 PICS Conference*, 135-138 (2000).
- [83] S. Pancharatnam, "Generalized theory of interference and its applications," *Proc. Indian Acad. Sci. A* 44(5), 247-262 (1956).
- [84] M. V. Berry, "Quantal phase factors accompanying adiabatic changes," *Proc. R. Soc. London Ser. A* 392(1802), 45-57 (1984).
- [85] Y. H. Lee, G. Tan, T. Zhan, Y. Weng, G. Liu, F. Gou, F. Peng, N.V. Tabiryan, S. Gauza, and S. T. Wu, "Recent progress in Pancharatnam-Berry phase optical elements and the applications for virtual/augmented realities," *Opt. Data Process. Storage* 3(1), 79-88 (2017).
- [86] K. Gao, C. McGinty, H. Payson, S. Berry, J. Vornehm, V. Finnemeyer, B. Roberts, and P. Bos, "High-efficiency large-angle Pancharatnam phase deflector based on dual-twist design," *Opt. Express* 25(6), 6283-6293 (2017).

- [87] J. Kim, Y. Li, M. N. Miskiewicz, C. Oh, M. W. Kudenov, and M. J. Escuti, "Fabrication of ideal geometric-phase holograms with arbitrary wavefronts," *Optica* 2(11), 958-964 (2015).
- [88] M. Ono, J. Kobashi, H Yoshida, and M. Ozaki, "Doubling the geometric phase of reflective Pancharatnam–Berry diffractive waveplates." *J. Opt. Soc. America B* 36(5), D20-D27 (2019).
- [89] T. Zhan, Y. H. Lee, G. Tan, J. Xiong, K. Yin, F. Gou, J. Zou, N. Zhang, D. Zhao, J. Yang, S. Liu, and S. T. Wu, "Pancharatnam-Berry Optical Elements for Head-up and Near-eye Displays," *J. Opt. Soc. Am. B* 36(5), D52-D65 (2019).
- [90] O. Cakmakci and J. P. Rolland, "Head-worn displays: A review," *J. Display Technol.* 2, 199-216 (2006).
- [91] J. Geng, "Three-dimensional display technologies," *Adv. Opt. Photonics* 5(4), 456-535 (2013).
- [92] J. P. Rolland, M. W. Krueger, and A. Goon, "Multifocal planes head-mounted displays," *Appl. Opt.* 39(19), 3209-3215 (2000).
- [93] G. Wetzstein, D. Lanman, W. Heidrich, and R. Raskar, "Tensor displays: compressive light field synthesis using multilayer displays with directional backlighting," *ACM Trans. Graph.* 31(4), 1 (2012).
- [94] D. Cheng, Q. Wang, Y. Wang, and G. Jin, "Lightweight spatial-multiplexed dual focal-plane head-mounted display using two freeform prisms," *Chin. Opt. Lett.* 11(3), 31201 (2013).



- [95] S. Lee, C. Jang, S. Moon, J. Cho, and B. Lee, "Additive light field displays: realization of augmented reality with holographic optical elements," *ACM Trans. Graph.* 35(4), 60 (2016).
- [96] D. Lanman and D. Luebke, "Near-eye light field displays," *ACM Trans. Graph.* 32(6), 220 (2013).
- [97] H. Hua and B. Javidi, "A 3D integral imaging optical see-through head-mounted display," *Opt. Express* 22(11), 13484-13491 (2014).
- [98] B. T. Schowengerdt, R. S. Johnston, C. D. Melville, and E. J. Seibel, "3D displays using scanning laser projection," *SID Symp. Dig. Tech. Papers* 43(1), 640-643 (2012).
- [99] X. Hu and H. Hua, "High-resolution optical see-through multi-focal-plane head-mounted display using freeform optics," *Opt. Express* 22(11), 13896-13903 (2014).
- [100] S. Suyama, M. Date, and H. Takada, "Three-dimensional display system with dual-frequency liquid-crystal varifocal lens," *Jpn. J. Appl. Phys.* 39(2R), 480-484 (2000).
- [101] S. Liu and H. Hua, "Time-multiplexed dual-focal plane head-mounted display with a liquid lens," *Opt. Lett.* 34(11), 1642-1644 (2009).
- [102] G. D. Love, D. M. Hoffman, P. J. W. Hands, J. Gao, A. K. Kirby, and M. S. Banks, "High-speed switchable lens enables the development of a volumetric stereoscopic display," *Opt. Express* 17(18), 15716-15725 (2009).
- [103] T. Zhan, Y. H. Lee, and S. T. Wu, "High-resolution additive light field near-eye display by switchable Pancharatnam-Berry phase lenses," *Opt. Express* 26(4), 4863-4872 (2018).
- [104] X. Wang, Y. Qin, H. Hong, Y. H. Lee, and S. T. Wu, "Digitally switchable multi-focal lens using freeform optics," *Opt. Express* 26(8), 11007-11017 (2018).

- [105] S. Liu, Y. Li, P. Zhou, Q. Chen, and Y. Su, "Reverse-mode PSLC multi-plane optical see-through display for AR applications," *Opt. Express* 26(3), 3394-3403 (2018).
- [106] S. Yoon, H. Baek, S. W. Min, S.-G. Park, M. K. Park, S. H. Yoo, H. R. Kim, and B. Lee, "Implementation of active-type Lamina 3D display system," *Opt. Express* 23(12), 15848-15856 (2015).
- [107] F. Peng, H. Chen, F. Gou, Y. H. Lee, M. Wand, M. C. Li, S. L. Lee, and S. T. Wu, "Analytical equation for the motion picture response time of display devices," *J. Appl. Phys.* 121, 023108 (2017).
- [108] M. Schadt and W. Helfrich, "Voltage-dependent optical activity of a twisted nematic liquid crystal," *Appl. Phys. Lett.* 18, 127-128 (1971).
- [109] S. Lee, J. Cho, B. Lee, Y. Jo, C. Jang, D. Kim, and B. Lee, "Foveated retinal optimization for see-through near-eye multi-layer displays," *IEEE Access* 6(1), 2170-2180 (2018).
- [110] R. Narain, R. A. Albert, A. Bulbul, G. J. Ward, M. S. Banks, and J. F. O'Brien, "Optimal presentation of imagery with focus cues on multi-plane displays," *ACM Trans. Graph.* 34(4), 59 (2015).
- [111] S. Liu and H. Hua, "A systematic method for designing depth-fused multi-focal plane three-dimensional displays," *Opt. Express* 18(11), 11562-11573 (2010).
- [112] C. Oh and M. J. Escuti, "Achromatic polarization gratings as highly efficient thin-film polarizing beamsplitters for broadband light," *Proc. SPIE* 6682, 668211 (2007).
- [113] C. Oh and M. J. Escuti, "Achromatic diffraction from polarization gratings with high efficiency," *Opt. Lett.* 33(20), 2287-2289 (2008).

- [114] N. V. Tabiryan, S. V. Serak, S. R. Nersisyan, D. E. Roberts, B. Y. Zeldovich, D. M. Steeves and B. R. Kimball, “Broadband waveplate lenses,” *Opt. Express* 24(7), 7091-7102 (2016).
- [115] K.J. Hornburg, J. Kim and M. J. Escuti, “Experimental characterization of a F/1.5 geometric-phase lens with high achromatic efficiency and low aberration,” *Proc. SPIE* 10125 (2017).